Rectilinear Three-Body Problem using Symbolic Dynamics

Masaya Saito

Doctor of Science

ABSTRACT

We have studied the phase-space-structure via the structure that appears in the Poincaré section. In the rectilinear three-body problem, the motion of Newtonian three particles is studied, where the three particles are located on a line. The degree of freedom is two. In this study, we introduce a Poincaré section and study the structure of the Poincaré section made by the orbits starting from this surface. First, we study the change of the Poincaré section with varying mass ratio of the particles, and second, we study the relation between the structures of the periodic points and the surface of section.

The position on the Poincaré section used here is given by the scale of the system R, and the velocity ratio θ of both side particles relative to the central one. According to researches carried out by Mikkola & Hietarinta, the Poincaré section are divided into (i) the Schubart region – the collisions between the centre and both sides repeat alternately, (ii) the fast escaping region – the system is separated into binary and single particle after small number of collision, and (iii) the chaotic scattering region – the destiny of orbits is sensitive to their initial conditions. The Schubart region is the stable region around the periodic orbit called the Schubart orbit. Each subregion of the fast escaping region is arch-shaped, hence called scallops, and their bottom edges are segments on the θ-axis. The Schubart region is located on slightly above the centre of the Poincaré section. The chaotic scattering region fills intermediate region among them. If mass ratio is changed, the number of scallops change. Introducing the symbolic dynamics, Tanikawa & Mikkola(2000a,2000b) studied the equal mass case. Their result and results we obtained for other mass ratios using this method give us finer structure of the chaotic scattering region. A united region of (ii) the fast escaping region and (iii) the chaotic scattering region is divided into (v) sectors by curves running from the vertices of the Schubart region. Even thought the orbits whose initial points are on these curve have the same symbol sequence as that of the Schubart orbit, these orbits go away from the Schubart orbit at every intersection, and so the curves are distinguished from the Schubart region. A sector is composed of a scallop and block(s) of the triple collision curves: the block(s) contains only (vi) an arch-shaped one and may contain (vii) germ-shaped ones (hereafter germs). Whether a block contains germs or not depends on mass ratio. The border curve of sectors together with triple collision curves converge at the points on the θ-axis. We call the points footpoints.

Using McGehee's variable (1974), the equations of motion are extended to include the θ-axis as the initial conditions. The orbits from these extended initial points run on a two dimensional surface, i.e. the so-called triple collision manifold. These orbits are called fictitious. In particular, there are fictitious orbits that enter the fix point passing the foot points with winding around the triple collision manifold. Therefore, we can obtain the number of the footpoints, if we count the number of the winding. Recently, Sekiguchi et al.(2001,2003) in the symmetric collinear four-body problem and Sano (2003) in the collinear electron-ion-electron three body problem introduced McGehee's variables into

4

and showed the correspondence between the foot points and the fictitious orbits. In our problem, the winding number increases at mass ratios of the totally degenerate case as the central mass is decreased. Moreover, Simo(1989) obtained these mass ratios via numerical calculation. If we combine these results and the observation that the number of scallops increases as the central mass is decreased (HM1993), we expect that the number of sectors increases at the totally degenerate case. In order to confirm this, we attemp to follow the process that a new arch-shaped block appears. To visualise the structure of the Poincaré section, we divide it according to symbol sequences of the points on the section.

Near the mass ratio for totally degenerate case, triple collision curves are well stratified and each divided region is located according to a rule which will be explained in text. With decreasing the central mass until the next total degenerate case, we can see the following process: a germ bifurcates from the leftmost arch-shaped block. The germ grows to the roof and then extends to the lower right. This block finally reaches the θ-axis and becomes the lowest layer of the new arch-shaped block. Other germs bifurcate from all arch-shaped block. These blocks grow to recompose arch-shaped blocks. This recomposition changes the regime for locating the regions. If the mass ratio of the left and right particles becomes asymmetric, the above structure and process change a little bit. Among the divided regions, the regions, where the heavier particle is temporally ejected, shrinks or disappears depending on the mass ratio as asymmetry is increased. Moreover, different from the symmetric case, the formation process of the new sector is not clear-cut. The germ already exist at totally degenerate case.

The Schubart orbit appears as the fixed point on the Poincaré section. We consider a Poincaré map, which is a map from a point on the Poincaré section to another point. In the Schubart region, points move around the fixed point under the map. The behaviour of the rotation is described by the averaged number of rotation per iteration, namely the rotation number. Generally, when the rotation number at the fixed point is rational, periodic points bifurcate from the fixed point and go outward with the mass ratio being changed. We have detected such periodic points, and then studied their influence upon the structure of the Poincaré section. First we have found that the periodic points with the rotation number $(n-2)/n$, where n is the natural number grater than 2, dominate the structure. The periodic points with the rotation number $(n-2)/n$ are composed of n stable ones and n unstable ones. Second, after the periodic points leave the Schubart region, the unstable ones stay around the vertices of the Schubart region and their separatrices approximate the border of the Schubart region. On the other hand, the stable ones approach toward the θ-axis with collecting the germ-shaped blocks. These germs become the arch-shaped blocks.

Contents

Part I

The Change of the Poincaré Section for the Change of Mass Configuration

1 Introduction

The three-body problem is the discipline which asks how the motion of Newtoninan three particles is. This question has a great extent according to the purpose and interest of scientists. First, the three-body problem is utilised to study the motion of small bodies in the solar system, of stars in multiple stellar systems, and of spacecrafts. In this aspect, a highly accurate numerical integration of orbits is required, sometimes extending to a long future. We frequently have to deal with binary close approach appropriately for an accurate integration. The regularisation such as the Levi-Chivita transformation (Levi-Civita, 1904; Wintner, 1941) and the Kustaanheimo-Stiefel transformation (Kustaanheimo, 1964; Kustaanheimo and Stiefel, 1965; Stiefel and Scheifele, 1970) allows us to overcome this problem. These are basically a transformation from a Keplerian two-body system to a harmonic oscillator through the coordinate and time transformations.

The motion of a triple system in a binary close approach is considered to be a super-position of two binary motions: one is the inner binary making a close approach, and the other is the outer binary composed of the inner binary and the third body. The three body problem is called a *hierarchical three-body problem* in such cases. There are a number of researches on the structure which appears in the initial value space, when the points is associated with fate of orbits for the initial values.

Even if hierarchical three-body system appears in many astronomical scenes, it represents a special and stable case. The three-body system is generally more unstable and chaotic. The chaotic property is considerd to come from triple collision. Here, we use the term chaotic to be identical with the sensitivity on the initial conditions. Let us consider two orbits which start from initial points close to each other. These orbits may be similar until they experience triple approach. Generally, the phase space distance of two orbits is expected to become larger after triple approach. This chaotic structure in the phase space is studied for a general (not necessarily hierarchical) configuration. Indeed, researchers study the systems with special symmetry. h The isosceles three-body system and the rectilinear three-body system are examples of such systems. In the isosceles three-body system, one of the objects (we call m_1) runs on the z-axis, the others (also m_2 and m_3) run with keeping the relation $\overline{m_1 m_2} = \overline{m_1 m_3}$. In the rectilinear three-body system, which is studied in the present thesis, three objects run on a line. Due to the toy nature of these configurations, triple collision is almost automatically expected to take place, and hence the chaotic property of the three-body system can be studied.

The degree of freedom of the both systems is two. There is a powerful technique to explore the phase space in two degrees of freedom: the Poincaré section. A phase trajectory runs in the 3D energy hypersurface $H(q_1, q_2, p_1, p_2) = E$ inside the $4D$ phase space (q_1, q_2, p_1, p_2), where H is the Hamiltonian and E is the total energy. If an appropriate $2D$ surface is set up, the orbits for inital points on the surface cover the whole energy hypersurface. The successive intersections of orbits with the surface make pattern on it. We can acquire information about the phase space through this pattern. The pattern on

the surface is formed by successive images of the points under the *Poincaré map*. This surface is called the *Poincaré section* or the *Poincaré surface*. The quantitative structures of the Poincaré section are also studied with associating features such as the interplay time (a time until disintegration into a binary and a single objects) and the ejection length have been the target of researches (Mikkola and Hietarinta, 1989). In our research, we associate to each point of the surface the fate of orbits described by a *symbol sequence*. This approach seems to give us a new horizon.

We summarise to which extent the understanding of the structure of the Poincaré section in the rectilinear three-body system proceeds. The Poincaré section is divided into three basic regions, according to the distribution of the interplay time in the surface (Mikkola and Hietarinta, 1989, 1990, 1991; hereafter MH1989, MH1990, MH1991) and to the behaviour of points under Poincaré map (Hietarinta and Mikkola; hereafter HM1993). First, there exist the Schubart region, which is stable region of the periodic orbit, the so-called Schubart orbit (Schubart, 1956). Outside the region, there exists the chaotic scattering region, where the interplay time is so sensitive to the initial values that no discernible structure can be seen. Further outside, there exists the fast escaping region, where the system disintegrates into a binary and a single particle after several collisions. This region consists of scallop-like sub-regions, so they called them *scallops*. We adopt this terminology. The number of scallops increases with the decrease of the mass of central particle (HM1993). Tanikawa and Mikkola[10] studied the structure of the Poincaré section for the equal mass case using symbol sequences which record the collisional itineray of orbits. According their work, the chaotic scattering region is filled with triple collision initial points and these points form well stratified curves. The following structures will be important in the present research which can be understood from the result of TM2000a.

1. An arch-shaped stratum of triple collision curves make a *sector* together with the sub-region of the chaotic scattering region under the stratum.

2. There are four sectors and these surround the Schubart region.

3. The two (different) terminals of an arch are the points on the θ-axis ($R = 0$ line). The number of such points is also four, because an arch shares the terminals with the neighbouring arches.

We can expect that there are sectors at other mass ratios and their number increases with the central mass together with the number of scallops. The number of sectors, if they exist, can be also known from the number of the terminal points of arch-shaped strata. These points are limit initial points with zero initial distances for triple collision orbits, which can be dealt with McGehee's variables. In McGehee's coordinates, these orbits become spiral orbits on the *triple collision manifold*. McGehee's variables blow up the triple collision singularity into two dimensional surface with four holes (McGehee, 1974). McGehee(1974) proved the number of spirals increases with decreasing mass of the central object. We can

find that the number of terminals of arch-shaped strata also increases in proportion to the number of spirals through the examination of correspondence between the terminals and the spriral orbits. Indeed, such a correspondence is pointed out in similar dynamical systems to our system, i.e., the symmetric rectilinear four-body problem (Sekiguchi, 2001; Sekiguchi and Tanikawa, 2004) and the Coulomb rectilinear three-body problem (Sano, 2003).

The first purpose of the present study is to follow the structural change of the Poincaré section which results from mass variation. We have to confirm the conjecture that there are sectores and their number increases as decreasing the central mass. Even if it is true (actually true as is confirmed in the text), it is still unknown what process a new sector appears through. The second purpose is to understand the reason why the Poincaré section changes through the process. We will show that the certain periodic orbits which bifurcate from the Schubart orbit make this process, by actually detecting the periodic orbits via the numerical integration.

The followings are the contents of this paper. In section 2, the framework used in this paper is shown. The equations of motions, the Poincaré section and the symbol sequences are introduced in section 2.1 and the numerical setup is done in section 2.2. In section 3, the method to divide the Poincaré section according to the types of symbol sequences is introduced, and the result for a few mass cases is shown. We obtain the distribution of totally degenerate cases in the mass space in section 4. We show the partition of the Poincaré section for mass configurations selected according to the distribution of totally degenerate cases. In section 6, we interpret the structure observed in section 5. Finally, in section 7, we summarise the result of the present work.

2   The formulation, and method of Analysis

2.1   Equations of motion and the Poincaré section

In this section, we introduce equations of motion and the Poincaré section (Mikkola & Hietarinta, 1989, 1990, 1991, Hietarinta & Mikkola, 1993). We call the three particles on the line m_1, m_0 and m_2 from the left. Let the distance between m_1 and m_0 be q_1, and m_0 and m_2 be q_2. Then the Hamiltonian, H, of the system is

$$H = K - U \tag{1}$$

with

$$K = \frac{1}{2}\left(\frac{1}{m_1} + \frac{1}{m_0}\right)p_1^2 + \frac{1}{2}\left(\frac{1}{m_0} + \frac{1}{m_2}\right)p_2^2 - \frac{p_1 p_2}{m_0}$$

$$U = \frac{m_1 m_0}{q_1} + \frac{m_0 m_2}{q_2} + \frac{m_1 m_2}{q_1 + q_2},$$

where p_1 and p_2 are the canonical momenta conjugate to q_1 and q_2, K is the kinetic energy, and U is the force function. Hereafter, we restrict ourselves to the system of $H = E = -1$.

This Hamiltonian is singular at collisions. We remove the singularity at binary collision by the canonical transformation,

$$S = p_1 Q_1^2 + p_2 Q_2^2 \tag{2}$$

$$Q_i = \sqrt{q_i}, \ P_i = 2Q_i p_i, \tag{3}$$

and time transformation,

$$dt = q_1 q_2 dt', \tag{4}$$

where S is the generating function, and P_i and Q_i are new variables. After this transformation, equations of motion are reduced to the canonical equations whose independent variable is t'. The new Hamiltonian, Γ, and equations of motions are

$$
\begin{aligned}
\Gamma &= q_1 q_2 (H - E) \\
&= \frac{1}{8}\left[(\frac{1}{m_1} + \frac{1}{m_0}) P_1^2 Q_2^2 + (\frac{1}{m_0} + \frac{1}{m_2}) P_2^2 Q_1^2 - \frac{2}{m_0} P_1 P_2 Q_1 Q_2 \right] \\
&\quad - m_0 m_2 Q_1^2 - m_0 m_1 Q_2^2 - \frac{m_1 m_2 Q_1^2 Q_2^2}{Q_1^2 + Q_2^2} - Q_1^2 Q_2^2 E
\end{aligned}
\tag{5}
$$

$$\frac{dQ_i}{dt'} = \frac{\partial \Gamma}{\partial P_i}, \quad \frac{dP_i}{dt'} = -\frac{\partial \Gamma}{\partial Q_i}. \tag{6}$$

There exists a solution, which satisfies the relation,

$$q_1(t) = \Lambda q_2(t) \tag{7}$$

for all time, t. This solution is called the *homothetic solution* (Irigoyen and Nahon, 1972). Putting the condition (7) into equations of motion, the value of Λ is determined. Specially, if $m_1 = m_2$ (hereafter, we call this mass configuration simply *symmetric*), Λ is unity.

The points (q, p) that satisfy the energy integral, $H(q, p) = E$ and $q_1 = \Lambda q_2$, form the two-dimensional surface. We employ this surface for the Poincaré section, and introduce the coordinate (θ, R) on it. The variable, R, is defined by

$$R = 0.5(q_1 + q_2)|_{q_1 = \Lambda q_2}, \tag{8}$$

If R is given, U, and also K are determined. The variable, θ, is determined as follows. The kinetic energy K is written as the formula in $\dot{q}_1$ and $\dot{q}_2$:

$$K = A\dot{q_1}^2 + B\dot{q_2}^2 + Cq_1 q_2, \tag{9}$$

where

where $M = \sum_i m_i$, $A = \dfrac{m_1(m_0 + m_2)}{2M}$, $B = \dfrac{m_2(m_0 + m_1)}{2M}$, and $C = \dfrac{m_2 m_0}{2M}$.

This can be diagonalised by the linear transformation $(\dot{q}_1, \dot{q}_2) \rightarrow (\alpha, \beta)$,

$$r_1 = \frac{2\tau}{\tau + 1}, \quad r_2 = \frac{2}{\tau + 1} \tag{10}$$

$$\kappa = \frac{4AB - C^2}{4(Ar_1{}^2 + Br_2{}^2 + Cr_1r_2)} \tag{11}$$

$$\alpha = \sqrt{(A - \kappa r_2{}^2)}\dot{q}_1 - \sqrt{(B - \kappa r_1{}^2)}\dot{q}_2 \tag{12}$$

$$\beta = r_2\sqrt{\kappa}\dot{q}_1 - r_1\sqrt{\kappa}\dot{q}_2, \tag{13}$$

as

$$K = \alpha^2 + \beta^2. \tag{14}$$

The variable θ is introduced as the parameter that represents these new 'velocity' (α, β) :

$$\sin\theta = \beta/\sqrt{K}, \quad \cos\theta = \alpha/\sqrt{K}. \tag{15}$$

For a given value of K, θ divides the velocity among $\dot{q}_1$ and $\dot{q}_2$.

Let us consider ranges of (R, θ). Because $E < 0$ in our system, the upper limit $R_{\max}$ of R, is determined by $K = U - E \geqq 0$. Putting the relation (7) into it, $R_{\max}$ is

$$R_{\max} = \frac{|E|}{2}\left[\frac{\Lambda + 1}{\Lambda}m_0m_1 + (\Lambda + 1)m_0m_2 + m_1m_2\right]. \tag{16}$$

The range of θ is $0° \leq \theta \leq 360°$. However, if we have orbits starting from $\{(\theta, R)|0° \leq \theta \leq 180°\}$ to the past and the future, we can obtain orbits for $\{(\theta, R)|180° \leq \theta \leq 360°\}$ by exchanging the past and the future. Suppose that the value of θ changes from θ to θ' as $\dot{q}_i$ is changed, and we obtain the relation between θ and θ' in order to confirm this property. The formulae (12) and (13) with (15) being substituted become

$$\sqrt{K}\cos\theta' = -\sqrt{A - \kappa r_2^2}\dot{q}_1 - \sqrt{B - \kappa r_1^2}\dot{q}_2 = -\sqrt{K}\cos\theta = \sqrt{K}\cos(\theta + 180°) \tag{17}$$

$$\sqrt{K}\sin\theta' = -r2\sqrt{\kappa}\dot{q}_1 - r_1\sqrt{\kappa}\dot{q}_2 = -\sqrt{K}\sin\theta = \sqrt{K}\sin(\theta + 180°). \tag{18}$$

Therefore, it is found that $\theta' = \theta + 180°$.

The variable θ represents the direction of the velocity vector $(\dot{q}_2, \dot{q}_1)$ as shown in Fig.1. The line $q_1 = \Lambda q_2$ on the (q_2, q_1)-plane corresponds to the Poincaré section on the (q_2, q_1)-plane, that is, the orbit intersects the surface of section when the trajectory in the (q_2, q_1)-plane crosses this line. The homothetic orbit corresponds to the trajectory on the line. Its velocity vector with $\theta = 0°$ or $180°$, is parallel to the line. Velocity vectors of other orbits are like a dashed arrow. $\dot{q}_1 \geqq \Lambda\dot{q}_2$ corresponds to $0° \leq \theta \leq 180°$(above the line), and $\dot{q}_1 \leqq \Lambda\dot{q}_2$ corresponds to $180° \leqq \theta \leqq 360°$.

14

Since our system is scale invariant, we normalise masses of the system to make the total mass be 3, and introduce parameters a and b to represent the masses:

$$m_1 = 1 - a - b, \ m_0 = 1 + 2a, \ m_2 = 1 - a + b, \tag{19}$$

where

$$-0.5 \leqq a \leqq 1.5, \ \text{and} \ b \geqq 0.$$

This range of (a, b) becomes a triangle in (b, a)-plane, and we call it the '*mass-triangle*'. For simplicity, we call the mass parameters (a, b) the mass of the system.
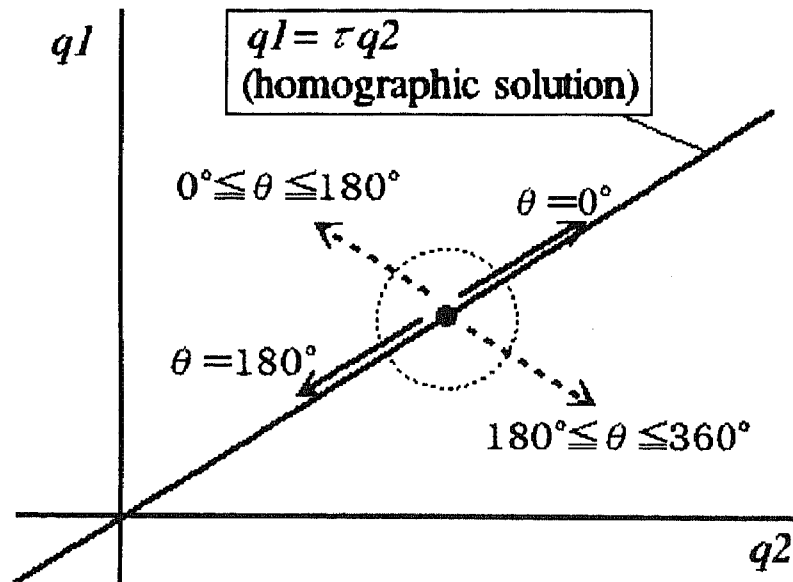

Figure 1: The relation between θ and the velocities

2.2 Numerical Procedure

TM2000a encoded the collisional history of orbits as sequences of symbols. The symbol '1' represents the collision between m_1 and m_0, the symbol '2' between m_0 and m_2, and the symbol '0' among all particles. Symbols are arranged from the left according to the time of collision. If it is necessary to distinguish the past sequence and the future sequence, the decimal point '.' are inserted. For instance, the trajectories drawn in Fig.2 correspond to the symbol sequence, '$\cdots .2(1)^3 21(2)^4 121 \cdots$'.

The initial points of triple collision orbits can be obtained from symbol sequences with some precision. Suppose that two orbits that start from close initial points, $z = (\theta, R)$ and $z + dz = (\theta + d\theta, R + dR)$, have symbol sequences whose first n-digits are common and symbols of the $(n + 1)$-th digit are different. After common n collisions, the left and
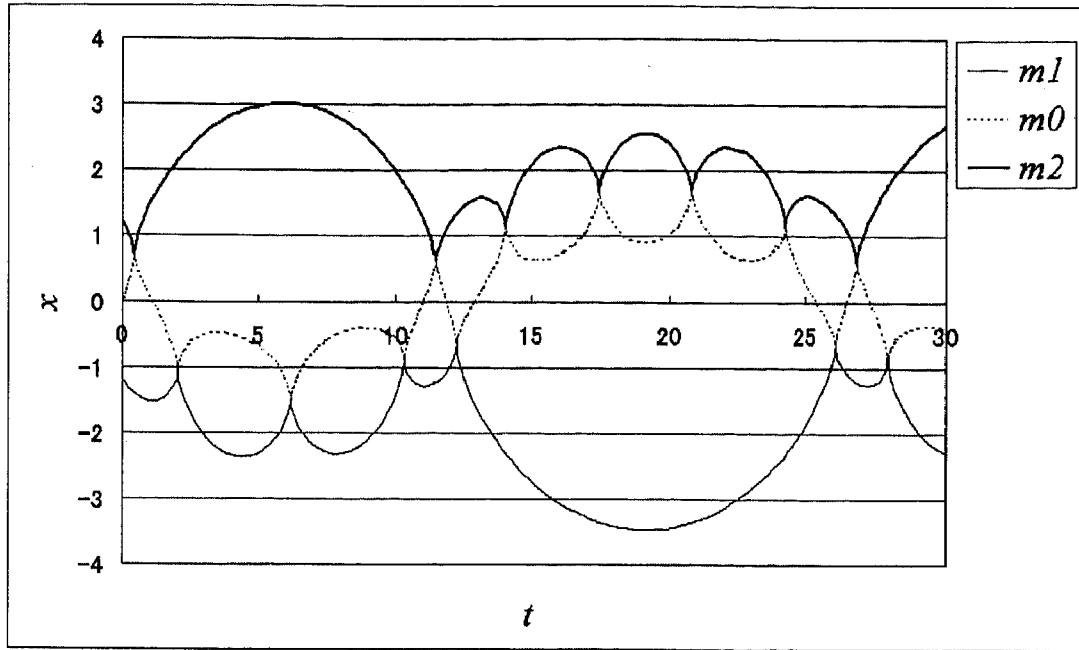
Figure 2: Correspondence of orbit and symbol sequence($\theta = 90°$, $R = 1.2$, for equal masses)

Grid of Poincaré section	$\theta = 180i/N_\theta (i = 0, \cdots, N_\theta - 1)$, $R = jR_{\max}/N_R$, $(j = 1, \cdots, N_R)$
	$N_\theta \times N_R = 540 \times 300$
End of integration	Until 64-th collision

Table 1: The setting of the integration

center particle collide in one orbit, whereas the right and center particles collide in the other orbit. Then, there should exist a triple collision orbit which starts from between z and $z + dz$, for both orbits have to change smoothly when the starting point is changed from z to $z + dz$ continuously.

We introduce grid into the Poincaré section and integrate the orbit from grid points to the future. These orbits are recorded as symbol sequences. Hence, the grid points on the Poincaré section can be associated with symbol sequences. The size of grids and condition for terminating the integration are shown in Table 1.

In Fig.1, the grid points are taken from $\{(R, \theta) | 0° \leqq \theta \leqq 180°\}$ (hereafter, *front side* of the Poincaré section) and not taken from $\{(R, \theta) | 180° \leqq \theta \leqq 360°\}$ (hereafter, *rear side* of the Poincaré section). Even if an orbit starts from the rear side, this orbit shall go back to the front side except the immediate escaping orbit. Therefore, we consider that the structure of the rear side of the Poincaré section is reflected into the structure of the front side, and we omit orbits starting from the rear side.

3 Partition of the Poincaré section

3.1 Structures of the Poincaré section and terminologies

TM2000a succeeded in obtaining the fine structure of the Poincaré section for equal mass case by obtaining the triple collision curves using symbol sequences. We have obtained the fine structure for other mass cases. In this section, we show the structure for three mass cases and introduce names for components of the structure. The initial points of orbits ending in triple collision form curves called triple collision curves on the Poincaré section. In this subsection, we look at the distribution of these curves, and give names to the structures of the Poincaré section. We show the Poincaré section for three mass configurations. Here and below we take, for the axes of the Poincaré section, $0 \leqq \theta \leqq 180°$ and

Figure 3 is the distribution of the triple collision curve on the Poincaré section. The range of axes is $0 \leqq \theta \leqq 180°$ (for horizontal) and $0 < R < R_{\mathrm{max}}$ (for vertical). This range is taken in the following figures of the Poincaré section. Figure 3(a) is of equal mass case (TM2000a). The Poincaré section is filled with triple collision curves except for the regions marked with (i),(ii),(iii), (iv), and (v). As for an orbit starting from the regions marked with (i)$\cdots$(iv), m_1 or m_2 run away to infinity. We call this particle an *escaping* particle and call the orbit an escape orbit. Mikkola and Hietarinta(1989) called these regions *fast escaping regions* or *scallops* from the shape. Now, if the particle running away shall go back to the binary, we call this particle an *ejected* particle, distinguishing it from escaping particle. Starting from (v), an orbit is stable with symbol sequences $(21)^{\infty}$. There is an initial point of a periodic orbit called the Schubart orbit in this region (Schubart, 1956). Therefore, Mikkola and Hietarinta call the region the *Schubart region*. When Hietarinta & Mikkola(1989) found the extent of the escaping and Schubart regions on the (θ, R)-plane, they used the distribution of the time until the system breaks into a binary and a single (dwell time). The dwell time is very short for the fast escaping region, while infinite for the Schubart region. In the remaining region, filled with triple collision curves in our scheme, they found that the dwell time was sensitive to the initial points and any structure seemed not to exist. Therefore, they called the region the *chaotic scattering region*.

The Poincaré section from which the Schubart region is removed is separated into *sector* by 'arms' running from the vertices of the Schubart region. There are four in (a), six in (b), and three in (c) sectors. A sector contains a scallop and a block/blocks of strata of triple collision curves. We call this block the *chaotic scattering block* (CSB). There is one *arch-shaped* CSB in all cases, and in (c), there are also *germ-shaped* CSB. A triple collision curve has terminal points on the θ-axis. We call them *foot points* (FOPs). The numbers of FOPs and arch-shaped CSB (hereafter, n_{FOP} and n_{ACS}) are the same. The triple collision curves in a CSB convergent into the same FOPs, so CSBs become thin where R is small. We call the thiner part a *leg*.

When mass parameters (a, b) are changed, the structure of the Poincaré Section changes complicatedly. However, the change of $n_{ACS}(= n_{FOP})$ is the most remarkable. The FOPs is the initial points $\lim_{R \to 0}(R, \theta)$ for triple collision. In Sect.4, we calculate the number of the FOPs using McGehee's variables, which enable us to integrate the orbits starting from $\lim_{R \to 0}(R, \theta)$.

3.2 Cylinder of symbol sequences

Although the change of the Poincaré section caused by the change of mass of the system appears on the strata of triple collision, this structure is too fine-grained to understand this change macroscopically. TM2000b found that the Poincaré section is divided into 13 regions, $I_1, \cdots, I_{12}$ and S, which are defined by sets of symbol sequences: $\{1.(21)^{2k}22 \cdots | k > 0\}$ for I_1, $\{1.(21)^{2k+1}2 \cdots | k > 0\}$ for I_2, etc.(see Fig.3 and Table 5 in TM2000b). In dynamics terminology, a set of symbol sequences that satisfy the requirements for symbols is called a *cylinder*. The structure obtained from the partition has suitable grain to study the dependency on mass. However, since these cylinders are adapted to equal mass case, we have to generalize them for general mass of the system. The definition of the generalised cylinders, $S_{c,j}(c, j \in \mathbf{N})$, is

$$S_{c,j} \equiv \begin{cases} \{(21)^i(2)^j \cdots | i \geqq 0, j \geqq 1\} & \text{for } c = 2i + 1 \\ \{(21)^i(1)^j \cdots | i \geqq 1, j \geqq 1\} & \text{for } c = 2i \end{cases} \tag{20}$$

$$S_c \equiv \cup_{j < \infty} S_{c,j}. \tag{21}$$

Since we consider only the front side of the Poincaré section, all symbol sequences have the form '$.2 \cdots$'. The suffix c has information about the number of alternate collisions and ejected particle[1], which is m_1 for odd c, and m_2 for even c. A cylinder $S_{\infty,j}$ $(S_{c,j}|_{c=\infty})$ correspond to the Schubart region and $S_{c,\infty}$ $(S_{c,j}|_{j=\infty})$ to escaping orbits. The structure obtained from $S_{c,j}$ is still finer than that of TM2000b. We then only distinguish $S_{c,j}$ with $j < \infty$ from $S_{c,\infty}$. In order to do so, we sum $S_{c,j}$ for $j < \infty$ and create cylinders S_c.

In order to divide the Poincaré section, we associate S_c and $S_{c,\infty}$ with regions $\mathrm{reg}(c)$ and $\mathrm{reg}((c, \infty))$. In addition, we abbreviate multiple regions $\mathrm{reg}(c_1), \mathrm{reg}(c_2), \cdots$ as $\mathrm{reg}(c_1, c_2, \cdots)$. We show $\mathrm{reg}(c)$ and $\mathrm{reg}((c, \infty))$ concretely. First, the correspondence between these regions and three regions in HM1993 is

| Fast escaping regions	$\mathrm{reg}((c, \infty))$	$1 \leqq c \leqq n_{FOP}$
Chaotic scattering region	$\mathrm{reg}(c) \cup \mathrm{reg}((c, \infty))$	$1 \leqq c \leqq \infty$
Schubart region	$\mathrm{reg}(c)$	$c = \infty$

Second, we reproduce the partition into 13 regions for equal mass case in Fig 4. A rule for the region number c of regions contained in a arch-shaped CSB is found from the reproduction. From the left, each CSB contains $\mathrm{reg}(1, 5, 9, \cdots)$, $\mathrm{reg}(2, 6, 10, \cdots)$, $\mathrm{reg}(3, 7, 11, \cdots)$,

---

[1]Note that a repeating symbol is opposite to the ejected particle: for example, the ejected particle corresponding to $(\underline{2})^j$ is $m_{\underline{1}}$.

18

(a) $a = 0, b = 0$
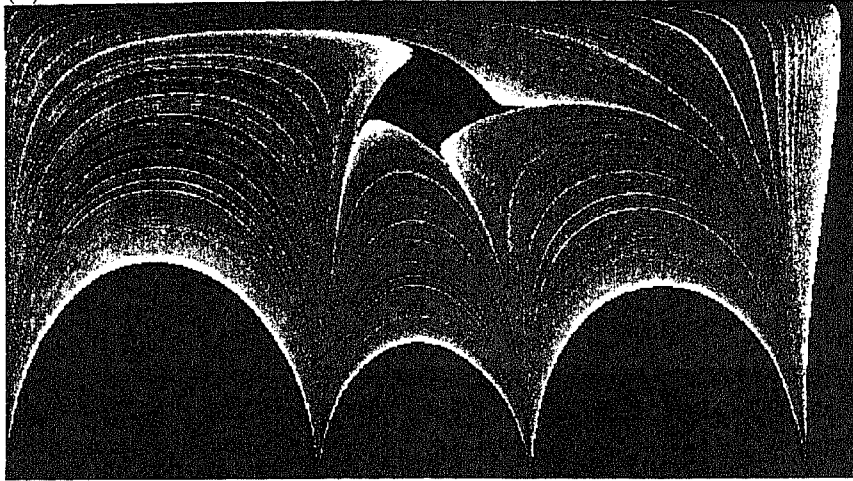
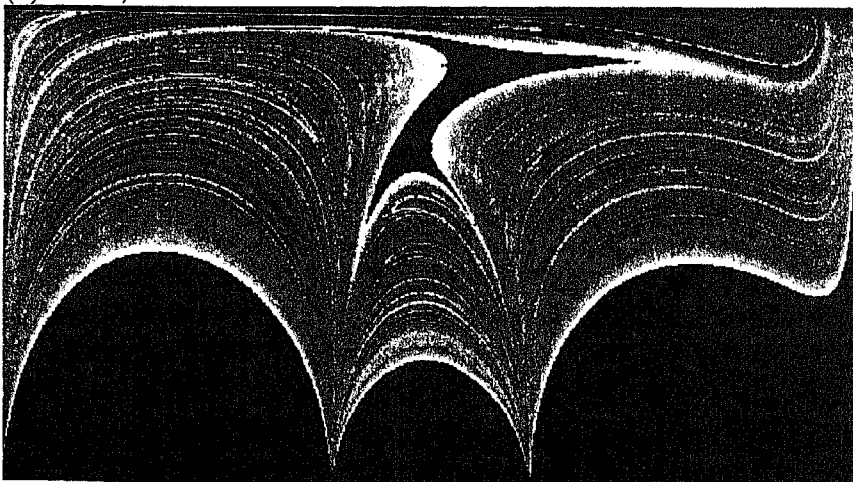(b) $a = -0.31, b = 0$
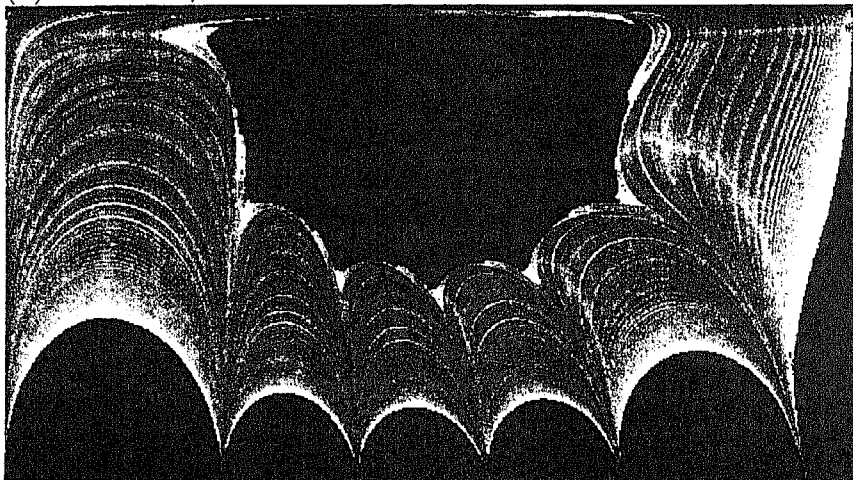
(c) $a = 0, b = 0.1$

Figure 3: Triple collision curve on the Poincaré section

and $\mathrm{reg}(4, 6, 12, \cdots)$, respectively. It is summarised as the rule that each CSB contains $\mathrm{reg}(c)$ whose c are congruent (modulo 4). The modulus, here being 4, depends on masses and is considered to be a number that represents the basic structure of the Poincaré section. We then give it n_{mod}.
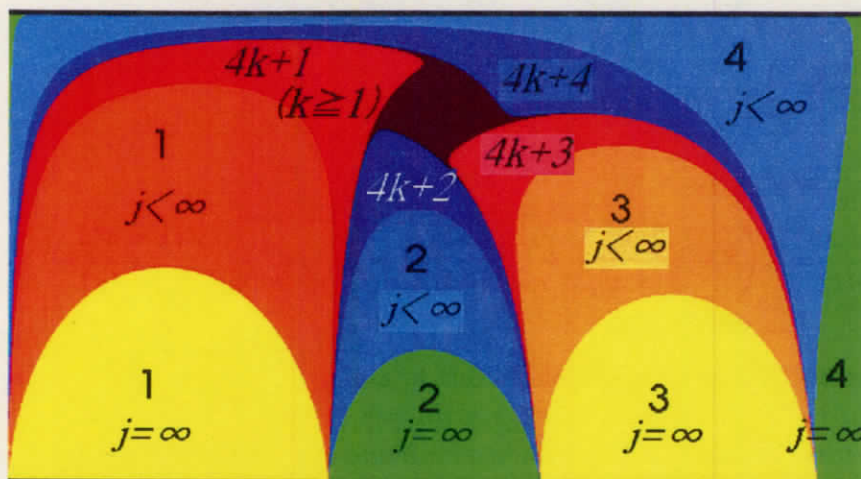

Figure 4: The division by cylinder in equal mass case. The number on the region is the value of c. If necessary, the value of j is shown.

4 The distribution of the number of root on mass-triangle

The purpose of this section is to obtain the distribution of numbers of roots on the mass-triangle. (The reason of not 'number' but 'numbers' shall be mentioned in the section.) This is the preparation for the study of the structural variation of Poincaré section depending on mass of the system, demonstrated in the next section.

Recall that roots are convergent point on the θ of triple collision curves, namely are initial points of orbits ending in triple collision as $R \to 0$. If McGehee's variables are introduced, equations of the motion are extended and include such orbits, called *fictitious orbits*, as ordinary solutions (McGehee, 1974).

4.1 McGehee's variables and triple collision manifold

We explain the meaning of McGehee's variables in the following. McGehee's variables consist of (r, w, s, v). The variable r is the square root of the inertial moment($r = \sum m_i x_i^2$), which represents the size of the system. The variable $s \in [-1, 1]$ indicates the configuration of the system, and $s = -1$ and $s = 1$ correspond to the left collision (symbol '1') and

the right collision (symbol '2'), respectively. The velocity of particles is related to w and v. The equations of motion described by McGehee's variables are

$$\frac{dr}{d\tau} = \frac{\lambda(1-s^2)}{\sqrt{W(s)}}rv \equiv f_r \tag{22}$$

$$\frac{dv}{d\tau} = \frac{\lambda}{2}\left[\frac{1-s^2}{\sqrt{W(s)}}v^2 - \sqrt{W(s)}\left(1 - \frac{2w^2}{1-s^2}\right)\right] \equiv f_v \tag{23}$$

$$\frac{ds}{d\tau} = w \equiv f_s \tag{24}$$

$$\frac{dw}{d\tau} = s\left(1 - \frac{2w^2}{1-s^2}\right) + \frac{1}{2}\frac{W'(s)}{W(s)}(1-s^2-w^2) - \frac{\lambda(1-s^2)}{2\sqrt{W(s)}}vw \equiv f_w, \tag{25}$$

where

$$W(s) = \frac{\sin 2\lambda}{2\lambda}[W_1(s) + W_2(s) + W_3(s)] \tag{26}$$

$$W_1(s) = \frac{m_1 m_0(1-s)}{(b_0 - b_1)\mathrm{sinc}(\lambda(1+s))}, \quad \mathrm{sinc}x = \frac{\sin x}{x}$$

$$W_2(s) = \frac{m_0 m_2(1+s)}{(a_2 - a_0)\mathrm{sinc}(\lambda(1-s))}$$

$$W_3(s) = \frac{\lambda m_1 m_2(1-s^2)}{(b_0 - b_1)\sin(\lambda(1+s)) + (a_2 - a_0)\sin(\lambda(1-s))}$$

$$\lambda = \arccos(a_1 m_1 b_1 + a_0 m_0 b_0 + a_2 m_2 b_2) \tag{27}$$

$$a_1 = a_0 = -\sqrt{\frac{m_2}{(m_1 + m_0)(m_1 + m_0 + m_2)}}, \quad a_2 = \sqrt{\frac{m_1 + m_0}{m_2(m_1 + m_0 + m_2)}} \tag{28}$$

$$b_1 = -\sqrt{\frac{m_0 + m_2}{m_1(m_1 + m_0 + m_2)}}, \quad b_0 = b_2 = \sqrt{\frac{m_1}{(m_0 + m_2)(m_1 + m_0 + m_2)}}. \tag{29}$$

Since the substitution $r = 0$ into (22) gives $dr/d\tau = 0$, equations (22)-(25) have solutions $(r(\tau) = 0, w(\tau), s(\tau), s(\tau))$. These are just solutions starting from θ-axis including roots. When $r(\tau) = 0$, orbits of (w, s, v) run on the two-dimensional surface, which is called the *triple collision manifold* (TCM). In Fig.5, the schematic diagram of TCM is shown in blue. The Poincaré section is embedded as the plane $s = 0$ in the (w, s, v)-space, which is also shown in the figure. If total energy $E < 0$, (real) orbits run inside the TCM, and if $E > 0$, outside the TCM. Since we consider $E < 0$, the Poincaré section is inside the TCM, in Fig.5. The θ-axis is the intersection of $s = 0$ and the TCM. To show the correspondence, the value of θ, $0°$, $90°$, $180°$, and $270°$ are written in Fig.5. Equation (22)-(25) have two equilibrium points c and d,

$$(r, w, s, v) = c : (0, 0, s_c, +v_c), \quad d : (0, 0, s_c, -v_c), \quad \text{where } V'(s_c) = 0, \quad v_c = \sqrt{2V(s_c)}. \tag{30}$$
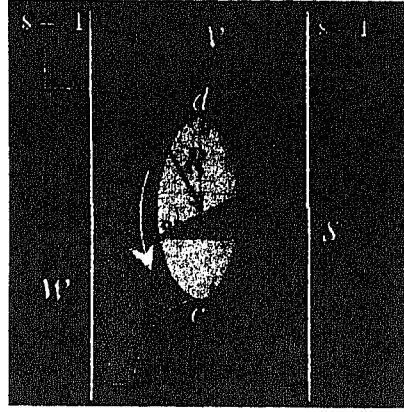
Figure 5: Triple Collision Manifold

The equilibrium points are initial points of the triple collision to the future for c and to the past for d. Moreover, at d and c, $\theta = 0°$ and 180, respectively. On the TCM, stable and unstable manifold of d and c are one-dimensional, and we denote them W_c^s, W_c^u, W_d^s, and W_d^u. On the whole (r, w, s, v)-space, the stable and unstable manifold of d are one- and two-dimensional, and, of c, vice versa. Figure 6(a) shows the relation between these manifolds and their relation to triple collision orbits. The stable manifold of c is a surface shown with shade. The straight path from d to c is the homothetic orbit. This path W_d^s and W_c^s are edges of the stable manifold. A triple collision orbit runs along with W_d^s and passes near d then runs along with the homothetic orbit. As $R \to 0$, (as starting point is close to the TCM), the triple collision orbit approaches W_d^s and the homothetic orbit. Therefore, when $R = 0$, triple collision orbits are on W_d^s, and intersections of W_d^s and the Poincaré section are starting points of triple collision when $R = 0$ namely roots.

4.2 The relation between roots and the fictitious orbit

In this subsection, using the schematic diagram of the TCM, Fig.6(b) and (c), we explain how to find the root .The TCM is homeomorphic to a sphere with four holes. Figures 6(b) and (c) are the top view of the northern and southern hemispheres. In this sphere, arms and legs of the TCM are transformed to four holes, $L+$, $R+$, $L-$, and $R-$. The vertical line represents the θ-axis. The lines $s = -1$ and $s = +1$ are projected onto the horizontal lines which terminate at $L + (L-)$ and $R + (R-)$ on the both hemisphere. The v-axis is projected onto d and c. The stable manifold W_d^s has two branches which go opposite direction from d. We distinguish their direction by the sign of the w component, and write them W_d^{s+} and W_d^{s-}.

From d, we trace one of the branches backward to the direction of the arrow. In the case of the figure, both branches spiral 3/2-times around the v-axis. The number of the spiraling depends on mass of the system. Then the branch falls into L^- or R^-. Therefore,

the branch intersects once with the Poincaré section every one passage between $s = -1$ and $s = +1$. The intersections on the front side are labeled p_i and on the rear side p_i^*, where $1 \leq i \leq 3$ in the case of the figure. It is roots of the front and rear sides that are p_i, d and p_i^*, d. If intersections of W_d^{s+} or W_d^{s-} is counted from p_1^* or p_1, the roots on the front side are what W_d^{s+} intersects at even order and W_d^{s-} at odd order. For the rear side, the parity is reversed. With consideration of this relation, the distribution of the number of passage between $s = \pm 1$ on the mass-triangle, which is studied first by Simó (1980), can be translated into the distribution of the number of roots.

If the central particle is made light, the number of spirals around v-axis increases. After increase of $1/2$ spirals, the target of the fall changes from L^- to R^-, and vice versa. For the critical masses, the branch enters c instead of falling into L^- nor R^-. At this point, one of the branch of W_d^s coincides with one of the branches of W_c^u. The flow for this situation is called totally degenerate.

Even if one of W_d^{s+} and W_d^{s-} enters c, the other branch does not always enter c. Therefore, the number of roots is not always the same on the both sides of the Poincaré section. Hence, we redefine variables for the number of roots. We use n_{FOP} for the front side as before, and introduce n_{FOP}^* for the rear side. Since $s = -1$ and $s = +1$ correspond to symbols '1' and '2', both branches can be associated with symbol sequences. The symbol sequences of W_d^{s+} and W_d^{s-} are $(2)^\infty 1210$ and $(1)^\infty 2120$. For the orbits that do not pass roots, it is sufficient to consider orbits that pass the point p_x and p_y, which are points above and below p_1. The orbit passing p_x moves a path similar to W_d^{s-} before the passage of p_x. After the passage, the orbit passes near d, and falls into R^+. Conversely, the orbit that passes p_y falls into R^-. Therefore, the symbol sequence of orbits starting from the θ-axis is the following:

| Range	(d, p_1)	p_1	(p_1, p_2)	p_2	(p_2, p_3)	p_3	(p_3, c)
Symbol Sequence	$1.(2)^\infty$	1.20	$1.2(1)^\infty$	1.210	$1.21(2)^\infty$	1.2120	$1.212(1)^\infty$

4.3 The number distribution of roots

We have obtained the distribution of $(n_{\mathrm{FOP}}, n_{\mathrm{FOP}}^*)$, based it on the previous subsection. As for the detail of the calculation, we write in appendix A. The distribution is shown in Fig.7(a),(b), and (c). The figure shows (a) whole mass-triangle, (b) area around $(a = 0, b = 0)$ and (c) $(a = 0.41, b = 1.0)$. All borders has a label in the form, $(n) \rightarrow (n+1)\pm$, which shows that the number of the travels of $W_d^{s\pm}$ increases from n to $n+1$, if the border is crossed downwards.

For example, if we cross '$2 \rightarrow 3+$' downward, a new intersection of W_d^{s+} appears, and since its numeric order is 3 namely odd, n_{FOP}^* increases. A similar discussion for other borders and known $(n_{\mathrm{FOP}}, n_{\mathrm{FOP}})$ for one point on the mass-triangle gives concrete values of $(n_{\mathrm{FOP}}, n_{\mathrm{FOP}}^*)$ for whole mass-triangle. The relation that three particle are marshaled in the order of their masses $(m_1 < m_0 < m_2)$ is written as $-b/3 < a < +b/3$.

(a) Flow inside the TCM
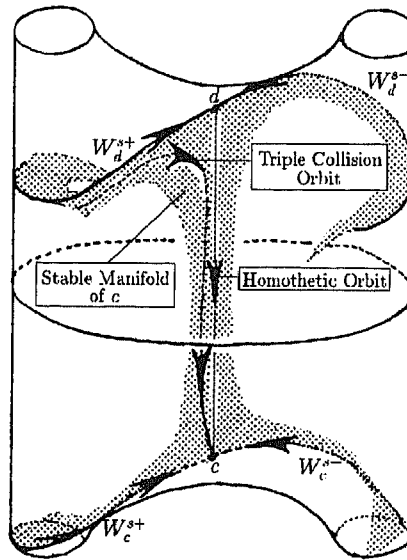
(b) Flow on the TCM
(the Northern Hemisphere)
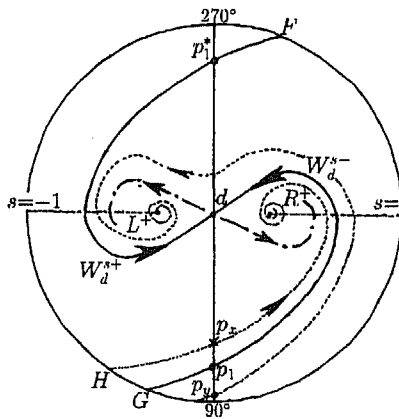
(c) Flow on the TCM
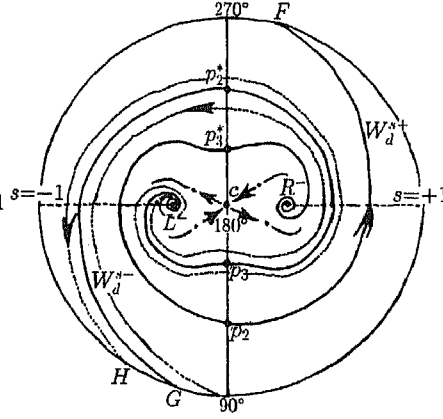(the Southern Hemisphere)

Figure 6: Stable and unstable manifold of equilibrium points
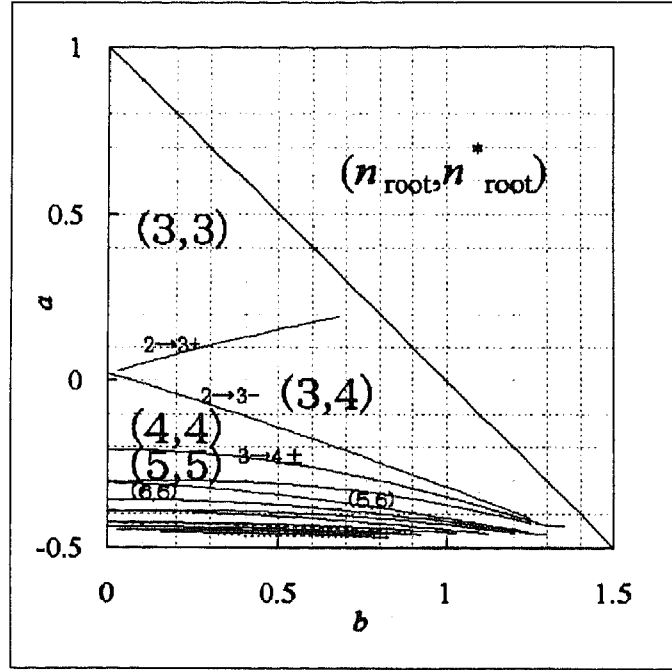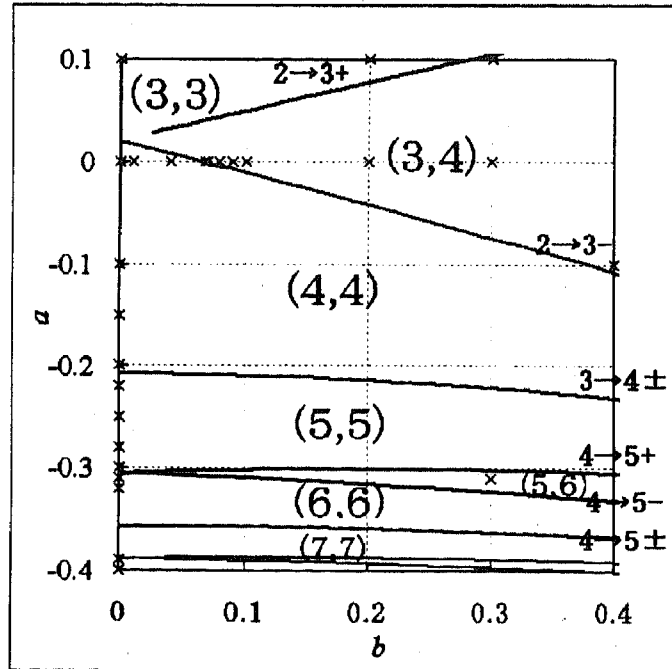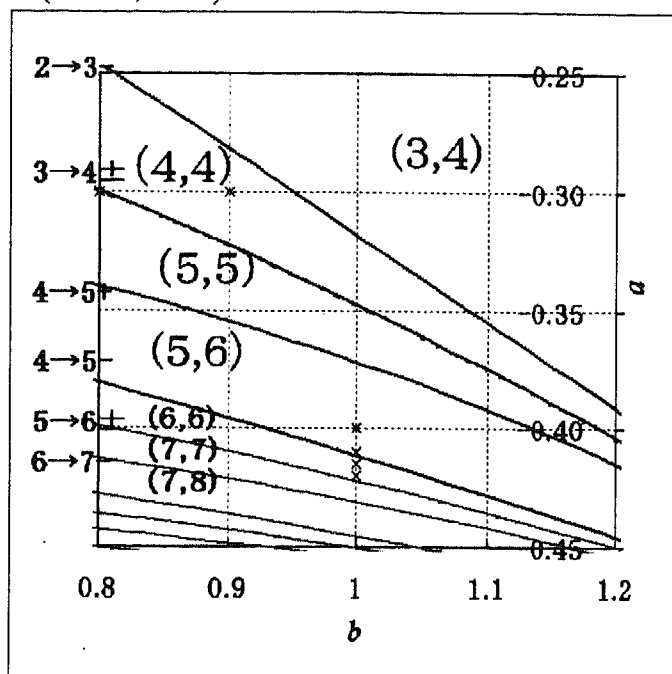
(a) global mass triangle

(b) neighbourhood of $(a, b) = (0, 0)$

Figure 7: The distribution of the number of passage between $s = -1$ and $s = 1$ and the distribution of (n_{FOP}, n^*_{FOP}). The winding number and the number of roots in both side

(c) neighbourhood of $(-0.41, -1.0)$
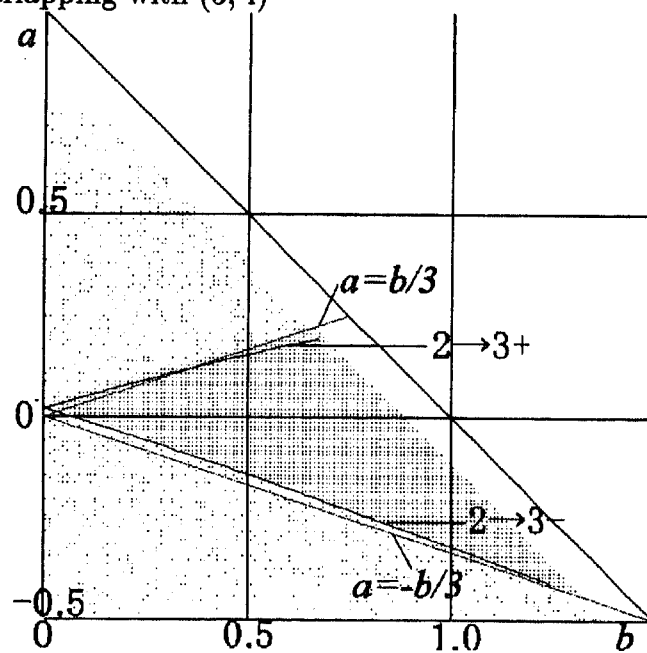

(d) regions near overlapping with $(3, 4)$

Figure 7: continue

The corresponding area on a mass-triangle nearly coincide with the area being $(3, 4)$. The correspondence is shown in 7(d). The Schubart orbit being the fixed point of the Poincaré map on (θ, R)-plane, MH1991 and HM1993 studied the distribution of the linear stability of the fixed point on the mass-triangle. Plotting the distribution on 7(d), we find that area $(3, 4)$ nearly coincides with also unstable area. In this plot, we regard the fixed point as unstable, when the eigenvalue of the matrix representing the linearisation is grater than 1.0005.

5   How the Poincaré section changes as (a, b) are changed

In this section, we describe the structure change of the Poincaré section as the mass configuration is changed. As we already pointed out in the Introduction, the structure change of the Poincaré section has been described in HM1993. They concentrated their attention to the change, with mass configuration, of the stability of the Schubart region and the related stability of the chaotic scattering regions, the latter stability being measured by the time until escape. Their result also shows that the number of n_{ACS} increases when a is decreased. Our analysis in the preceding section has explained this increase by way of the increase of the winding number of $W_d^{s\pm}$ for the (a, b) which is studied by Simo(1980). Therefore, the remaining major problem is how new arch-shaped CSBs appears when mass parameters are changed continuously. We show a scenario for the problem before show the details of results.

The triple collision curves for mass parameters near total degenerate case form well stratified strata. There is rule for the region number of the regions that compose a arch-shaped CSB: the lowest strata of arch-shaped CSB are $\operatorname{reg}(1)$, $\operatorname{reg}(2)$, $\cdots$, $\operatorname{reg}(n_{FOP})$ from the left, and a block are composed by $\operatorname{reg}(\ell, \ell + n_{FOP}, \ell + 2n_{FOP}, \cdots)$. Let us be decreasing the mass parameter a until the next total degenerate case. The $\operatorname{reg}(n_{FOP} + 1)$, which will be the lowest strata of the new arch-shaped CSB, are the second strata of the leftmost arch-shpaed CSB. Second and upper strata $(\operatorname{reg}(n_{FOP} + 1, 2n_{FOP} + 1, \cdots))$ of this block bifurcate and compose a germ-shaped CSB between the leftmost and the rightmost CSB. This germ-shaped CSB push up the rightmost CSB, then push down toward the θ-axis and touch at total degenerate case. At the moment of the touch, the rightmost CSB become the second rightmost one and the germ CSB the rightmost one. The above scenario explain the process that the new CSB appears for symmetric and $n_{FOP} \geq 4$ (equivalent to $a \leq 0$). But for $n_{FOP} \geq 4$ the scenario does not explain the process, which is too complex to summarise here. The scenario explains also asymmetric case, and however the additional features appear. The regions with even numbers shrink as the asymmetry parameter b being increased. Particularly, when $n_{FOP} \neq n_{FOP}^*$, these regions disappear at high b. We will explain about the disappearance associating with the flow on the TCM in Sect.6. Moreover, for large n_{FOP} and high b, bifurcations for another new CSB, before the composition of the new CSB is completed.

5.1   Symmetric case 1: $n_{\mathrm{root}} \geq 4$

We divide the symmetric case into two sub-cases where $n_{\mathrm{FOP}} = 3$ and $n_{\mathrm{FOP}} \geq 4$ according to the difference of the process for the appearance of the new CSB. We here describe the latter case. In the symmetric case ($b = 0$), $n_{\mathrm{FOP}} \geq 4$ corresponds to $a \lesssim 0$ (more accurately, $a \leq a_{3,4} = 0.019823$). Figure 8 shows several Poincaré sections for the parameter values ranging from $a = -0.15$ to $a = -0.31$. In this mass range, the 5th and 6th arch-shaped CSBs appear. Each colour corresponds to each reg(c) for $c = 1, \cdots, 14$. For $c = 15, \cdots, 31$, the regions are painted in gray. If $c \geq 32$, regions are regarded as the part of the Schubart region and painted in light-green, so that the Schubart region looks larger. The regions in balck represent the sub-regions, $\mathrm{reg}((1,\infty)), \mathrm{reg}((2,\infty)), \cdots$, and $\mathrm{reg}(n_{\mathrm{FOP}}, \infty)$, of the fast escape region disposed from the left in the ascending order. The correspondence between colours and regions will be the same in the figures in Section 5.

As we have shown in the opening of section 5, near the total degenerate case, the ℓ-th arch-shaped CSB from the left is composed by $\mathrm{reg}(\ell, \ell + n_{\mathrm{FOP}}, \ell + 2n_{\mathrm{FOP}}, \cdots)$ from the bottom or formally by the regions

$$\bigcup_{c} \mathrm{reg}(c \equiv \ell (\mathrm{mod}\ n_{\mathrm{mod}})), \tag{31}$$

$$\text{where } n_{\mathrm{mod}} = n_{\mathrm{FOP}} \text{ and } 1 \leq \ell \leq n_{\mathrm{FOP}}.$$

This simple '$n_{\mathrm{mod}} = n_{\mathrm{FOP}}$ organisation' is seen in the cases $a = -0.22$ and -0.31.

The process of a new arch-shaped CSB appears for $n_{\mathrm{FOP}} = 4 \to 5$ can be seen from the cases (a) $a = -0.15$, (b) -0.20, and (c) -0.22. The germ-shaped CSB (marked with 5' in the figure) bifurcates from the leftmost arch-shaped CSB reg(5) ($a = -0.15$), elongates with pushing reg(4) ($a = -0.20$), and touches the θ-axis. Then, reg(5) becomes the lowest stratum of the new 5th CSB. In a similar process, reg(6) becomes the lowest stratum of the 6th CSB in a sequence of the cases (d) $a = -0.25$, (e) -0.28, (f) -0.30, and (g) -0.31.

The organisation (31) says that when the new CSB appears, the second and upper regions of all CSB have to be replaced by new regions moved from other places: for example, the leftmost CSB reg$(1, 5, 9, 13, \cdots)$ changes into reg$(1, 6, 11, 16, \cdots)$, when $n_{\mathrm{FOP}} = 4 \to 5$. There take place two kinds of process at the same time. Regions reg(5), reg(9), ... move off, whereas regions reg(6), reg(11), ... move in. The germ-shaped CSBs are the form of these regions when they travel between one sector to another sector. A bifurcated CSB is composed of the second and upper regions of the original one and appears at the left-next sector to the sector the original being in (**[FALSE] if the original is in the leftmost sector, the bifurcated go back to the rightmost sector). Each region moves to the appropriate sector according to this rule. We make the schematic diagram for the re-organisation of CSB based on the rule on Fig.5.1. This diagram shows the case $n_{\mathrm{FOP}} = 4 \to 5$. Let us pick up the bifurcations for the re-organisation of the leftmost CSB (in the first sector). reg(6) is imported by the bifurcation reg$(2, 6, 10, 14) \to$ reg$(6, 10, 14)$. reg(11) is imported to the 2nd sector by reg$(3, 7, 11, 15) \to$ reg$(7, 11, 15)$ once, then imported to the first sector by reg$(7, 11, 15) \to$ reg$(11, 15)$. Similarly, reg(16) is transported to the 1st via the 3rd

and 2rd sectors. With decreasing a, the second and upper regions of each CSB shrink and finally vanish. Then the first strata of CSBs in a block becomes a new arch-shaped CSB. As we can see from each case in Fig.8, only one or two of series of branches and one or two regions of the branches are visible at one mass parameter. Therefore, we cannot confirm the correctness of the rule for the bifurcation, and however, we show the Poincaré section for $a = -0.17$ in Fig.5.1, which is selected to see as many series of bifurcations as possible.

5.2 Symmetric case 2: $n_{\mathrm{FOP}} = 3$

We deal with the remaining symmetric case, $n_{\mathrm{FOP}} = 3$. We show, with increasing a in Fig.10, the change of the Poincaré section for this case. The process that the Poincaré section changes is different from that for $n_{\mathrm{FOP}} \geq 4$. At $a \backsimeq 0.4$, the Schubart region vanishes and changes its orientation when it re-appears, that is, the Schubart region takes triangular shape at around $a \backsimeq 0.4$ looking upward ($a \lesssim 0.4$) and downward ($a \gtrsim 0.4$). The process of change is divided into $a \lesssim 0.4$ and $a \gtrsim 0.4$ cases. For the former case, if a is decreased until $a = a_{3,4} = 0.019823$, then n_{ACS} changes from 3 to 4 in a similar way as n_{ACS} changes from n to $n + 1$ for $n \geq 4$.

However the triple system is far from total degeneracy at around $a = -0.4$, even though arch-shaped CSBs are well stratified, $n_{\mathrm{ACS}} = 3$, and organised in $n_{\mathrm{mod}} = 3$. This is the reason why we separated this case from the scenario shown in the opening of Sect.5. In order to confirm the process, we give Fig.10 (a) $a = 0.1$, (b) 0.3, (c) 0.4, (d) 0.5. In (c) $a = -0.4$, the almost vanishing Schubart region is seen. The cases (b) $a = 0.3$ and (c) $a = 0.4$ show the change of orientation of the Schubart region at $a \backsimeq 0.4$ and the well stratified CSBs at around $a = 0.4$. Finally, at (a) $a = 0.1$, the bifurcations for $n_{\mathrm{ACS}} = 3 \to 4$ are seen: $\mathrm{reg}(7, 10, \cdots)$, $\mathrm{reg}(10, 13, \cdots)$, and others are bifurcated.

Now, we consider the latter case, $a \gtrsim 0.4$. As we have seen in the case (d) $a = 0.5$, the extent of the structure like $a = 0.4$, so the feature of this case appears at $a \backsimeq 0.7$. The process of the bifurcations for $a \backsimeq 0.7$ is very complicated. In order to follow the process, We take values of a at small intervals and show the Poincaré section for them in (e) $a = 0.70$, (f) 0.75, (g) 0.78, (h) 0.80, (i) 0.82, (j) 0.85, (k) 0.88, (ℓ) 0.90, (m) 0.92, (n) 0.99, and (o) 0.9999 of Fig.10. However, if we look at only terminals cases, the CSBs composed according to $n_{\mathrm{mod}} = 3$ at (c) $a = 0.40$ becomes to be composed according to $n_{\mathrm{mod}} = 2$ at $a = 1$, and required transportation of the regions are also accomplished by the bifurcations of the regions. The difference to $n_{\mathrm{FOP}} \geq 4$ case is that it is the change from $n_{\mathrm{ACS}} = 3$ to 2 with increasing a. (This difference does not mean simply that n_{ACS} decreases because of the reversed process for the reversed change in a to that for $n_{\mathrm{FOP}} \geq 4$. If the fact were so, the process might proceed so that the regions inside a arch-shaped CSB disintegrated and were taken in different germ-shaped CSBs. Instead, the Poincaré section (e)-(o) shows that germ-shaped blocks bifurcate.) For example, let us follow the transportation of $\mathrm{reg}(6)$. This region is inside the 3rd arch-shaped CSB
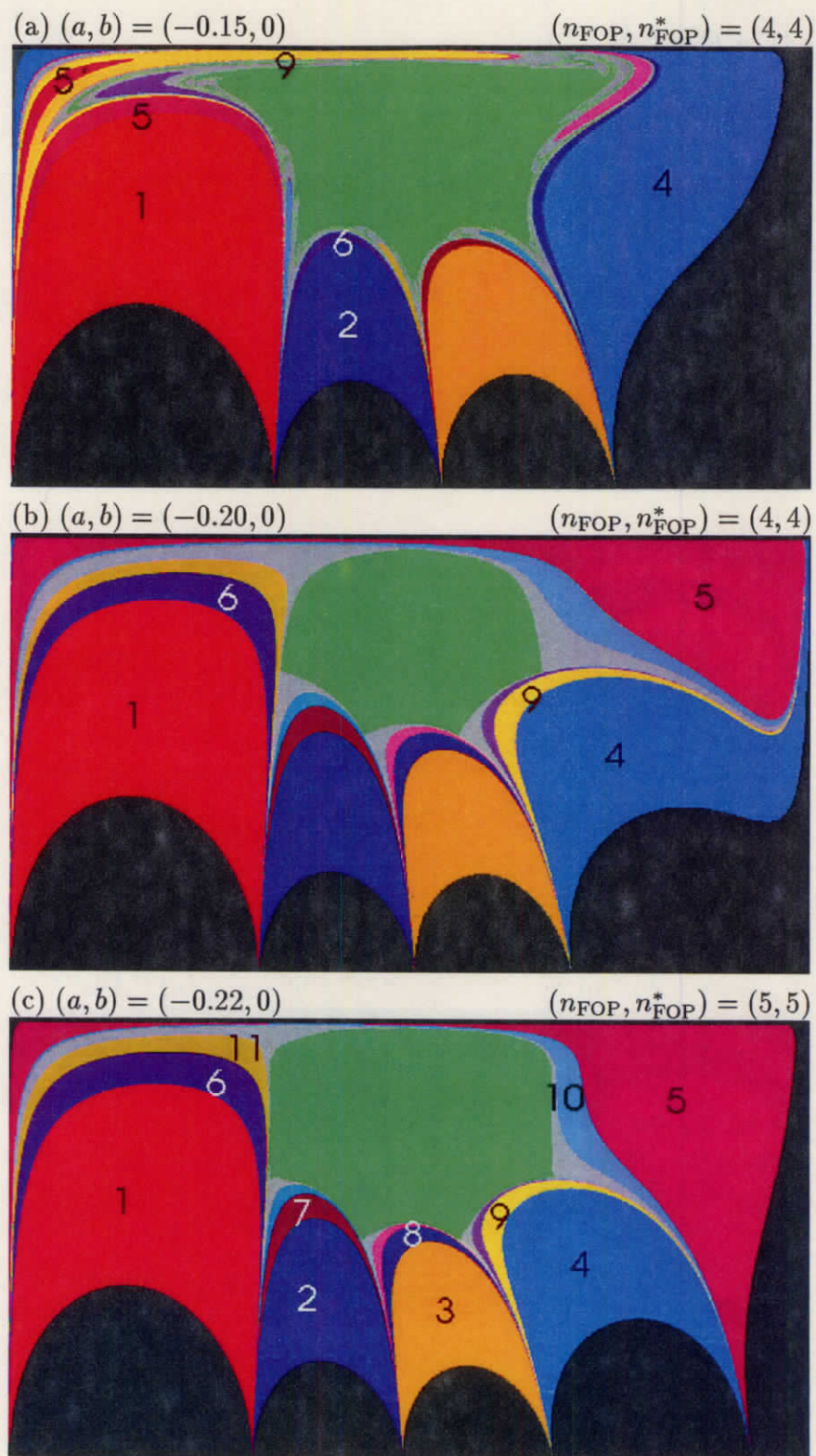
(a) $(a, b) = (-0.15, 0)$ $(n_{FOP}, n^*_{FOP}) = (4, 4)$

(b) $(a, b) = (-0.20, 0)$ $(n_{FOP}, n^*_{FOP}) = (4, 4)$

(c) $(a, b) = (-0.22, 0)$ $(n_{FOP}, n^*_{FOP}) = (5, 5)$

Figure 8: The partition of the Poincaré section(Symmetric, $n_{root} \geq 4$)

(d) $(a, b) = (-0.25, 0)$ $(n_{\text{FOP}}, n^*_{\text{FOP}}) = (5, 5)$

(e) $(a, b) = (-0.28, 0)$ $(n_{\text{FOP}}, n^*_{\text{FOP}}) = (5, 5)$

(f) $(a, b) = (-0.30, 0)$ $(n_{\text{FOP}}, n^*_{\text{FOP}}) = (5, 5)$

Figure 8: (continue)

(f) $(a, b) = (-0.31, 0)$ $(n_{\text{FOP}}, n^*_{\text{FOP}}) = (6, 6)$
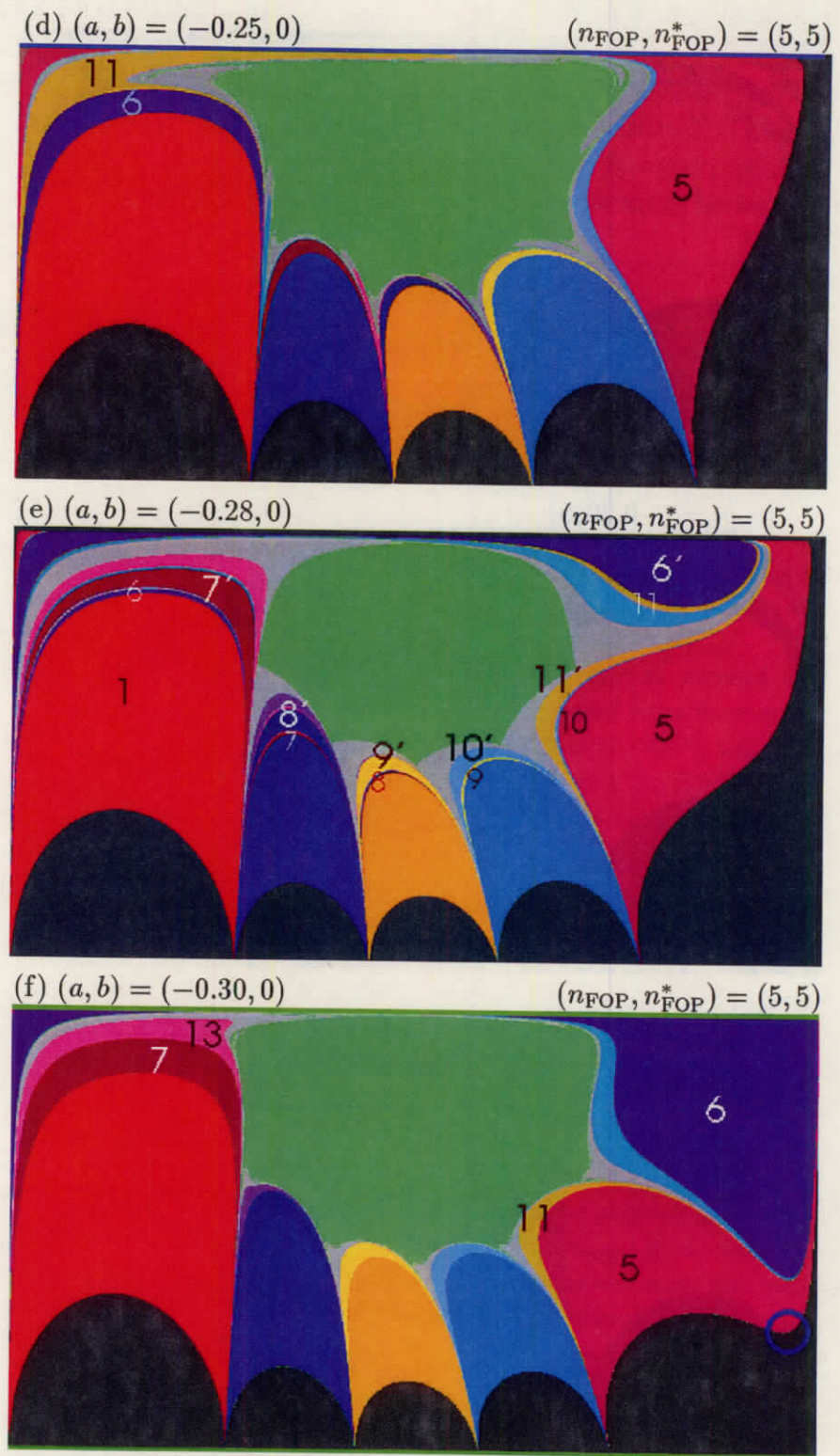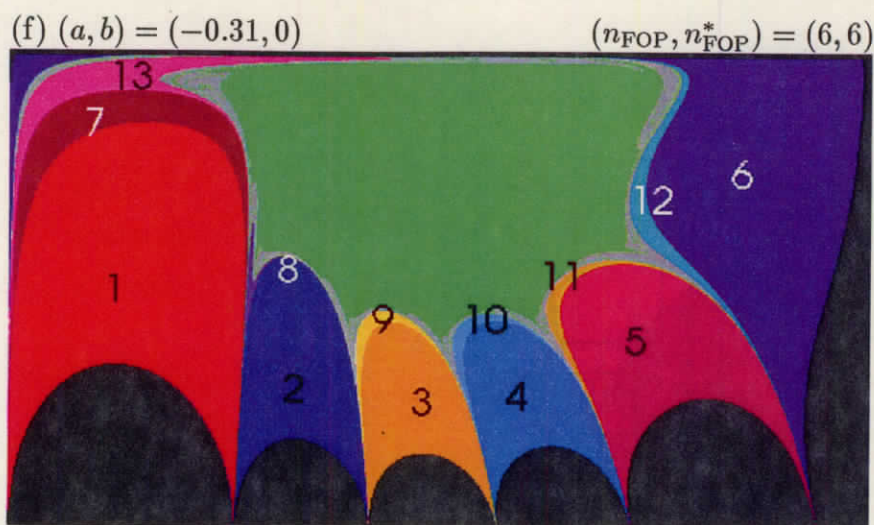
Figure 8: (continue)

from the left, $\text{reg}(3, 6, 9, \cdots)$, at $a = 0.40$. This block is distorted at a place above the 1st CSB ((e),(f) $a = 0.70, 0.75$), a 'branch' that bifurcates from the point piles up on the 1st CSB((g-i) $a = 0.78 - 0.82$). This 'branch' is still connected to the original CSB. Among the cases shown here, the branch separates from the original CSB at (k) $a = 0.88$. The $\text{reg}(3)$ appears under the lowest strata $\text{reg}(6)$ of the branch, its composition becomes the same as that of the original CSB. For this point, we can consider that $\text{reg}(3)$ was already included in the branch at the bifurcation, but was invisible, then grows so as to be visible at $a = 0.85$. From the point of view, we can explain the bifurcation and the transportation of $\text{reg}(6)$ and other regions with the simple rule that a block bifurcating from a CSB contains the second and upper strata of the original block and appears in the left-neighbouring sector to that of the original block (For the rightmost block, the branch contains all regions and appears in the leftmost sector). The $\text{reg}(6)$ stays for some interval of a, then piles up on the 2nd arch-shaped CSB at (n) $a = 0.99$. As going to $a = 1$, the 3rd arch-shaped CSB becomes invisible, and the compositions of the rest of CSBs becomes $\text{reg}(1, 3, 5, 7, \cdots)$ and $\text{reg}(2, 4, 6, 8, \cdots)$. However, these two blocks are not completed until $a = 1$ (while m_1/m_0 being finite). We can confirm at (o) $a = 0.999$ that $\text{reg}(4)$, $\text{reg}(6)$, and $\text{reg}(8)$ are still germ-shaped independent block.

5.3 Asymmetric case 1: $(n_{\text{FOP}}, n^*_{\text{FOP}}) = (3, 4)$

Looking at area being $n_{\text{FOP}} \neq n^*_{\text{FOP}}$ on the mass-triangle shown in Fig.7, one find that $n_{\text{FOP}} = 2\ell - 1$ and $n_{\text{FOP}} = 2\ell$ with $\ell \geq 2$. The area being $(n_{\text{FOP}}, n^*_{\text{FOP}}) = (3, 4)$, which we take up in this section, is the main area of these. The Poincaré section for these area is
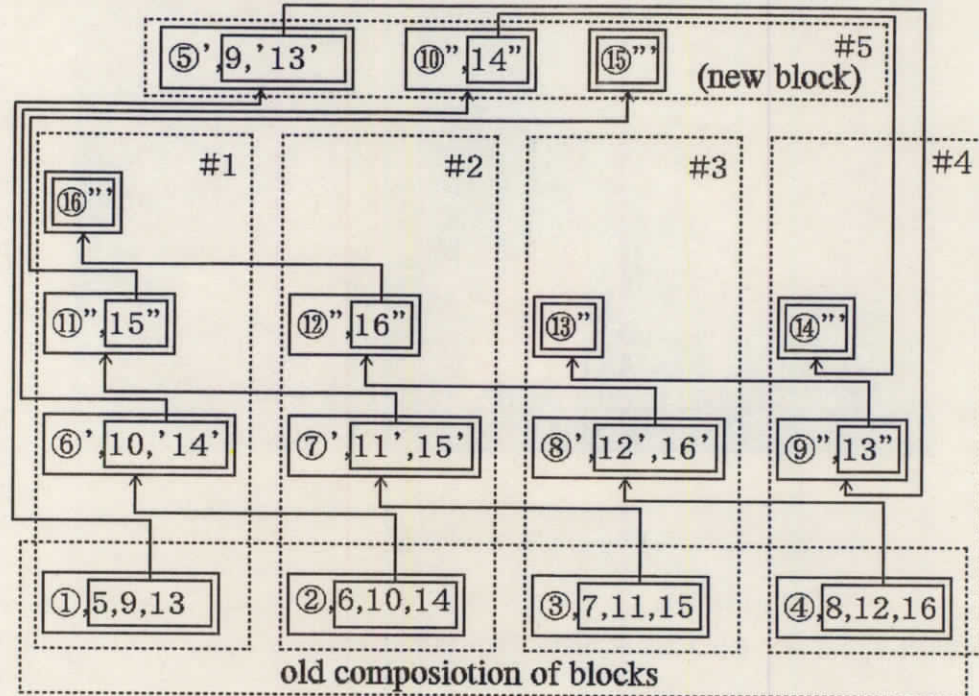
32

(a) schematic diagram

(b) instance for $(a, b) = (-0.17, 0)$

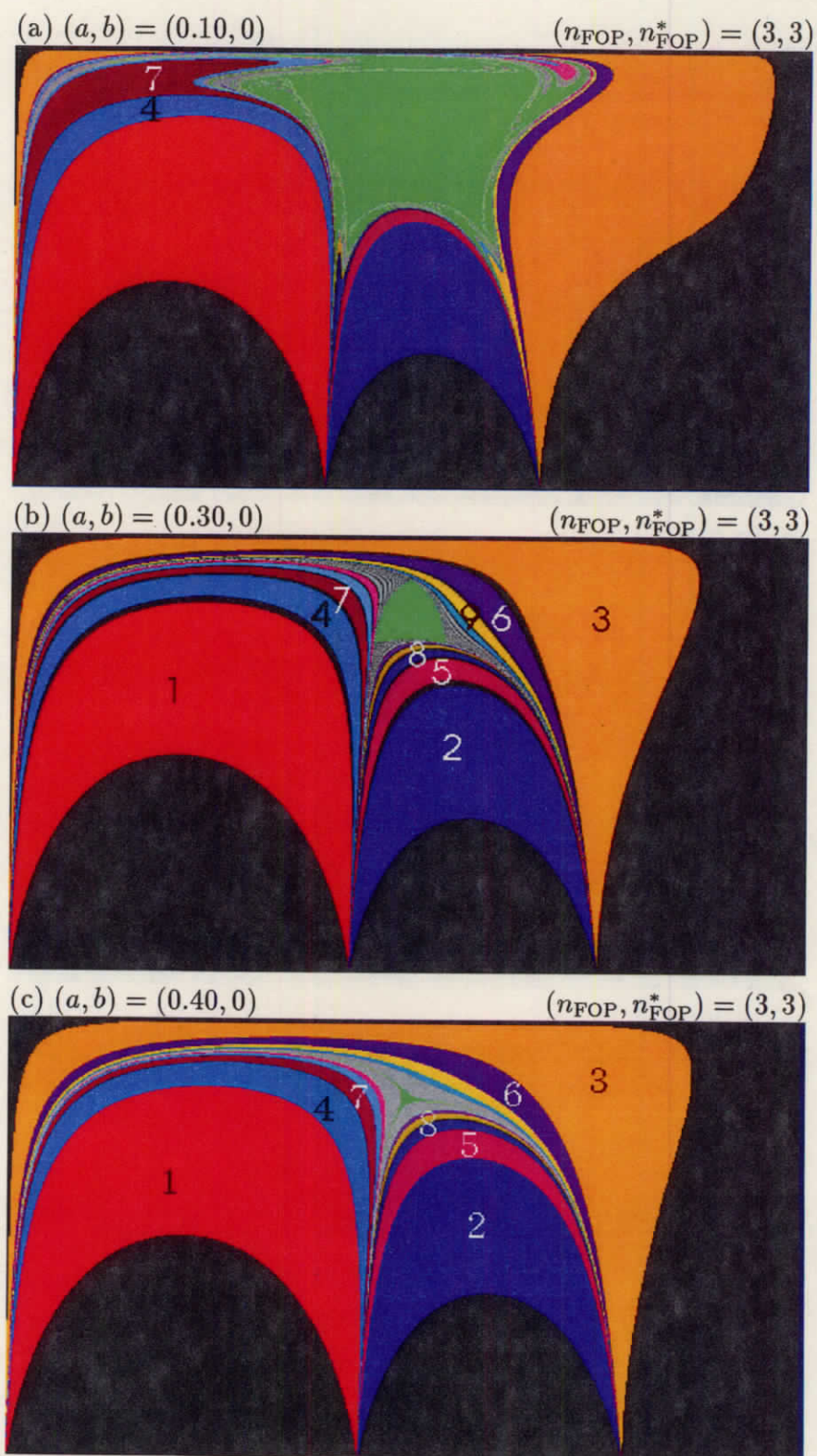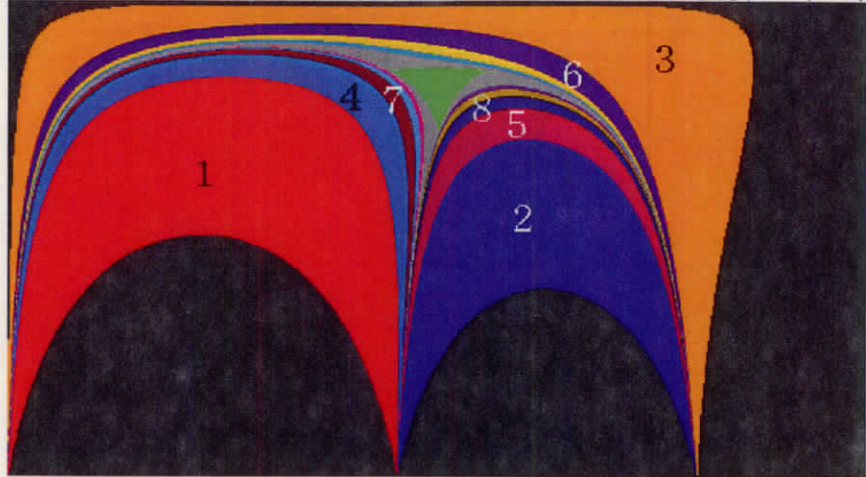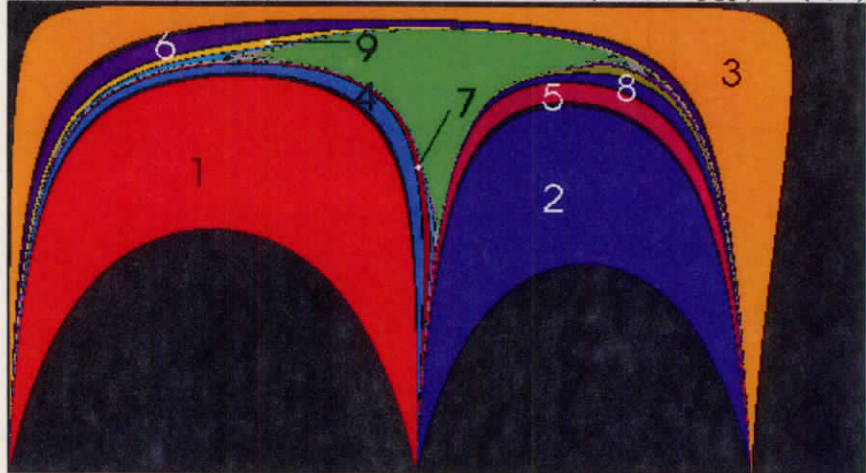Figure 9: The Bifurcation and Composition Change of Arch-shaped CSB

Figure 10: The partition of the Poincaré section(Symmetric, $n_{FOP} = 3$)

34

(d) $(a, b) = (0.50, 0)$ $\qquad$ $(n_{\text{FOP}}, n_{\text{FOP}}^*) = (3, 3)$

(e) $(a, b) = (0.70, 0)$ $\qquad$ $(n_{\text{FOP}}, n_{\text{FOP}}^*) = (3, 3)$

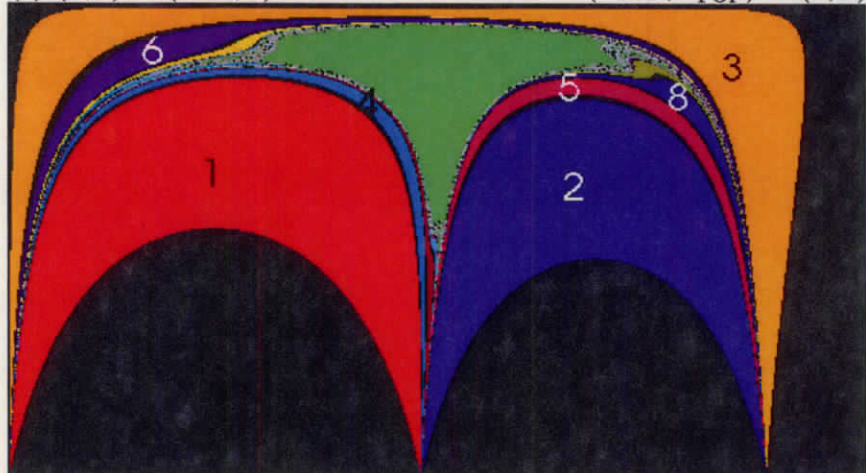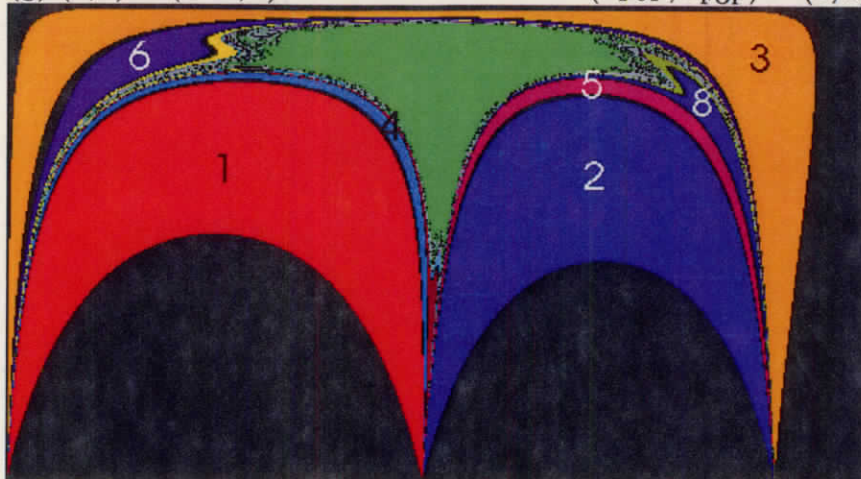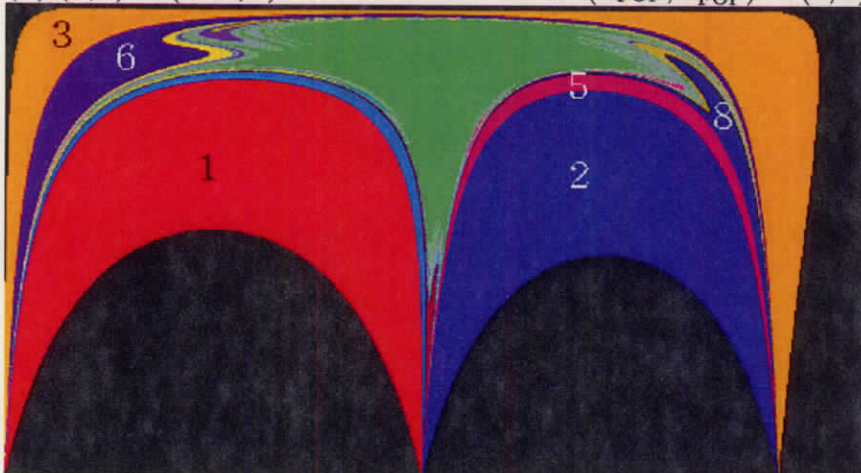(f) $(a, b) = (0.75, 0)$ $\qquad$ $(n_{\text{FOP}}, n_{\text{FOP}}^*) = (3, 3)$

Figure 10: (continue)

(g) $(a, b) = (0.78, 0)$ $(n_{\text{FOP}}, n_{\text{FOP}}^*) = (3, 3)$

(h) $(a, b) = (0.80, 0)$ $(n_{\text{FOP}}, n_{\text{FOP}}^*) = (3, 3)$

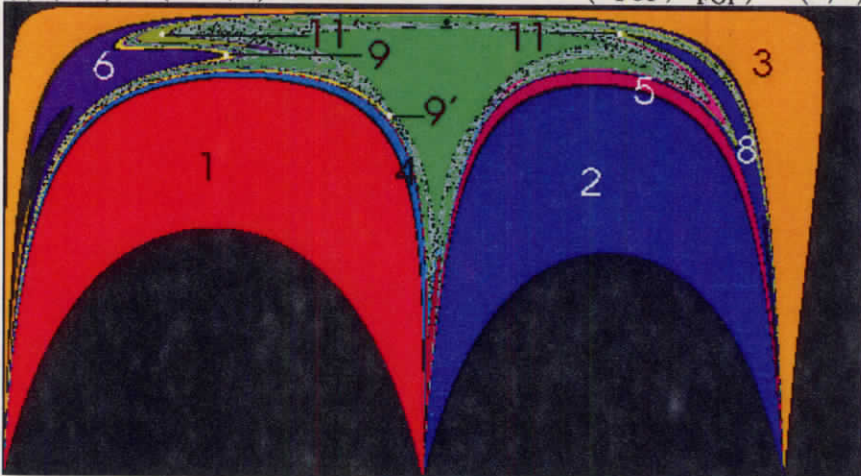(i) $(a, b) = (0.82, 0)$ $(n_{\text{FOP}}, n_{\text{FOP}}^*) = (3, 3)$
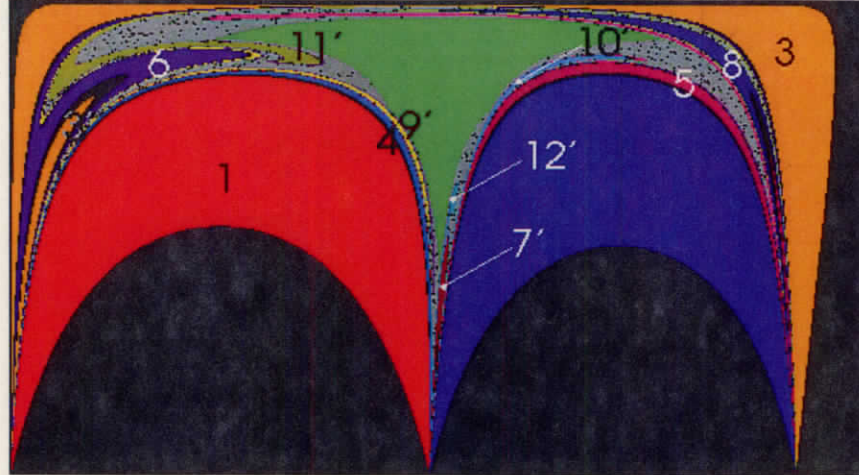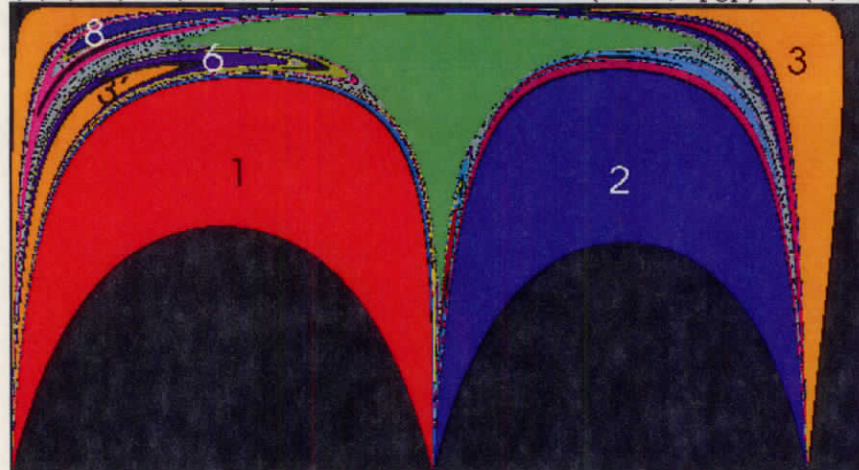

Figure 10: (continue)

(j) $(a, b) = (0.85, 0)$ $(n_{\mathrm{FOP}}, n_{\mathrm{FOP}}^{*}) = (3, 3)$

(k) $(a, b) = (0.88, 0)$ $(n_{\mathrm{FOP}}, n_{\mathrm{FOP}}^{*}) = (3, 3)$

(ℓ) $(a, b) = (0.90, 0)$ $(n_{\mathrm{FOP}}, n_{\mathrm{FOP}}^{*}) = (3, 3)$

Figure 10: (continue)

(m) $(a, b) = (0.92, 0)$ $(n_{\mathrm{FOP}}, n_{\mathrm{FOP}}^*) = (3, 3)$

(n) $(a, b) = (0.99, 0)$ $(n_{\mathrm{FOP}}, n_{\mathrm{FOP}}^*) = (3, 3)$

(o) $(a, b) = (0.9999, 0)$ $(n_{\mathrm{FOP}}, n_{\mathrm{FOP}}^*) = (3, 3)$
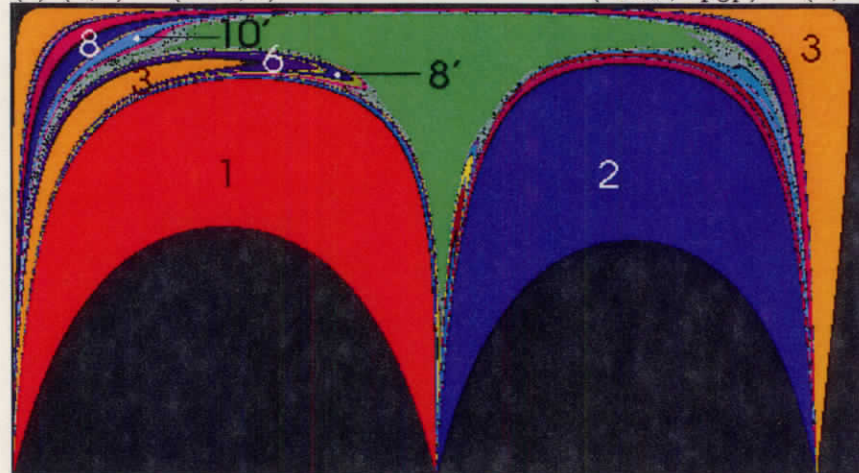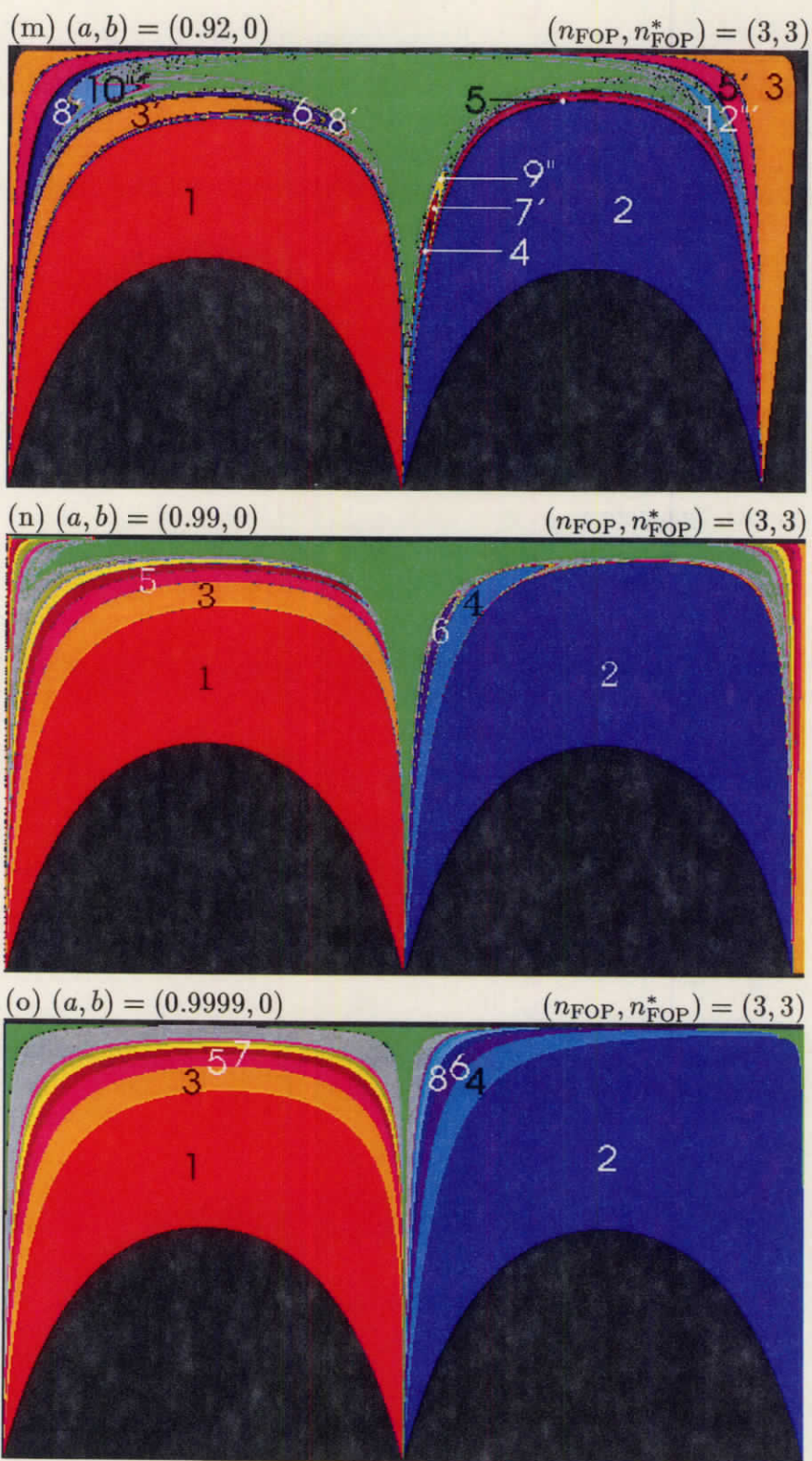
Figure 10: (continue)

shown in Fig.11.

Now, we begin to look at $(n_{\text{FOP}}, n^*_{\text{FOP}}) = (3,4)$ with increasing the asymmetry b. From the cases $(a,b) = (0,0.1)$ and $(-0.1,0.4)$, it is found that reg(c) with even c shrink with increasing b. In a more asymmetric case $(-0.1,0.4)$, the region $c = 10$ disappears. If the system becomes more asymmetric, regions with even number, except $c = 2$, finally disappear. In these two cases, arch-shaped CSBs are organised according to $n_{\text{mod}} = 4$, but $n_{\text{FOP}} = 3$ for the rightmost CSB rising up. If considering that these mass cases are just above the border for n_{FOP}, we can find that the shape taken by the Poincaré section just above the border is the same as one at symmetric case (e.g. $(a,b) = (-0.20,0)$ in Fig.8). However, the behaviour of reg(4, 8, $\cdots$), rising up from the θ-axis, is different from the symmetric case. In the symmetric case, such regions are together as one germ. However, these regions are disrupted in $(a,b) = (0,0.1)$ (reg(8) is too small to be seen in $(-0.1,0.4)$). Similar disruptions are seen in the second CSB from the left: reg(6) and reg(10) are independent germs.

Here, we describe the structure around these germs. This structure is fine but important in case asymmetric and $n_{\text{FOP}} \neq n^*_{\text{FOP}}$. We show the Poincaré section of $(0,0.1)$ magnified around reg(6) next to the original one. reg(2,6,10) are enclosed by regions including reg(5,9,13). For the time being, we call reg(2,6,10) *enclosee* and reg(5,9,13) *encloser*. Because of the enclosure, the enclosee are isolated from the global structure of the arch-shaped CSB. Note that the enclosee have even region number, and the encloser have an odd region number. The regions reg(5,9,13) bifurcate into two or more branches. One branch is a part of the leftmost CSB. The other branches are encloser. The correspondence between the enclosee and encloser is summarised on Table 2. This is generalised

enclosee	encloser
reg(2)	reg(5,9,13,$\cdots$)
reg(6)	reg(9,13,$\cdots$)
reg(10)	reg(13,$\cdots$)

Table 2: The relation between enclosees and enclosers

into the relation that reg($4i+2$) with $i \geq 1$ is enclosed by reg($\{4j+2+3 | j \geq i\}$). A similar relation is seen also between reg(4, 8, 12, $\cdots$) and reg(7, 11, $\cdots$). In this case, reg($4i$) with $i \geq 1$ is enclosed by reg($\{4j + 3 | j \geq i\}$). This relation shall be discussed in the next section.

We come back to the Poincaré section changing with increasing b. The regions with even number except reg(2) do not exist at $(0,0.2)$, and for each of reg(5,9,13) or reg(7,11), its branches are united. In this mass case, curve of strata is wavy, however it is relaxed as increasing. Then, the Poincaré section reaches the shape seen in $(0.0.5)$. Even if b increases more, there is nothing more than reg(c) and reg((c, ∞)) with even c become small and with odd c become large. Which is known from show $(a,b) = (0,0.6)$ and

$(-0.2, 0.8)$. In order to know the limit case $(0, 1)$, where m_1 is mass-less particle, we show the case $(0, 0.99)$. The Poincare section is almost occupied by the escape regions $reg((1, \infty))$ and $reg((3, \infty))$. In these mass parameters, the arch-shaped CSBs are well stratified in spite of being distant from the border for (n_{FOP}, n_{FOP}^*). As mentioned in the above, these mass parameters are located in rather inside of mass area that the Schubart region is linearly unstable. It implies that the well stratification is related to the instability of the Schubart region also in these case.

5.4 Asymmetric case 2: $n_{FOP}, n_{FOP}^* \geqq 4$

In 5.1 and 5.2, we have seen the change of the Poincaré section dependent on the parameter a, when symmetric. In this subsection, we watch how the change is modified when the asymmetric b is high. In Fig.12, we show Poincaré sections for mass parameters from $a=-0.390$ to 0.432 with fixed $b=1.0$ (only for a=-0.39, b=0.9), which correspond to mass areas from $(n_{FOP}, n_{FOP} *) = (4, 4)$ to $(7, 8)$.

At the mass case $(a, b) = (-0.39, 0.9)$, where (n_{FOP}, n_{FOP}^*) is (4,4), there are no special difference except the shrinkage of regions with even number. At $(-0.40, 1.0)$, where (n_{FOP}, n_{FOP}^*) is (5,6), regions with even c does not exist. At $(-0.41, 1.0)$, where is little above the border to $(n_{FOP}, n_{FOP}^*) = (6, 6)$, regions with even number recover. In this case, even if the sixth arch-shaped CSBs is not completed, the bifurcation of reg(7,13) for the seventh CSBs appears. At (-0.4227,1.0), which is on the border between $(n_{FOP}, n_{FOP}^*) = (6, 6)$ and $(7, 7)$, the CSBs with reg(9),reg(11), or reg(13) curl and trail to their left CSB, and regions reg(8), reg(10), and reg(12) look as if they were piled up on by reg(9), reg(11), or reg(13), respectively. The regions reg(8,10,12) are very thin, but they do not disappear while $(n_{FOP}, n_{FOP}^*) = (7, 7)$. At $(-0.432, 1.0)$, where $(n_{FOP}, n_{FOP}^*) = (7, 8)$, the tip of curling regions reach the root and pairs of CSBs with reg(1,2), reg(3,4), or reg(5,6) are united, respectively. The regions reg(8,10,12) disappear and reg(1,9), reg(3,11), and reg(5,13) are directly connected, respectively.

From the above observation, it seems that (1) cycles for creation of a arch-shaped CSB becomes ambiguous if the asymmetry b becomes high, and (2) the regions with even number disappears only when $n_{FOP} \neq n_{FOP}^*$.

5.5 Asymmetric case 3: $n_{FOP} = n_{FOP}^* = 3$

Finally, the asymmetric case being $n_{FOP} = n_{FOP}^* = 3$ is show in Fig.13. In this case, there are no more difference to symmetric case than the Schubart region distorting and the regions with even number shrinking. For any values of b, the Schubart region disappears near $a = 0.4$. The Poincaré section is well stratified in and around the mass parameter: for example, the Poincaré section of $(a, b) = (0.3, 0.6)$, $(0.4, 0.2)$, and $(0.6, 0.3)$ are shown in the figure. When a becomes large, the bifurcation of the regions appears ($(a = 0.8, b =$

40

(a) $(a, b) = (0, 0.1)$
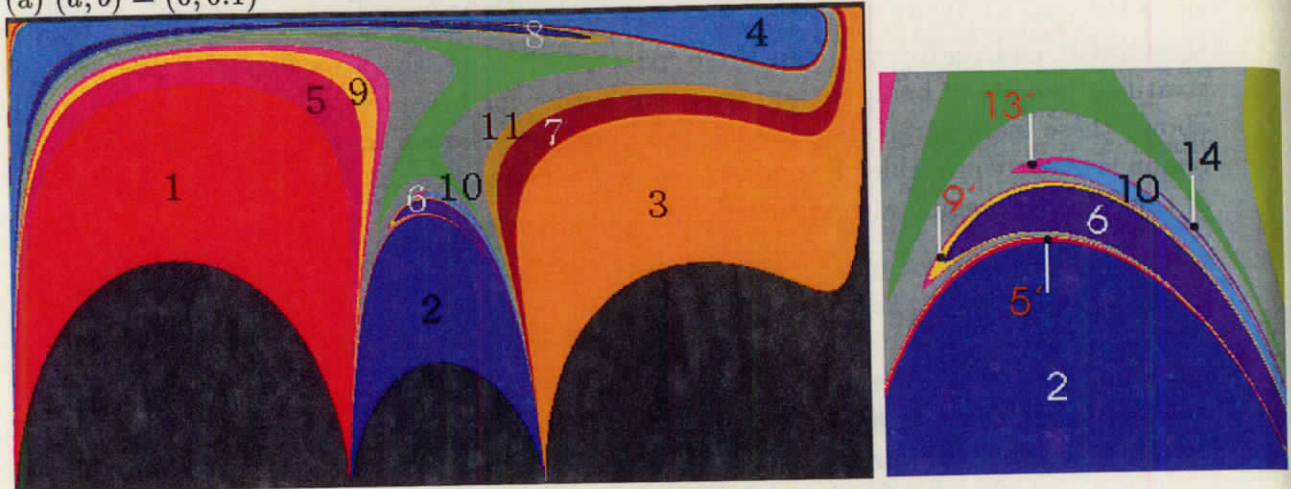
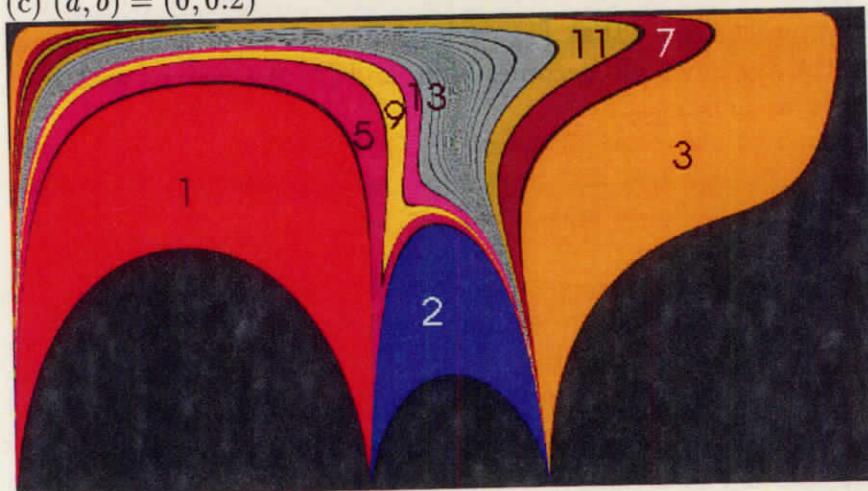(b) $(a, b) = (-0.1, 0.4)$
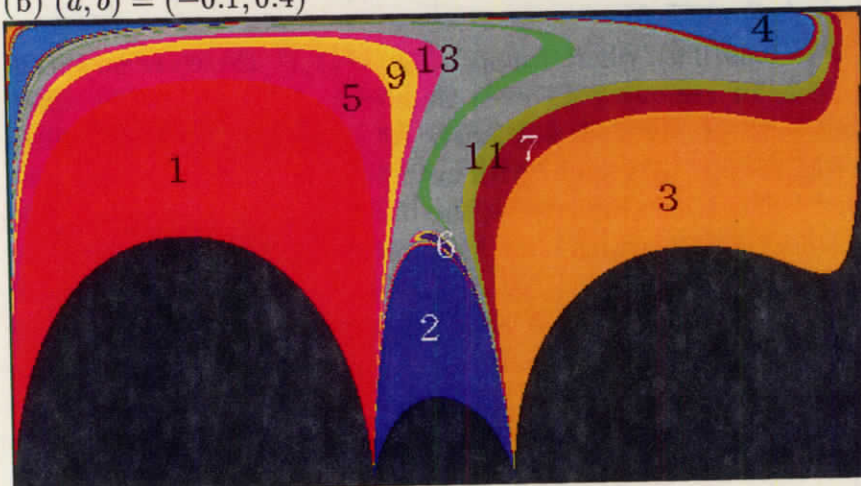
(c) $(a, b) = (0, 0.2)$

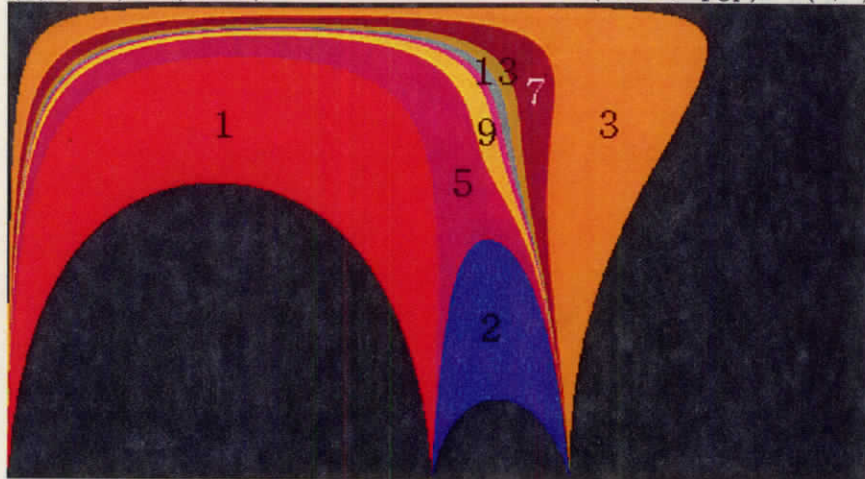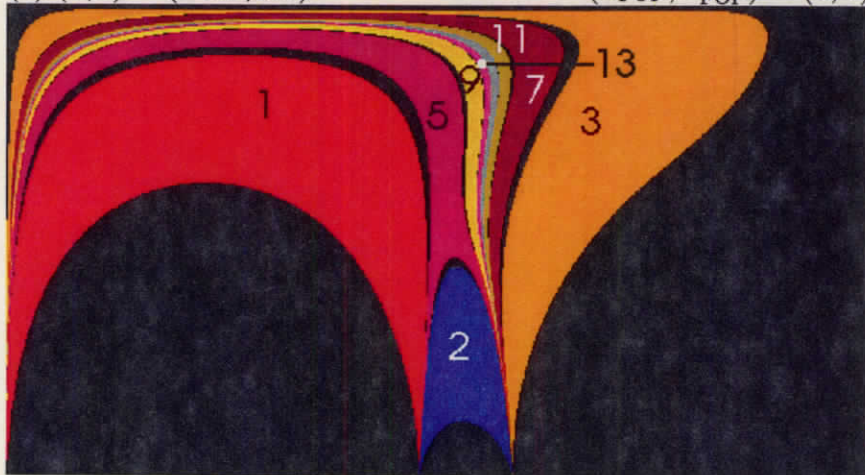Figure 11: The partition of the Poincaré section(Asymmetric, the number of roots is different in both side of the Poincaré section)

(d) $(a, b) = (0, 0.5)$ $(n_{\text{FOP}}, n_{\text{FOP}}^*) = (3, 4)$

(e) $(a, b) = (-0.2, 0.8)$ $(n_{\text{FOP}}, n_{\text{FOP}}^*) = (3, 4)$

(f) $(a, b) = (0, 0.99)$ $(n_{\text{FOP}}, n_{\text{FOP}}^*) = (3, 4)$

Figure 11: (continue)

(a) $(a,b) = (-0.3000, 0.9)$ $(n_{\text{FOP}}, n_{\text{FOP}}^*) = (4,4)$

(b) $(a,b) = (-0.4000, 1.0)$ $(n_{\text{FOP}}, n_{\text{FOP}}^*) = (5,6)$

(c) $(a,b) = (-0.4100, 1.0)$ $(n_{\text{FOP}}, n_{\text{FOP}}^*) = (5,6)$

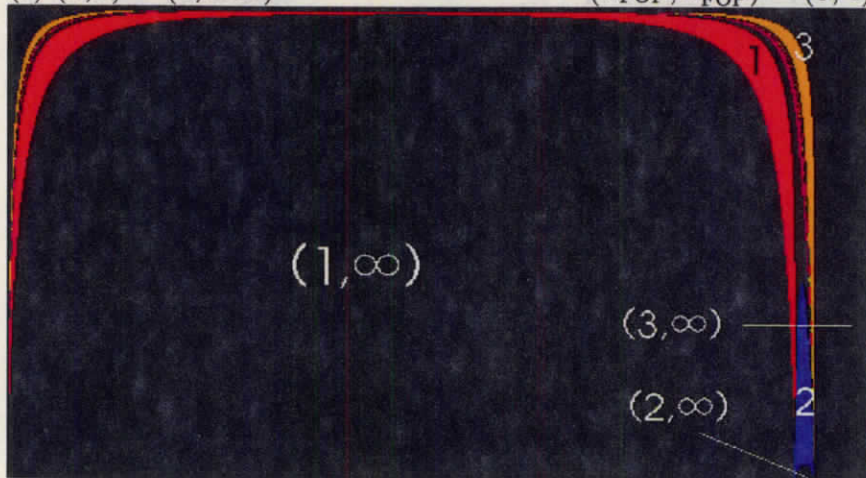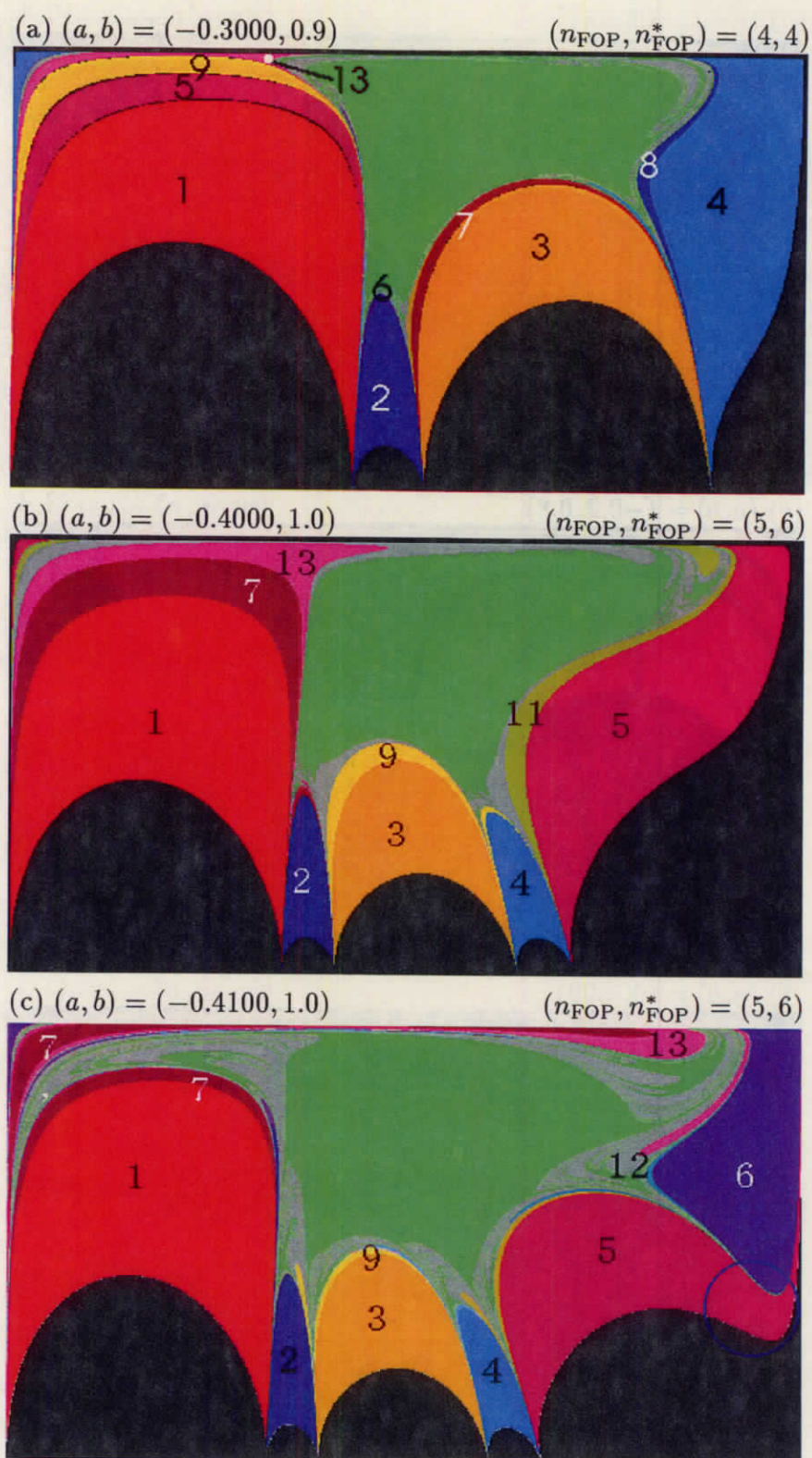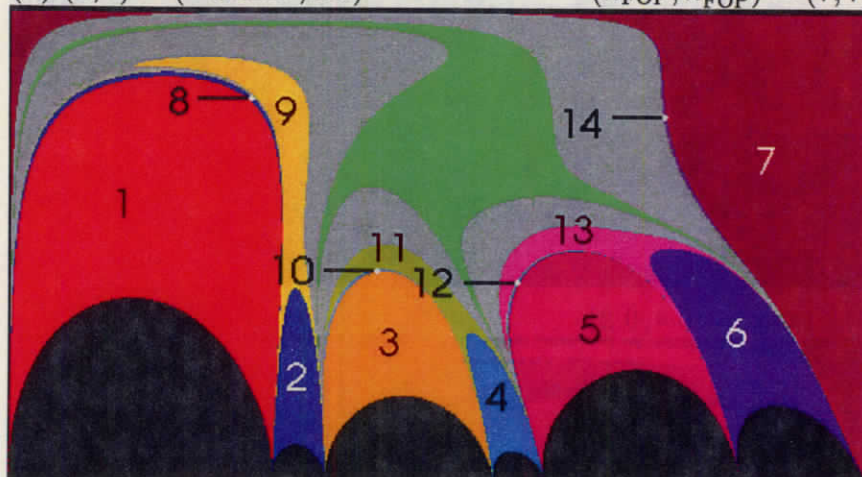Figure 12: The partition of the Poincaré section (Asymmetric, the dependency on the parameter a)

(d) $(a, b) = (-0.4227, 1.0)$ $(n_{\mathrm{FOP}}, n_{\mathrm{FOP}}^*) = (7, 7)$

(e) $(a, b) = (-0.4320, 1.0)$ $(n_{\mathrm{FOP}}, n_{\mathrm{FOP}}^*) = (7, 8)$
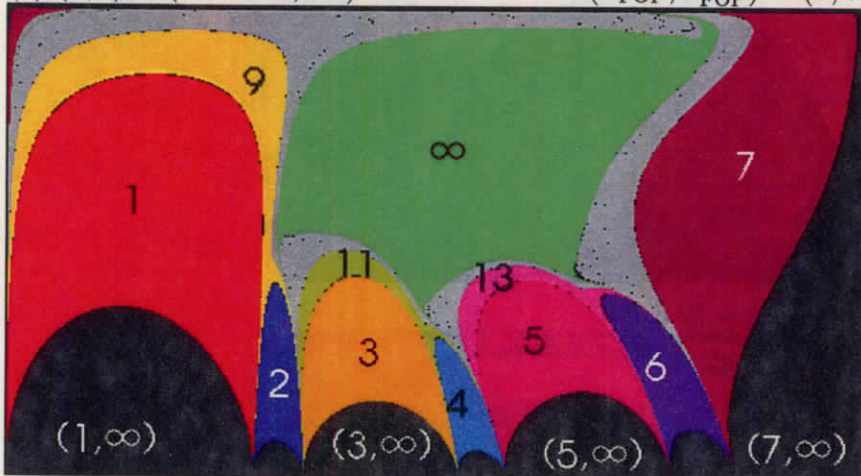
Figure 12: (continue)

44

Figure 13: The partition of the Poincaré section(Asymmetric, $n_{\text{FOP}} = n^*_{\text{FOP}} = 3$)

(d) $(a, b) = (0.8, 0.1)$ $(n_{\text{FOP}}, n_{\text{FOP}}^*) = (3, 3)$

Figure 13: (continue)
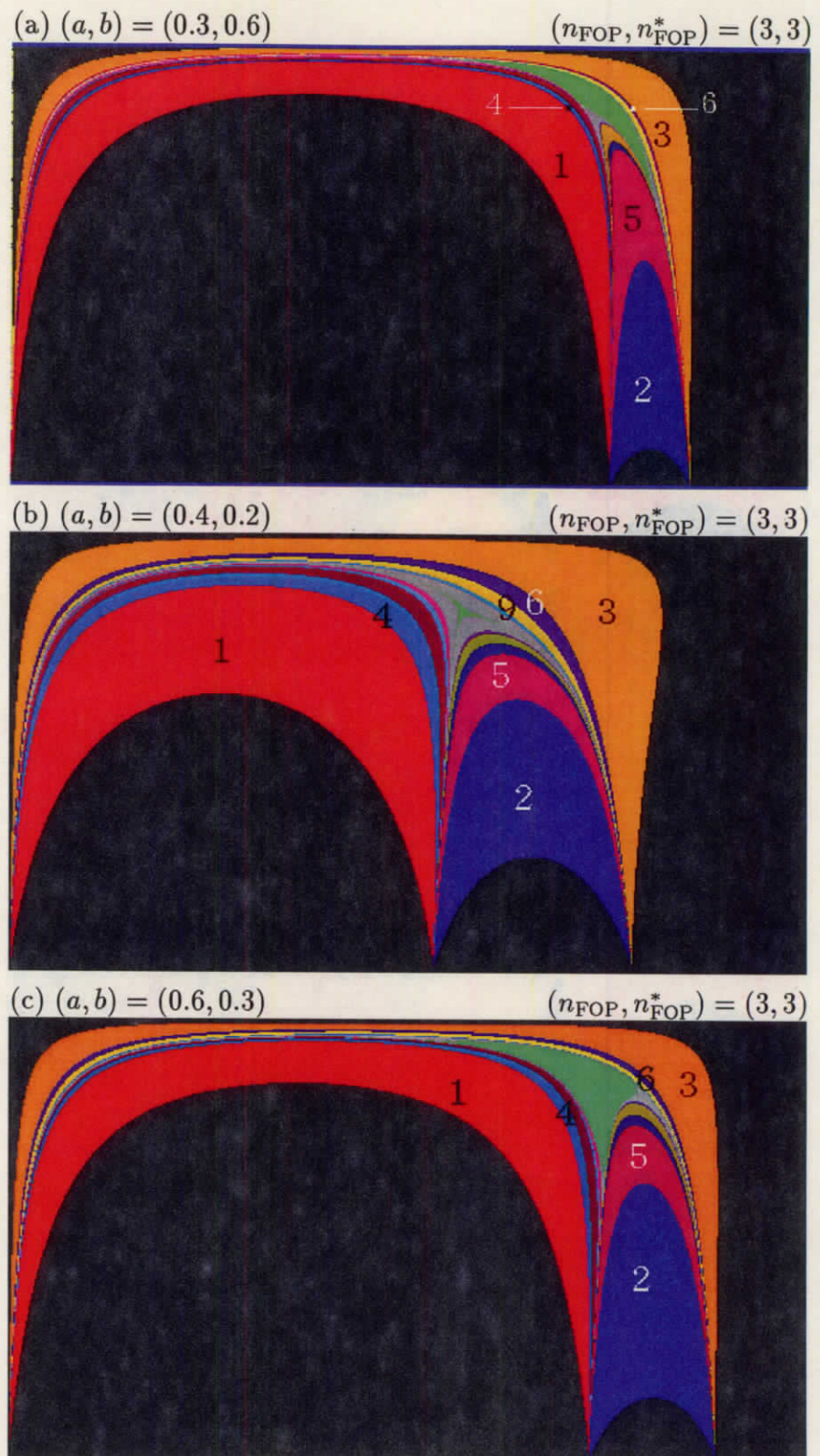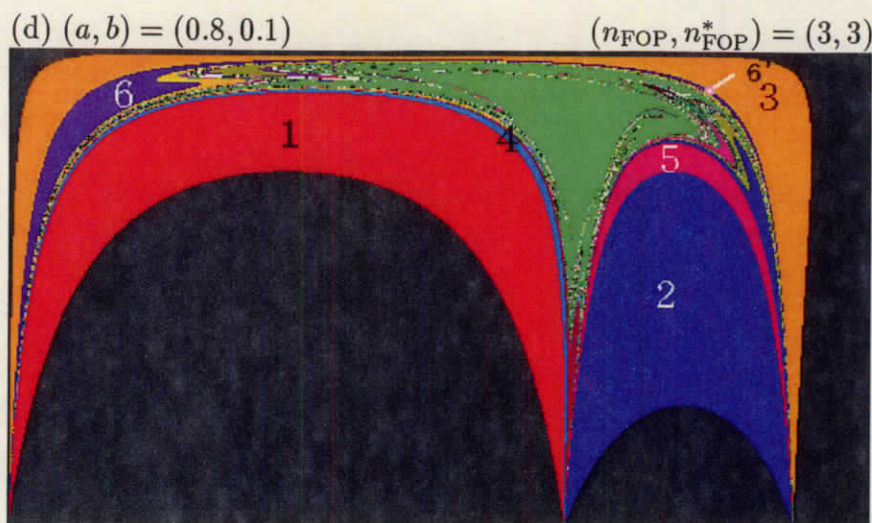
0.1)). The number n_{ACS} seems to be 2 at the limit value of a, $a = 1 - b$, at which m_1 is 0.

6   Interpretation of Results

In the previous section, we have observed the structure of the Poincaré section obtained by means of its partition according to symbol sequences. The observation shows the relation between the location of a region $\text{reg}(c)$ in the Poincaré section and the number c. In this section, we try to explain these relations using the flow on the TCM and symbol sequences.

6.1   How $\text{reg}(c)$ with $c > n_{\text{FOP}}$ appear

If the (θ, R)-plane is considered in the McGehee's variables, the θ-axis is connected continuous to $(\theta, R > 0)$. Therefore, we can expect that a fictitious orbit can metamorphose into real orbits without changing its topology. Actually, the foot-points and segments between foot-points on the θ-axis have symbol sequences

$$S_F = \{(21)^i, (21)^i 20, (21)^i (1)^\infty, (21)^i (2)^\infty | i \leqq \text{int}(n_{\text{FOP}}/2), i \in \mathbf{Z}\},$$

and they appear also above the segments and the foot-points. These are just scallops and some triple collision curves. The escaping orbits can metamorphose into ejection orbits continuously, which is analogous to the continuity between hyperbolic and elliptic orbits.

This is the reason why the regions corresponding to

$$S_R = \{(21)^i, (21)^i 20, (21)^i (1)^j, (21)^i (2)^j | i \leq \mathrm{int}(n_{\mathrm{FOP}}/2), i, j \in \mathbf{Z}\}$$

exist and touch the fast escaping regions. Now, we have considered the reason for the existence of regions $\mathrm{reg}((c, \infty))$ and $\mathrm{reg}(c)$ with $c \leq n_{\mathrm{FOP}}$. The $c > n_{\mathrm{FOP}}$ case is considered in the rest of this section.

An arch-shaped block, for example, the leftmost one in the equal mass case, are composed of $\mathrm{reg}(1)$, $\mathrm{reg}(5)$, $\mathrm{reg}(9)$, $\cdots$ from the bottom, as is observed in Sect.5. This relation is going to be explained through the consideration of orbits in McGehee's coordinates. Generally, the regions, such as $\mathrm{reg}(1)$ and $\mathrm{reg}(5)$, are separated by a triple collision curve. In Fig.14, $\mathrm{reg}(1)$ and $\mathrm{reg}(5)$ are separated by the triple collision curve with the symbol sequence 20. The first N-digit of symbol sequence is $(21)^2(2)^{N-4}$ and $2(21)^2(1)^{N-5}$ at 'black bands' over and under the curve, where $N = 64$ according to the specification for symbol sequences written in Sect.2. If N were increased, the corresponding black bands might be narrow. Then, do the bands corresponding to $(21)^2(2)^\infty$ and $2(21)^2(1)^\infty$ appear, when $N \to \infty$? We can confirm that the answer is yes, through the consideration of the orbits in McGehee's coordinates shown in Fig.15 for points on a triple collision curve (the orbit TCO in the figure) and on the both black bands (O180$\mp$). The TCO exists on the the stable manifold of the fixed point c and experience triple collision at c, while O180$\mp$, after the passage near c, approach $W_c^u \pm$. Hence the symbol sequences of O180$\mp$ are

$$s(\mathrm{O}180\mp) = s(\mathrm{TCO})\text{-}s(W_c^u \pm), \tag{32}$$

where $s(\mathrm{TCO})$-0 and $s(W_c^u \pm)$ are the symbol sequences of TCO and $W_c^u \pm$. Generally,

$$s(W_c^u \pm) = \left\{ \begin{matrix} (21)^i \\ (12)^i \end{matrix} \right\} \text{-} \left\{ \begin{matrix} (1)^\infty \\ (2)^\infty \end{matrix} \right\} \tag{33}$$

(see Sect.4.2), where $\{\cdot\}$ denotes that one item is selected from $\cdot$. Therefore, the symbol sequences of O180$\mp$ are that of escaping orbits:

$$s(\mathrm{O}180\mp) = s(\mathrm{TCO})\text{-} \left\{ \begin{matrix} (21)^i \\ (12)^i \end{matrix} \right\} \text{-} \left\{ \begin{matrix} (1)^\infty \\ (2)^\infty \end{matrix} \right\}. \tag{34}$$

We have found that the initial points for triple collision orbits are surrounded by those of escaping orbits in our system. It is contrastive to the case of isosceles three-body system (Tanikawa, Umehara and Abe, 1995). There are two configurations where the orbits experience triple approache but not exact triple collision. In one configuration, the third particle passes through between approaching binary. The acceleration (before passage) to the third particle is smaller than the deceleration (after passage). In the other configuration, the third particle passes through receding binary. The acceleration is larger than the deceleration. Because of this asymmetry, the initial points for triple

collision touch those for both escaping and non-escaping orbits in isosceles three-body system. Now, if we let $s(\text{TCO})\text{-}0=20$, $s(W_c^u+) = (21)^2(1)^\infty$, and $s(W_c^u-) = (12)^2(2)^\infty$, we find

$$s(\text{O}180-) = 2(21)^2(1)^\infty \in S_{(5,\infty)} \quad \text{and} \quad s(\text{O}180+) = (21)^2(2)^\infty \in S_1.$$

Moreover, since $\text{reg}(c,\infty)$, with arbitrary c, touches $\text{reg}(c)$ because of the continuity between escaping and ejection orbits, we find that $\text{reg}(1)$ adjoins $\text{reg}(5)$ via $\text{reg}((5,\infty))$. If we set $s(\text{TCO}) - 0$ general symbol sequences being able to be the border of $\text{reg}(c)$ and $\text{reg}(c')$ (via $\text{reg}((c',\infty))$) and evaluate Eq.(32) or Eq.(34), we can obtain the relation between c and c'. We will do that in the next subsection.
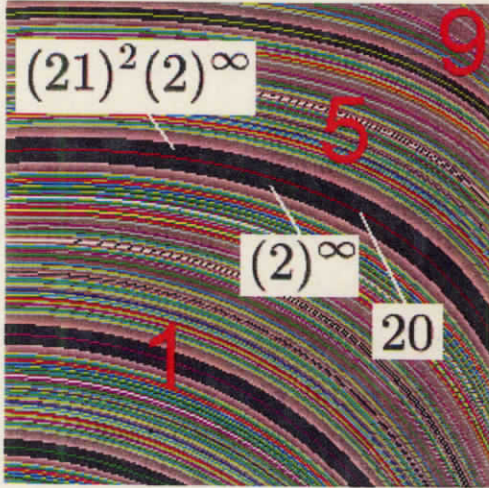

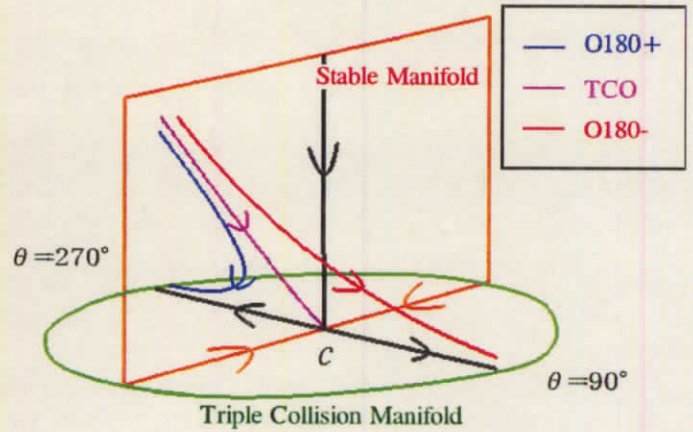Figure 14: Symbol sequences of the triple collision curve and its neighbourhood

Figure 15: A triple collision orbit and orbits of its neighbourhood

6.2 Interpretation for the organisation of arch-shaped CSBs

Since $\text{reg}(c)$ are defined by the repeating number of the word '21' , only triple collisions curve with a symbol sequence whose form is $(21)^k 0$ or $(21)^k 20$ can be the border of regions [2] $\text{reg}(c)$. For such triple collisions, Table 6.2 shows possible concatenation of symbol sequences and their region number. This table is separated into cases of (a) $n_{\text{FOP}} = n_{\text{FOP}}^*$ and (b) $n_{\text{FOP}} \neq n_{\text{FOP}}^*$. First, we explain elements of the table for case (a). The column 'Triple Collision' shows a symbol sequence of a triple collision curve. The column, '$\theta = 180\mp°$ ' shows symbol sequences of $W_c^{u\pm}$. For each item of 'Triple Collision

---

[2]For example, removing '0' from '2220' and concatenating any symbols after that, we obtain only symbol sequences belong to $S_1 \cup S_{1,\infty}$. Therefore, '2220' cannot be a border of regions reg(c).

Orbits' the symbol sequence of W_c^{u+} is shown in the upper row, and W_c^{u-} in the lower row. Since symbol sequences of the branches have different expression selected by the parity of n_{FOP}, Table 6.2 is separated into two cases $n_{\mathrm{FOP}} = 2m$ and $n_{\mathrm{FOP}} = 2m + 1$. The column 'Concatenation', shows the symbol sequences made from the concatenation of 'Triple Collision' and '$\theta = 180 \mp °$', and corresponding region numbers are shown in the column, 'c'. For example, if we look at the pair of rows, $11-$ and $11+$, it is found that the region $c = 2\ell$ and the region $c = 2\ell + 2m$ touch with each other. The others pairs of rows give similar relations, we express these relations as the following:

$$n_{\mathrm{FOP}} = 2m \quad : \quad \text{(i)} \ 2\ell \prec 2\ell + 2m, \ \text{(ii)} \ 2\ell + 1 \prec 2\ell + 1 + 2m$$
$$n_{\mathrm{FOP}} = 2m + 1 \quad : \quad \text{(iii)} \ 2\ell \prec 2\ell + 2m + 1, \ \text{(iv)} \ 2\ell + 1 \prec 2\ell + 2m + 2.$$

These relations are more simplified,

$$c \prec c + n_{\mathrm{FOP}}.$$

This relation shows that each CSB consists of regions whose region numbers are congruent (mod n_{FOP}). Second, we consider the case of (b) $n_{\mathrm{FOP}} \neq n_{\mathrm{FOP}}^*$. In this case $n_{\mathrm{FOP}} = 2m - 1$, and $n_{\mathrm{FOP}}^* = 2m$ for $m \geq 2$, so there are only the case of $n_{\mathrm{FOP}} = 2m + 1$ in Table 6.2(b). From this table, relations of touching regions is

$$\text{(v)} \ 2\ell \prec 2\ell + 2m + 1, \ \text{(vi)} \ 2\ell + 1 \prec 2\ell + 2m + 3.$$

For $\mathrm{reg}(1, \cdots, n_{\mathrm{FOP}})$, the base strata of arch-shaped CSBs, $\mathrm{reg}(c)$ with odd c are accumulated, which comes from applying both of the above relations. For second and upper strata also, $\mathrm{reg}(c)$ with odd c are accumulated, which comes from applying only the relation (vi). This relation about regions touching to each other explains the disappearance of $\mathrm{reg}(c)$ with even c in high asymmetric cases such as $(a, b) = (0, 0.5)$ in Fig.11. These relations do not forbid $\mathrm{reg}(c)$ with even $c > n_{\mathrm{FOP}}$. The left hand side of the relation (v) is even. Hence, $\mathrm{reg}(c)$ with even c can appear as first term in a series of touching regions. However, this series is independent from series of arch-shaped CSBs, whose first terms are $\mathrm{reg}(1, \cdots, n_{\mathrm{FOP}})$. Therefore, $\mathrm{reg}(c)$ with even $c > n_{\mathrm{FOP}}$ are not at least in CSBs. These 'independent even regions' appear in low asymmetric cases such as $(a, b) = (0.1, 0.1)$, as germs intruding to the arch-shaped CSB. In Sect.5.3, we have obtained the observation that these germs consist of a $\mathrm{reg}(c)$ with even c, enclosee, and $\mathrm{reg}(c)$ with odd c enclosing it, enclosers. We have shown the relation about enclosee and enclosers in Table 2. This relation can be derived from the relations (v) and (vi).

7 Summary

We have followed the structural change of the Poincaré section caused by the variation of masses of the particles through the classification of the points on the section according to symbol sequence type. The following is the summary of the Part I.

Table 3: Symbol sequences made with the concatenation of symbol sequences of a triple collision orbit and $W_c^{u\pm}$

(a)$n_{FOP} = n^*_{FOP}$

Label	Triple Collision	$\theta = 180\mp°$	Concatenation	Region c
$n_{FOP} = 2m$				
11− 11+	$(21)^\ell 0$	$(21)^m(1)^\infty$ $(12)^m(2)^\infty$	$(21)^{\ell+m}(1)^\infty$ $(21)^\ell 1 - (21)^{m-1}(2)^\infty$	$2\ell+2m$ 2ℓ
12− 12+	$(21)^\ell 2\,0$	$(21)^m(1)^\infty$ $(12)^m(2)^\infty$	$(21)^\ell 2 - (21)^m(1)^\infty$ $(21)^{\ell+m}(2)^\infty$	$2\ell+1$ $2\ell+1+2m$
$n_{FOP} = 2m + 1$				
21− 21+	$(21)^\ell 0$	$(21)^m(2)^\infty$ $(12)^m(1)^\infty$	$(21)^{\ell+m}(2)^\infty$ $(21)^\ell 1 - (21)^m(1)^\infty$	$2\ell+2m+1$ 2ℓ
22− 22+	$(21)^\ell 2\,0$	$(21)^m(2)^\infty$ $(12)^m(1)^\infty$	$(21)^\ell 2 - (21)^m(2)^\infty$ $(21)^{\ell+m+1}(1)^\infty$	$2\ell+1$ $2\ell+2m+2$

(b)$n_{FOP} \neq n^*_{FOP}$

Label	Triple Collision	$\theta = 180\mp°$	Concatenation	Region c
$n_{FOP} = 2m$				
21− 21+	$(21)^\ell 0$	$(21)^m(2)^\infty$ $(12)^{m+1}(1)^\infty$	$(21)^{\ell+m}(2)^\infty$ $(21)^\ell 1 - (21)^{m+1}(1)^\infty$	$2\ell+2m+1$ 2ℓ
22− 22+	$(21)^\ell 2\,0$	$(21)^m(2)^\infty$ $(12)^{m+1}(1)^\infty$	$(21)^\ell 2 - (21)^m(2)^\infty$ $(21)^{\ell+m+1}(1)^\infty$	$2\ell+1$ $2\ell+2m+3$

- The Poincaré section is composed of the Schubart region and sectors surrounding it. If mass ratio is near that of totally degenerate case, a sector is composed of a subregion of fast escaping regions (scallop) and an arch-shaped block of strata (arch-shaped CSB). The regions numbers of regions included in an arch are mutually congruent modulo the number of sectors. The terminal points of the arches are the points on the θ-axis and their number is the same as the number of sectors.

- The number of sectors increases as the central particle becomes light. This fact harmonise with the McGehee's result that the winding number of fictitious orbits on the triple collision manifold increases.

- The structure of the Poincaré section changes from a totally degenerate case to another totally degenerate case through the common way. If the central mass is decreased, the germ-shaped block, which bifurcate from the leftmost scallop, grows

toward the roof and 180° side and becomes the lowest layer of the leftmost arch-shaped block. Even if this germ includes multiple regions, only the region with least region number survives. Similarly, germs bifurcate from other arches to be the second and the upper layers of arches, including the new arch. This event make the modulus increase by one, which determines the regions included in an arch.

- As asymmetry of mass ration becomes high, the regions with even region number shrink. Moreover, if the number of foot-points is different in the both sides of the Poincaré section, these regions disappear. Excluding this case, there exist regions for all region numbers.

A.1   Procedure to obtain the number distribution of FOPs

As we have mentioned in Sect.4.2, the distribution of $(n_{\rm FOP}, n^*_{\rm FOP})$ can be obtained from the number of passage of $W_d^{s\pm}$ between $s = -1$ and $s = +1$, so we show the procedure to obtain the number of passage.

Procedure to obtain the passage of $W_d^{s\pm}$ between $s = -1$ and $s = 1$

1. Calculate equilibrium points

   The value of s_c is obtained by the numerical solution of the equation $V'(s_c) = 0$ and the relative error of the value is about 10^{-10} among mass parameters. If obtained equilibrium points referring s_c are put into (f_r, f_w, f_s, f_v), the norm of this vector is 10^{-10}.

2. Calculate the coefficient matrix of the linearised equation of (22)–(25) around d

   The equations are linearised around d as $\frac{d}{d\tau}(\delta w, \delta s, \delta v)^T = [a_{i,j}](\delta w, \delta s, \delta v)^T$, where $a_{i,j} = \partial f_i / \partial j$ and $i, j \in \{w, s, v\}$. Since the constraint that variations δw, δs, and δv are taken on the energy manifold reduces into $\delta v = 0$, only 2×2 part of a_{ij} is effective. The value of a_{ij} is calculated numerically with the displacement $\Delta \ell$ of w or s. The calculation is iterated with replacing $\Delta \ell$ by $\Delta \ell / 2$. The eigenvectors of $a_{i,j}$ are calculated via their eigenvalues directly. For one of the eigenvectors, the angle between the value of n-th and $(n-1)$-th step gives error of a_{ij}. This angle decreases with decreasing $\Delta \ell$, tends to increase because of error of equilibrium points and we stop the iteration for $a_{i,j}$ at this moment. At the end of the iteration, $\Delta \ell = 10^{-7}$ and $\delta\phi = 10^{-6}$.

3. Integrate from the point slightly apart from d along the stable eigenvector and count the passage between $s = -1$ to $s = +1$.

4. Iterate the above steps $1 - 3$, and determine mass parameter where the number of travels changes

   First, we obtain the distribution of the number of passage between $s = -1$ and $s = 1$ on the mass-triangle with the grid size of $\Delta a = \Delta b = 0.1$. Second, scanning all vertical lines $b = 0.1\Delta$, we find ranges of a including the border of the number and improve the ranges.

Part II

Periodic Points and the Structure of the Poincaré Section

1 Introduction

We start from the summary of the the structure of this Poincaré section according to the research of Mikkola and Hietarinta. There is a periodic orbit of period one in our system. This is the so-called Schubart orbit. This orbit intersects the Poincaré section with $0 \le \theta < \pi$ at only one point, that is, this is a fixed point of the Poincaré map. This point is inside a polygonal region (the Schubart region), where general orbits are stable in the sense that these never escape to infinity, and have similar behavior as the Schubart orbit does. Each side of the Schubart region faces an arch-shaped block (arch-shaped CSB) where the orbits are chaotic (Mikkola & Hietarinta, 1989; hereafter MH1989).

We have seen in Part I that near the totally degenerate case, each CSB is stratified only by arch-shaped regions, whereas in the intermediate mass ratio, germs (germ-shaped blocks) intrude between the Schubart region and the arch-shaped blocks. If we decrease the central mass, we can see the process that germs bifurcating from the leftmost scallop grow to be the main part of the new arch-shaped block at the next totally degenerate case. This process is repeated when the system passes between two consecutive totally degenerate cases, and accordingly the number of sectors containing arch-shaped blocks increases as the central mass is decreased.

We can expect the influence of the distribution of the periodic points bifurcated from the fixed point on the structure of the Poincaré section, with taking the following results of preceding researches into account. Generally, in twisted maps on the two dimensional surface, if the parameters specifying the system, such as mass ratio, is varied, periodic points bifurcate and go outward radially from the central fixd point (see, e.g., Tanikawa & Yamaguchi 1989). By taking the Poincaré map, we can confirm the existence of stable periodic points observing the islands appearing around the fixed point. The Poincaré map of Hietarinta & Mikkola (1993, hereafter HM1993) suggests that the periodic points which have the same number of islands as the number of the sides of the Schubart region seem to have a dominant role. Moreover, for the equal mass case, the periodic points are actually detected by MH1989. In this case, the Schubart region has quadrangular shape and two sets of unstable periodic points with period 2 are located at the vertices. Tanikawa & Mikkola (2000b) found curves running from the four unstable points via symbol sequences as sets of points whose orbits repeat the alternate collision. The points on the curves are distinguished from the Schubart region, because these points are mapped into more distant points from the fixed point. The curves seem to be the separatrices of the four unstable periodic points. The study for a similar dynamical system, the collinear Coulomb three-body problem with electron-ion-electron configuration, carried out by Sano(2003) is helpful to understand our system. In his system, there exists the Schubart region and on its vertices are unstable periodic points. He confirmed the existence of the separatrix numerically following the mapped points starting near the vertices.

In Part II, we will systematically detect the periodic points, follow their motion with varying mass ratio, and see the relation to the structure observed in Part I. We explain

the growing process of the germs associated with the motion of the periodic points. The result of HM1993 suggests that certain series of periodic points regulate the shape of the Poincaré section. As for this suggestion, we confirm that such periodic points have a rotation number with a special form and determine the border of the Poincaré section for one case of the series. The chaotic scattering blocks are filled with triple collision curves (TM2000a), periodic points can not traverse these curves. We observe that the periodic points intruding with detouring these curves affect on the structure inside the chaotic scattering blocks.

Section 2 is devoted to the formulation of the problem and the preparation of tools. The equations of motion and the definition of the Poincaré section (θ, R) and the symbol sequence are common to Part I. In addition, we introduce the rotation number α which is a index describing the behaviour of the periodic points (PPs). The detection of the PPs using the rotation number is shown. In Sect.3, we first summarise property of the series of the PPs bifurcated from the fixed point(FXP) with changing the mass of central particle, then look at the process in detail that a set of the PPs with certain α, as a sample case, move outward from the FXP on the Poincaré section with changing the central mass. In order to look at the influence on the structure of Poincaré, we show the divided Poincaré section or triple collision curves. We also construct a scenario about the PPs and the change of the Poincaré section based on this observation. Section 4 summarises the result of Part II.

2 Method

We have studied the structure on the Poincaré section in Part I. We return to the Poincaré map technique used by HM1993 in Part II. This Poincaré map has the fixed point and the periodic points bifurcated from it. The purpose of this part is to follow how these periodic points relate to the structure observed in Part I. In this section, we define the Poincaré section and introduce a quantity *rotation number* in a fixed-point-centric coordinates introduced here. The motion on the Poincaré section around the fixed point is the fixed-point-centric rotation. The rotation number is the averaged rotation angle under the Poincaré map.

2.1 The definition of the Poincaré map and the motion around the fixed point

We defined the Poincaré map on the Poincaré section (θ, R). See Sect.2.1 about the definition of the Poincaré section, and Sect.3.1 about the structures seen on it.

We divide the Poincaré section into two sides, and denote the part with $0° \leq \theta < 180°$ by II and the part with $180° \leq \theta < 360°$ by II*. An orbit starting from the Poincaré section repeats the intersection with II and II* alternately. When an orbit intersects with

Π (resp. Π^*) at (R, θ) and Π (resp. Π^*) again at (R'', θ''), we define a map T from (θ, R) to (θ'', R'').

$$T : (\theta, R) \to (R'', \theta''), \text{ where } (\theta, R), (\theta'', R'') \in \Pi \text{ or } (\theta, R), (\theta'', R'') \in \Pi^* \quad (35)$$

The map T has a fixed point (θ_0, R_0), which satisfy $(\theta_0, R_0) = T(\theta_0, R_0)$. The fixed point (FXP) is an orbital point of the periodic orbit, the so-called Schubart orbit (Schubart, 1956), whose symbol sequence is $(21)^\infty$. If this orbit is stable, the motion around the FXP is the FXP-centric rotation. Let us confirm the rotation by taking the Poincaré map. Figure 16(a) results from mapping the points many times on the line parallel to the θ-axis and starting from the FXP. The rotational motion is reflected on the ellipse-like curves (the so-called KAM curves). Moreover, we find that the rotation angle depends on the distance from the FXP, because the line parallel is mapped to a sprial as shown in Fig.16(b). As one can understand from an ellipse-like curve drawn under the numbers of mapping of a point, most of points do not return to their original points. However, there are few points which return to their original points under the n iterations of the mapping. These points are called the *periodic points* or n-periodic points and n the period. If periodic points (PPs) are stable, the points rotate around the PPs to the some extent from the PPs. Therefore, n individual KAM curves appear there instead of the KAM curves centered on the FXP. These individual KAM curves are often called 'islands'. Six islands appear in Fig.16(a). Conversely, when we obtain these islands through the numerical calculation of the Poincaré map, we can find the periodic points on the centre of the islands by solving the equation $(\theta, R)^T = T^n(\theta, R)$ using Newton Raphson method with the initial points inside the islands.

In order to describe the rotation, we introduce a quantity *rotation number*. The rotation number is the averaged number of rotations over the infinite iteration of the mapping. We introduce coordinates $(\tilde{\theta}, \tilde{R})$ with origin at the FXP to measure the rotation angle

$$\tilde{\theta} = (\theta - \theta_0), \quad \tilde{R} = g(R - R_0)/R_{\max} \text{ with } g = 100, \quad (36)$$

and corresponding the polar coordinates (D, A)

$$D = \sqrt{\tilde{\theta}^2 + \tilde{R}^2}, \quad A = \arctan(\tilde{R}/\tilde{\theta})$$
$$\tilde{\theta} = D \cos A, \quad \tilde{R} = D \sin A. \quad (37)$$

Obviously, the distance in this coordinates, $\sqrt{(R - R')^2 + g^2(\theta - \theta')}$, depends on the coefficient g. We set $g = O(\theta) = 100$ to balance the contributions from both components. There is a freedom that the Azimuth A is measured clockwise or anticlockwise, since the variaton of A is discrete. In order to measure the accumulated difference of the azimuth, we always measure anticlockwise (positive angle). Therefore, the azimuth difference ΔA is

$$\Delta A(A, A') = \begin{cases} A' - A & (\text{if } A' - A \geqq 0) \\ A' - A + 2\pi & (\text{else}) \end{cases}, \quad (38)$$

when (D, A) is mapped to (D', A').

58

(a) many iterations, $(a, b) = (-0.25, 0)$

(b) one iteration, $(a, b) = (-0.22, 0)$

$\widetilde{R}$

$\widetilde{\theta}$
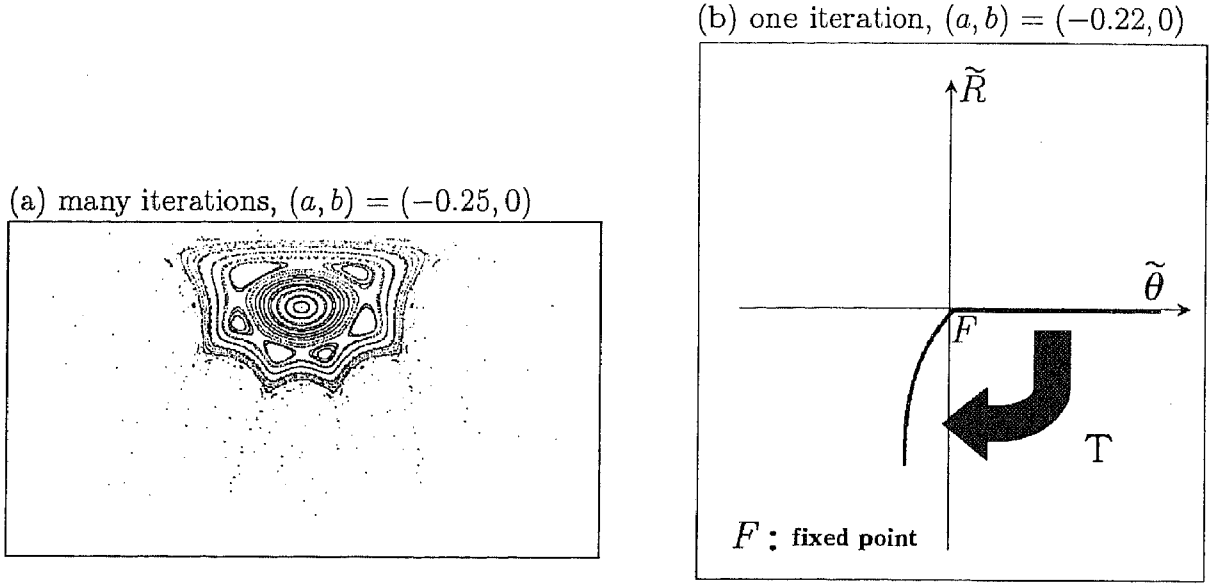
F

T

F : fixed point

Figure 16: The mapping of a line under the Poincaré map

2.2 Exact and Effective Rotation Number

Let $(D^{(i)}, A^{(i)})$ denote the mapped point of (D, A) under the i iteration of the mapping. The averaged number of rotations $\alpha(D, A; n)$ over the n iterations is

$$\alpha(D, A; n) = \frac{1}{2\pi n} \sum_{i=1}^{n} \Delta A(A^{(i-1)}, A^{(i)}). \tag{39}$$

The rotation number $\alpha_\infty(D, A)$ is defined by

$$\alpha_\infty(D, A) = \lim_{n \to \infty} \alpha(D, A; n). \tag{40}$$

We can only calculate $\alpha(D, A; n)$ for some n instead of exact rotation number though the numerical caluculation. We first iterate the mapping N times, and then take i that minimise $\delta A(A^i, A)$, for $1 \leq i \leq N$ as n. We write $\alpha(D, A; n)$ for this n $\alpha(D, A)$ and regard as the rotation number in this book. If the point (D, A) is a p-perodic points, $\alpha_\infty(D, A) = \alpha(D, A; p) = q/p$ with integers p, q. Moreover, since p is selected as n which determines $\alpha(D, A)$, $\alpha(D, A) = \alpha(D, A; p)$. Thus, our effective rotation number $\alpha(D, A)$ gives exact rotation number for the periodic points. Note that $\alpha = q/p$ corresponds to the periodic p but also kp, where integer $k \geq 2$. The rotation number of the kp-periodic points is q/p, which rotate q-times around the fixed point under the kp iterations. In this book, if necessary, we write the rotation numbers p/q and $2kp/2kq$ to discriminate the periods.

The Poincaré map $(\tilde{\theta}', \tilde{R}') = T(\tilde{\theta}, \tilde{R})$ is approximated by the linear map

$$\left(\begin{array}{c} \tilde{\theta}' \\ \tilde{R}' \end{array} \right) = G \left(\begin{array}{c} \tilde{\theta} \\ \tilde{R} \end{array} \right), \text{ where } [G]_{ij} = \frac{\partial T_i}{\partial j}, \ i, j \in \{\theta, R\}, \text{ and } T(\tilde{\theta}, \tilde{R}) = (T_{\tilde{\theta}}, T_{\tilde{R}}). \quad (41)$$

in the neighbourhood of the fixed point. The rotation number is calculate there via G. The matrix G is diagonalised with its eigenvalues λ_1 and λ_2 and eigenvectors $\vec{u}_1$ and $\vec{u}_2$:

$$G = V^{-1}BV, \text{ where } B = \left(\begin{array}{cc} \lambda_1 & 0 \\ 0 & \lambda_2 \end{array} \right) \text{ and } V = [\vec{u}_1 \ \vec{u}_2]^T. \quad (42)$$

The area is magnified anywhere by $|\det(G)|^n$ under the n iterations of mapping by G. Hence, if $\det(G)$ were not 1, the area increases or decreases monotonically. It is inconsistent with the volume preserving property of the Hamiltonian system. Therefore, $\det(G) = \lambda_1 \lambda_2 = 1$. The stability and the rotation number in the neighbourhood of the fixed point is considered in the coordinates (ξ, η) with $(\xi \ \eta)^T = V(\tilde{\theta} \ \tilde{R})^T$. When $\lambda_1 = \exp(\phi\sqrt{-1})$ and $\lambda_2 = \exp(-\phi\sqrt{-1})$, then $(\xi^{(n)} \ \eta^{(n)})^T = B^n(\xi^{(0)} \ \eta^{(0)}) = (\exp(n\phi\sqrt{-1}) \ \exp(-n\phi\sqrt{-1}))^T$. It shows the rotational motion and that the fixed point is stable for small displacement. When $\lambda_1 = r$ and $\lambda_2 = 1/r$ with $r > 1$, then $(\xi^{(n)} \ \eta^{(n)})^T = B^n(\xi^{(0)} \ \eta^{(0)})^T = (r^n \ 1/r^n)^T$. It shows the hyperbolic motion and that the fixed point is unstable. The dependence of this linear stability on the mass parameters is studied by MH1991. The symmetric case, considered here, is linear stable for all values of a. In most of linear stable cases, there is a stable region (the Schubart region) around the FXP. However, HM1993 found that the Schubart region vanishes in $a \fallingdotseq 0.4$ line on the mass-triangle in spite of the linear stability. We will consider this case later. The argument ϕ in stable case is the rotation angle (in coordinates (ξ, η)). Therefore, $\lim_{D \to 0} \alpha_\infty(D) = \phi/2\pi$.

2.3   The periodic points and their accompanied structure

The rotational motion under the mapping T has the rotation angle depending on the radius $\tilde{R}$. This motion is analogous to that under the (perturbed) twist map T_{tw} (Lichtenberg and Liberman, 1992):

$$T_{tw} : \left\{ \begin{array}{l} J_{n+1} = J_n + \epsilon f(J_{n+1}, \phi_n) \\ \phi_{n+1} = \phi_{n+1} + 2\pi\alpha(J_{n+1}) + \epsilon g(J_{n+1}, \phi_n), \end{array} \right. \quad (43)$$

where perturbation parameter ϵ, the rotation number $\alpha(J_{n+1})$ in unperturbed case $\epsilon = 0$ (regard (J, θ) as the radius and the angle), periodic functions f and g for ϕ. When $\epsilon = 0$, there is the circle whose points are p-periodic points with the rotation number $\alpha(J) = q/p$. According to the Poincaré -Birkoff theorem, this circle is broken into $2kp$ periodic points with integer $k \geq 2$, when $\epsilon \neq 0$. The following is the outline of the proof. The closed curve C_1 exist also in $\epsilon \neq 0$ case, where the angle ϕ is unchanged after p iteration of mapping but the radius changed. Let C_2 denote the closed curve mapped from C_1 under the p iteration.
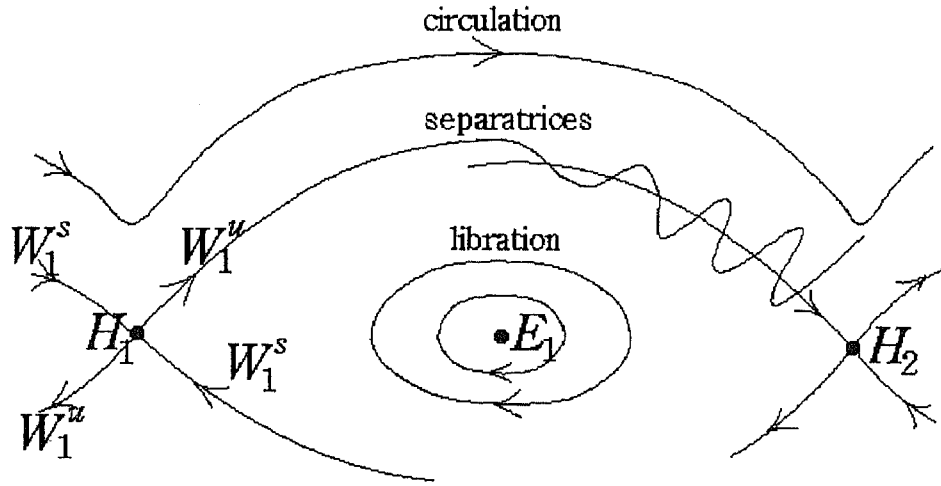
Figure 17: the periodic points and their accompanied structures

Since C_1 and C_2 have to enclose an equal area due to the area-preserving property, C_1 must intersect with C_2 an even number of times. The intersecting points are p-periodic points. The periodic points are divided into two types according to the motion of their neighbourhood. One motion is rotationl motion. The periodic points are called *elliptic* for this type. Due to this rotation, the points near the periodic points take only the values of ϕ around that of the periodic points. This motion is called *libration*. The other motion is hyperbolic motion and corresponding periodic points are called *hyperbolic*. The number of elliptic and hyperbolic periodic points is the same and aligined alternately. When the initial point is changed from the elliptic point to hyperbolic point, its motion under the iterations changes from the libration to the circulation. The hyperbolic motion in the neighbourhood of unstable points are described by the matrix linearising the composition mapping of p iterations. The motions for the infinitesimal displacement in the direction of the eigenvectors of the matrix are marginal of elliptic and hyperboilc motion. Their trajectories are called *separatories*. The schematic illustration about the elliptic and hyperbolic points and accompanied libration and separatrices are shown in Fig.??.

The elliptic point E_1 exist between two hyperbolic points H_1 and H_2 in the figure. The separatrices of H_1 are four curves marked with W_1^u and W_1^s, which are called unstable and stable manifolds of H_1. The separatrices are mapped into themselves and the points on W_1^s and W_1^u are mapped to H_1 under the infinite number of mapping and inverse
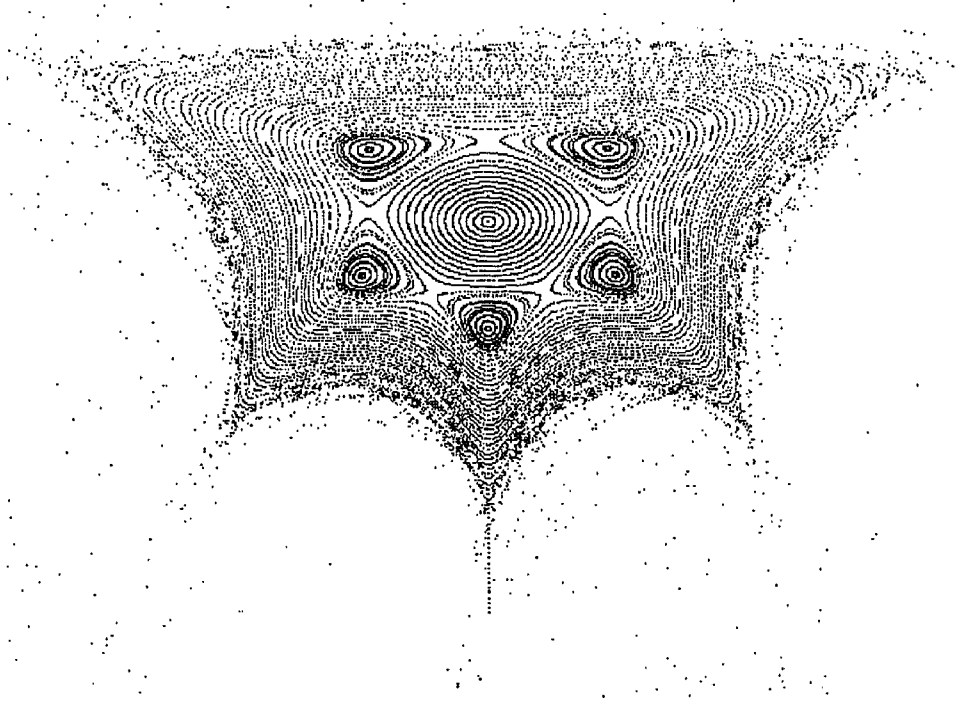
Figure 18: the periodic points and their accompanied structures in the rectilinear three-body system, $(a,b) = (-0.15,0)$, $\alpha_\infty = 3/5$.

mapping, respectively:

$$T_{tw}(W_1^s) = T_{tw}(W_1^s) \text{ and } T_{tw}(W_1^u) = T_{tw}(W_1^u) \tag{44}$$

$$\lim_{n\to+\infty} T_{tw}^{np}(\vec{x}_s) = H_1 \quad \text{for } \vec{x}_s \in W_1^s \tag{45}$$

$$\lim_{n\to-\infty} T_{tw}^{np}(\vec{x}_u) = H_1 \quad \text{for } \vec{x}_u \in W_1^u.$$

If the composition map T_{tw}^p of p iterations are linearised at the periodic points by the matrix G_{tw}, the eigenvalues of G_{tw} are $\lambda_1 = r$ and $\lambda_2 = 1/r$ ($r¿1$) for the hypernbolic points H_i and $\lambda_1 = \exp(-\phi\sqrt{-1})$ and $\lambda_2 = \exp(\phi\sqrt{-1})$ for the elliptic points E_i, where due to the area preserving property, $\lambda_1\lambda_2 = 1$. At the hyperbolic points, the eigenvector for λ_1 elongates, while the eigenvector for λ_2 shrinks, under the mapping by G_{tw}. We have mentioned the accompanied structure of the periodic points generally seen in twist maps. We show in Fig.?? that similar structure appears under the mapping by T.

The periodic points move radially in twist map, when the parameters of system is varied. For example, in the standard map

$$\begin{cases} J_{n+1} = J_n + K\sin\phi_n \\ \phi_{n+1} = \phi_n + J_{n+1} \end{cases}, \tag{46}$$
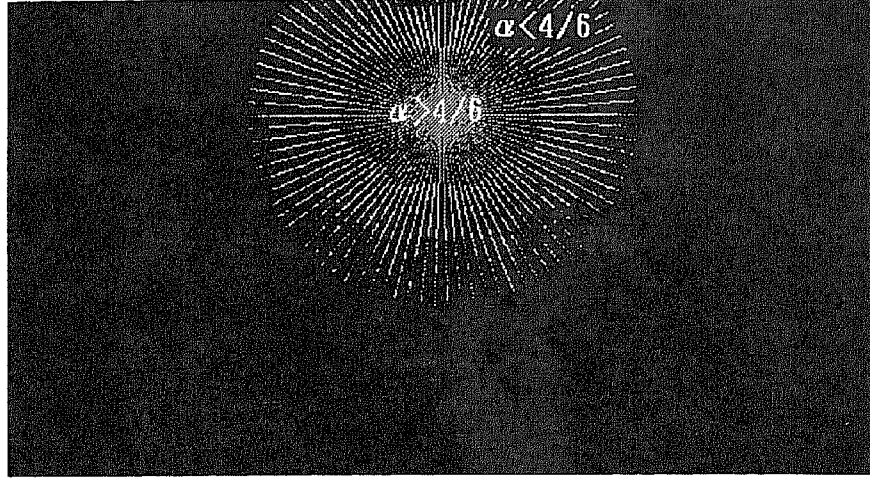
Figure 19: The azimuth unchanged curve as the candidate for the periodic points, $(a, b) = (-0.25, 0), \alpha_\infty = 4/6$

which is obtained from the setting $\epsilon f(J_{n+1}, \phi) = K \sin \phi$, $\alpha(J_{n+1}) = J_{n+1}$, and $g = 0$ in the twist map(43), K is the parameter of system. The behaviour of the periodic points when K is varied is studied by Chrikov(1979) and Tanikawa and Mikkola(1988). In our map T, the parameter is the mass parameter a. The periodic points may move inward and finally coincide with the fixed point, when these parameters are varied to some direction. If the rotation number of the periodic points is q/p, then $\lim_{D \to 0} \alpha_\infty(D, A)$ must q/p at the value of the parameter for the coincidence. Conversely, for arbitrary rational q/p, $\lim_{D \to 0} \alpha_\infty(D, A) = q/p$ shows any points are periodic points with period p under the linearised map of the original map. Therefore, the periodic points bifurcate from the fixed point, when $\lim_{D \to 0} \alpha_\infty(D, A)$ is rational.

2.4 How to detect the periodic points

We mention the detection of the periodic points. First, we have to calculate $\lim_{D \to 0} \alpha_\infty(D, A)$ as a function for a. For given $\alpha_\infty = q/p$, we can determine the massparameter a where corresponding periodic points appear. Second, we find the candidate at a mass parameter little distant from the exact bifurcation. There are two way to find candidate. One way is to take the Poincaré map such as Fig.16(a). The candidates for elliptic points can be taken at the centre of the libration and for hyperbolic points at the saddle between two librations. The other way is to obtain the $\alpha(D, A)$ distribution. The points whose $\alpha(D, A)$ is near q/p are taken as the candidate in the order of the nearness. These points exist on the curve where the azimuth is unchanged after the p iteration of the mapping (corresponding to the curve C_1 in Sect.2.3). We show this curve in Fig.19, where $(a, b) = (-0.25, 0)$ and $\alpha_\infty = 4/6$, as the boundary of regions with $\alpha(D, A) > 4/6$ and $\alpha(D, A) < 4/6$. Finally, we

make the candidate converge using the Newton-Raphson method. This method is used in MH1991 to find the fixed point $(\theta_0, R_0) = T(\theta_0, R_0)$. Replacing T with T^p, we can use this method for the p-periodic points. First, we show the general multi-dimensional Newton Raphson method. The problem is to slove $\vec{G}(\vec{X}) = \vec{0}$, where $\vec{X} \in \mathbf{R}^N$ and $\vec{G}: \mathbf{R}^N \to \mathbf{R}^N$. Let $(\vec{X}_0, \vec{X}_n)$ denote the initial value (candidate point) and approximated solution at the n-th step. Linearising $\vec{G}(\vec{X})$ around $\vec{X}_n$ and supposing that $\vec{X}_{n+1}$ is the solution of $\vec{G}(\vec{X}) = \vec{0}$ under the approximation, we get

$$\vec{G}(\vec{X}_{n+1}) \fallingdotseq \vec{G}(\vec{X}_n) + \left[\frac{\partial \vec{G}(\vec{X}_n)}{\partial \vec{X}_n} \right] (\vec{X}_{n+1} - \vec{X}_n) = 0. \tag{47}$$

It is reduced to the recurrence formula

$$\vec{X}_{n+1} = \vec{X}_n - \left[\frac{\partial \vec{G}(\vec{X}_n)}{\partial \vec{X}_n} \right]^{-1} \vec{G}(\vec{X}_n) = 0. \tag{48}$$

If we set $\vec{X} = (\theta, R)$ and $\vec{G}(\vec{X}) = T^p(\vec{X}) - \vec{X}$, we get the recurrence formula to calculate the periodic points

$$\vec{X}_{n+1} = \vec{X}_n - \left[\frac{\partial T(\vec{X}_n)}{\partial \vec{X}_n} - 1 \right]^{-1} (T^p(\vec{X}_n) - \vec{X}_n) = 0. \tag{49}$$

2.5   Symbol Sequences and Partition of the Poincaré Section

About the definition of the symbol sequence, see §2.3, Part I, and about the partition of the Poincaré section according to the symbol sequences see §3.2, Part I. As has been shown there, the Poincaré section is divided into a lot of regions including the Schubart region according to the symbol sequence with 64 columns. We then regard a connected region with $(21)^n$, $n \geq 32$ containing the FXP as the 'Schubart region'.

3   Results

3.1   Radial Movements of PPs

We examine which direction the PPs move when mass parameters are changed, by means of the rotation number distribution on the Poincaré section. In the present paper, we only consider the symmetric mass configuration. Therefore, we fix $b = 0$ and change a. We calculate numerical rotation number $\alpha(D, A)$, defined in (39), for certain selected values of a; we write $\alpha(D, A)$ as $\alpha(D, A, a)$ to show its dependence on a.

We first calculate the $\alpha(D, A)$ distribution on the Poincaré section. Using this data, we draw the equi-rotation-number curves for rational values. Then we find that these are

polygonal closed curves around the FXP. The PPs with these rotation numbers exist on the curves. Hence, we utilise the curves for selecting the candidates for the PPs. We then improve the position of the candidates via the Newton-Raphson method. We find that all PPs for a value of α go out from or come into the FXP radially. Therefore, we can assume it is independent to azimuth A that the equi-rotation-number curve goes out or comes in. We fix $A = 0$ and examine which direction this curve moves.

Suppose that a equi-rotation number for $\alpha(D, A, a)$ intersects with a line $A = 0$ at D when the mass parameter is a; then the intersecting point moves to $D + dD$ when the mass parameter is $a + da$. The relation da and dD is written as

$$d\alpha = \left(\frac{\partial \alpha}{\partial a}\right)da + \left(\frac{\partial \alpha}{\partial D}\right)dD = 0. \tag{50}$$

The sign of dD gives us the direction of motion of the curves and the PPs for a given sign of da. Particularly, the sign of dD at $D \to 0$ (the FXP) shows that the PPs are bifurcated or annihilated. We determine the signs of $(\partial \alpha/\partial a)$ and $(\partial \alpha/\partial D)$ at $D \to 0$ using dependence of $\lim_{D \to 0} \alpha(D, a)$, and dependence of $\alpha(D, a)$ on D for several values of a. These dependence are shown in Figs. 20 and 21.

The dependence of $\lim_{D \to 0} \alpha(D, a)$ is calculated from the linearisation matrix G around the FXP for the Poincaré map T. We are not successful in calculating G for $a > 0.75$, because we cannot not find the FXP. We consider the dependence on a continues after $a = 0.75$. Base on this consideration, we assume that

$$\left(\frac{\partial \alpha}{\partial a}\right)\bigg|_{D=0} < 0 \qquad \text{for all } a. \tag{51}$$

In addition, if $\lim_{D \to 0} \alpha(D, a)$ becomes 0 at $a = 1$, we can assume that the range of $\lim_{D \to 0} \alpha(D, a)$ in the domain $-1/2 < a < 1$ is

$$\inf \lim_{D \to 0} \alpha(D, a) = 0 \text{ and } \sup \lim_{D \to 0} \alpha(D, a) = 1 : \tag{52}$$

$\lim_{D \to 0} \alpha(D, a)$ moves all the range of the rotation number.

Referring to the dependence of $\alpha(D, a)$ on a for several values of a, we assume that

$$\begin{cases} \left(\dfrac{\partial \alpha}{\partial D}\right) > 0 & \text{(for } a > a_{1/3} \text{ and inside the Schubart region)}, \\[2ex] \left(\dfrac{\partial \alpha}{\partial D}\right) < 0 & \text{(for } a < a_{1/3} \text{ and inside the Schubart region)}, \end{cases} \tag{53}$$

where $\lim_{D \to 0} \alpha(D, a_{1/3}) = 1/3$. However, in order to reach this assumption, we have to add several interpretations to the original data shown in Fig.17. In Fig.17(b), The graph of $\alpha(D, a)$ is jaggy for $a = 0.35$, 0.38, and 0.45 in $D \gtrsim 3$. The jaggy part of the curve results

from meaningless α values calculated in the chaotic scattering region. In the chaotic scattering region, the variation of azimuth A is sensitive to the initial point. Therefore, if the point (D, A) goes out of the Schubart region, the graph of $\alpha(D, a)$ changes from a smooth curve to a jaggy curve. Since the Schubart region is large in the $a < 0$ case, the jaggy curves do not appear in Fig.21(a). We can only understand $(\partial\alpha/\partial D) < 0$ for $a \lesssim 0.35$ (Fig.17(a) and upper two curves in (b)) and $(\partial\alpha/\partial D) > 0$ for $a \gtrsim 0.45$ (Fig.17(b) the lower two curves) from Fig.17 itself. Since our rotation number is not so accurate, the change of $\alpha(D, a)$ cannot be resolved when $(\partial\alpha/\partial D) \doteqdot 0$. Instead of testing the sign of $(\partial\alpha/\partial D)$, we detect the PPs with $\alpha = 1/3$ at $a = 0.35$ and at $a = 0.45$ individually, and followed the their motions during $0.35 \le a \le 0.45$. In Fig.22, we show the $D - a$ graph for one of the PPs. Increasing a from $a = 0.35$ to $a = 0.45$, the PP with α (labelled with '$\alpha = 1/3L$') approaches and reaches the FXP at $a \doteqdot 0.406$. Decreasing a from $a = 0.45$ to $a = 0.35$, the PP with $\alpha = 1/3$ (labelled with '$\alpha = 1/3U$') also approaches and reaches the FXP at $a \doteqdot 0.406$. Moreover, according to the data plotted in Fig.16 as the $\lim_{D\to 0} \alpha(D, a)$ graph, $\lim_{D\to 0} \alpha(D, a) = 1/3$ at $a = a_{1/3} \doteqdot 0.40$ (the value of $a_{1/3}$ is less accurate than crossing point of both lines '$\alpha = 1/3L$' and '$\alpha = 1/3U$'). From the above results, we assume that $dD < 0$ for $0.35 \le a \le 0.406$ and $dD > 0$ for $0.406 \le a \le 0.45$, if $da > 0$. This assumption is equivalent to that $(\partial\alpha/\partial D) < 0$ for $0.35 \le a \le 0.406$ and $(\partial\alpha/\partial D) > 0$ for $0.406 \le a \le 0.45$, if (51) is satisfied.

From the assumption (51) and (53) and the relation (50), the sign of da so that $dD > 0$ (PPs bifurcate) is

$$\begin{cases} da > 0 & \text{(for } a > a_{1/3}) \\ da < 0 & \text{(for } a < a_{1/3}) \end{cases} . \tag{54}$$

We prove the following proposition under the above assumption.

PROPOSITION 1 *Except for PPs which do not bifurcate from the PP and which bifurcate at the PP in asymmetric mass configuration, there are no PPs at $a = a_{1/3}$.*

[Assumption]

- (52) $\lim_{D\to 0} \alpha(D, a)$ takes the all range of rotation number

- (54) the sign of da for the bifurcation

[Proof] Suppose that there exist PPs with α_0 at $a = a_{1/3}$. We examine whether the PPs is bifurcated ones at $a \ne a_{1/3}$ and $b = 0$.

If $\alpha_0 < 1/3$,
   PPs with α bifurcate at only $a = a_0 > a_{1/3}$ and go outward if $da > 0$.
   Therefore, the PPs with α_0 cannot exist at $a = a_{1/3}$.

If $\alpha_0 > 1/3$,

PPs with α bifurcate at only $a = a_0 < a_{1/3}$ and go outward if $da < 0$. Therefore, the PPs with α_0 cannot exist at $a = a_{1/3}$.

If $\alpha_0 = 1/3$,

PPs with α bifurcate at only $a = a_{1/3}$ and coincide with the FXP itself at $a = a_{1/3}$. Therefore, the PPs with α_0 cannot exist at $a = a_{1/3}$.

Q.E.D.

If the Schubart region has the finite extent on the Poincaré section and $(\partial\alpha/\partial D)$ is 0 in the not all region, there exist PPs in the region. Therefore, the Schubart region is the FXP itself at $a = a_{1/3}$. HM1993 found that the Schubart region vanishes at $a = 0.4$ using Poincaré map. We confirm that the Schubart region takes triangular shape at $a = 0.35$ and reversed triangular shape at $a = 0.45$, and the PPs with $\alpha = 1/3$ stay at its vertices. From the motion of one of PPs shown in Fig.22, as a is increased from $a < a_{1/3}$ to $a > a_{1/3}$, the Schubart region may shrink with triangular shape, vanish, and expand with reversed triangular shape.
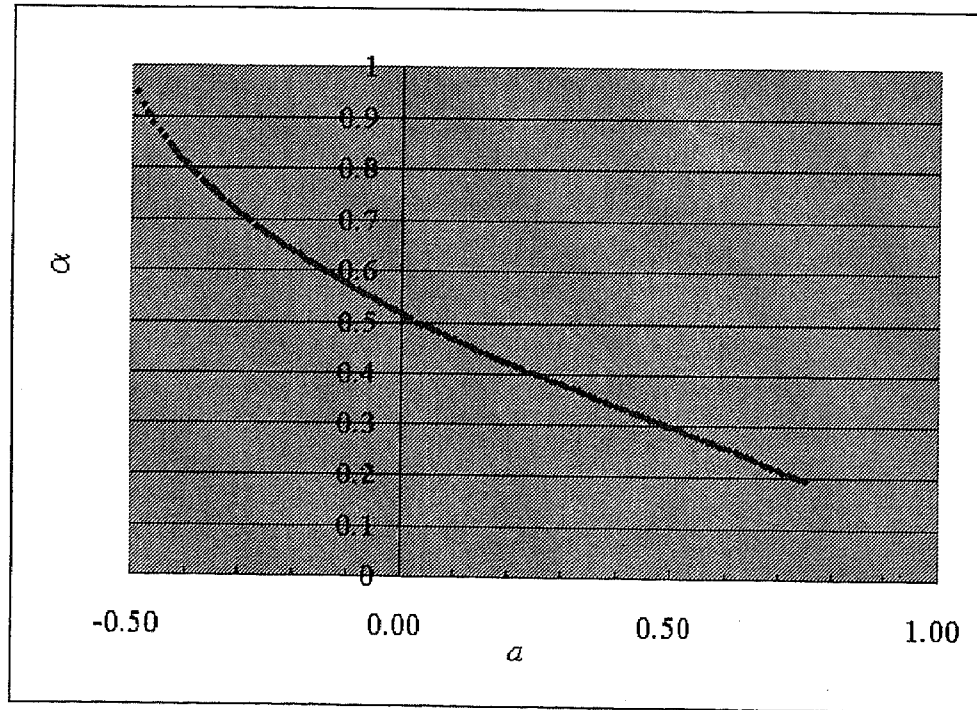
Figure 20: Dependence of $\alpha(D = 0, a)$ on a

(a) $a < 0$ case
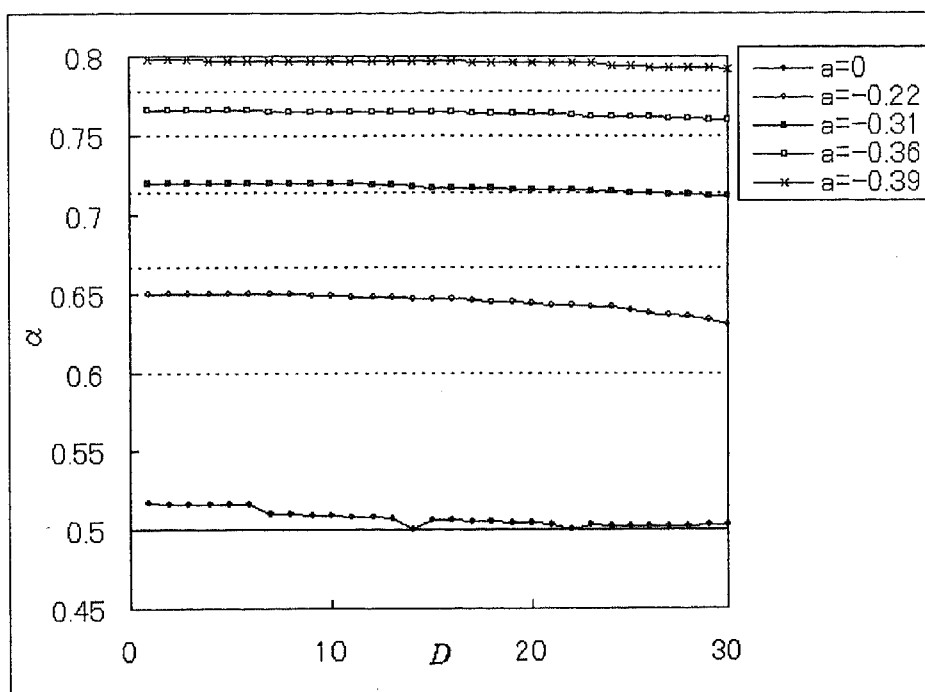
(b) $a > 0$ case, around $a \fallingdotseq 0.4$
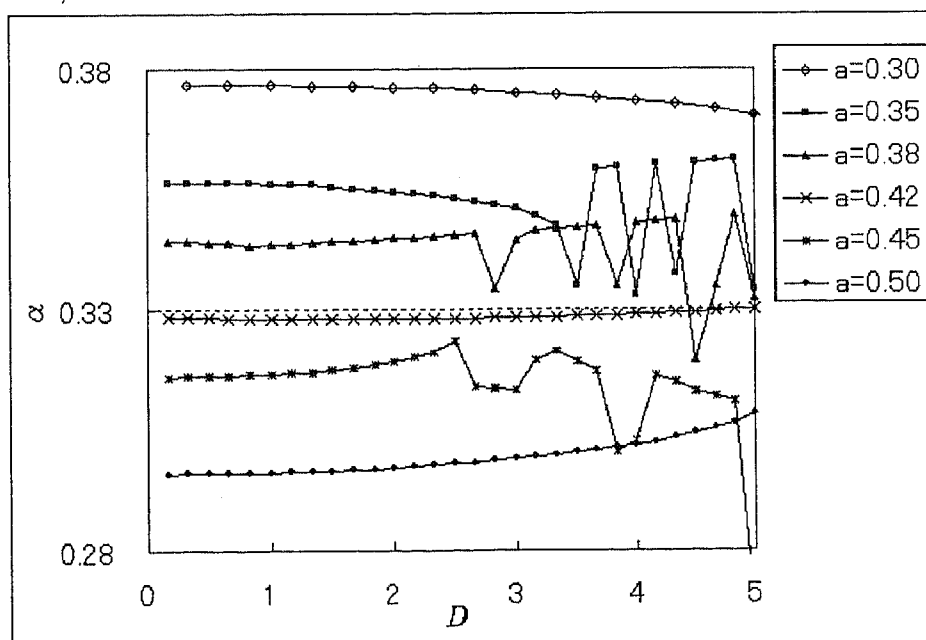
Figure 21: Dependence of $\alpha(D, a)$ on D

68
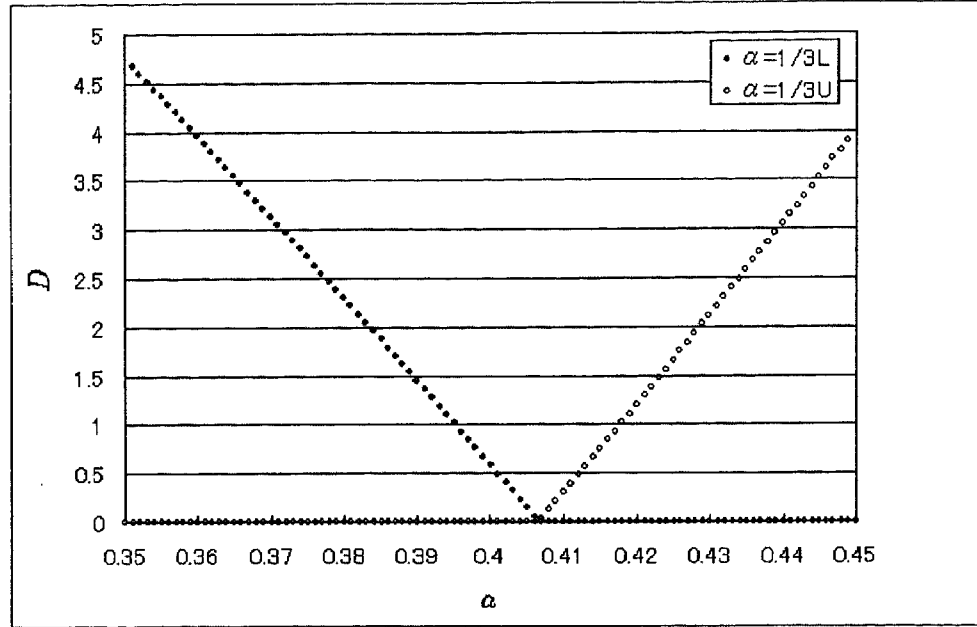
Figure 22: The radial motion of the PPs with $\alpha = 1/3$

3.2 The rotation numbers of dominant PPs

The PPs with special rotation numbers are important for the structure of the Poincaré section. Such rotation numbers have a form $\alpha = (n-2)/n$ with integer $n > 2$.

The periodic orbits with $\alpha = (n-2)/n$ have a rule about the number of the orbits and period. For odd n, there is a pair of stable and unstable orbits with period n. The case $\alpha = 1/3$ is an exception: there is only an unstable orbit. For even n, there are two pairs of stable and unstable orbits with period $n/2$. Therefore, in this case, if the information for period is required, we have to write $\alpha = (k-1)/k$, where $k = n/2$. We show the location of the PPs on the Poincaré section with (a) $\alpha = 3/5$ and (b) $\alpha = 4/6$ in Fig.23. In this figure, we connect the PPs which belong to the same orbit. We examine the above property for the number of periodic orbits up to $n = 19$ ($\alpha = 17/19$), which is shown in Fig.?? together with Poincaré map. We marked up the PPs with circle for the first stable orbit, with multiply-symbol for the first unstable orbit, with filled-circle for the second stable orbit, and with plus-symbol for the second unstable orbit. The background plots result from the mapping of the points on the line through the fixed point: $(D, A)|A = 0, D = D_{min} + k\Delta D, \Delta D = 1°, k = 1, \cdots, k_{max}$, where D_{min} and k_{max} are selected appropriately according to the size of the Schubart region. We can confirm that stable orbital points stay at the centre of the circulation, while the unstable ones at the saddle between two circulations. That there are two orbits for stable and unstable

(a) $\alpha = 3/5$
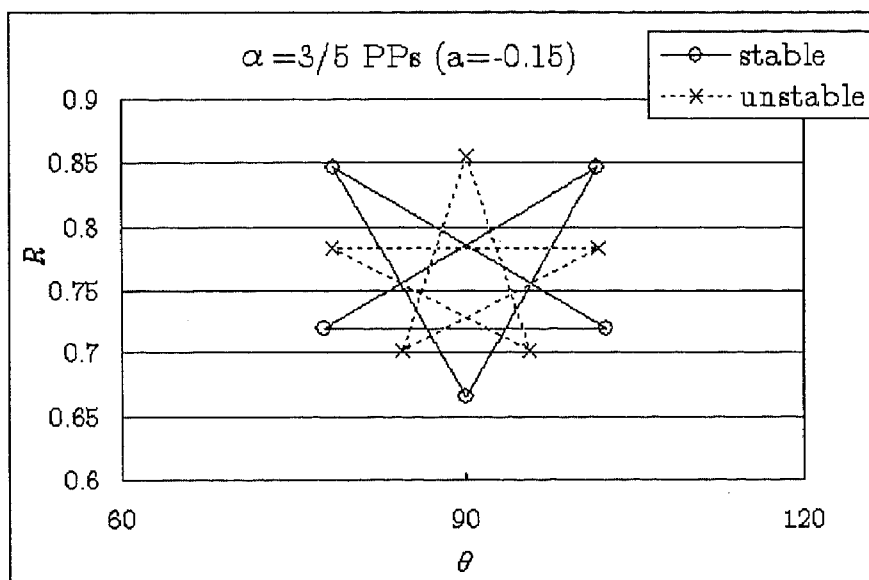
(b) $\alpha = 4/6$
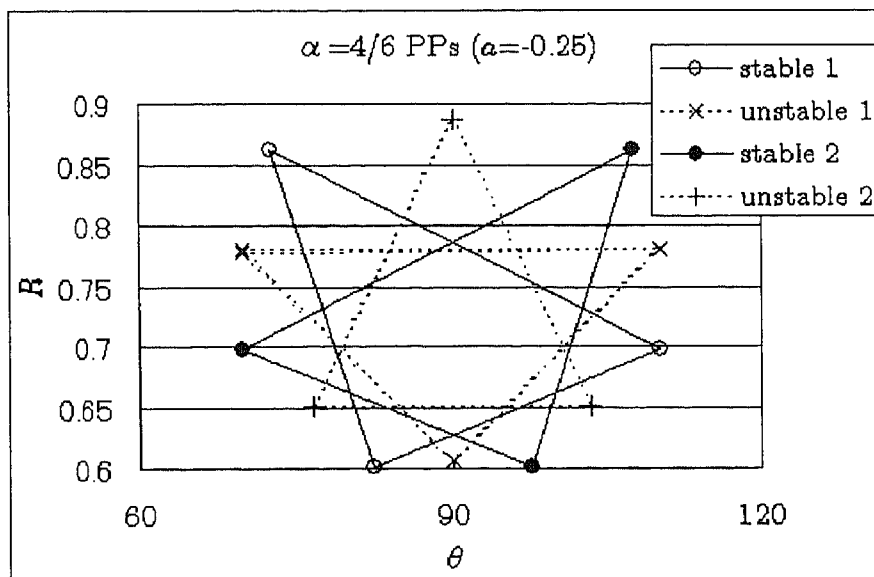
Figure 23: Sample of the periodic points

70

respectively in even n is found through the appearance of whole four marks. This fact appears in the lack of the circulation around second stable orbits. The above initial points include the points near a stable point. These points take the circulation around the all stable points of the orbit to which this stable point belongs. For odd n, these stable points are all stable points for $\alpha = (n-2)/n$, while for even n only a half of all stable points $\alpha = (n-2)/n$.

(a) $\alpha = 13/15$, $(a, b) = (-0.452335, 0)$
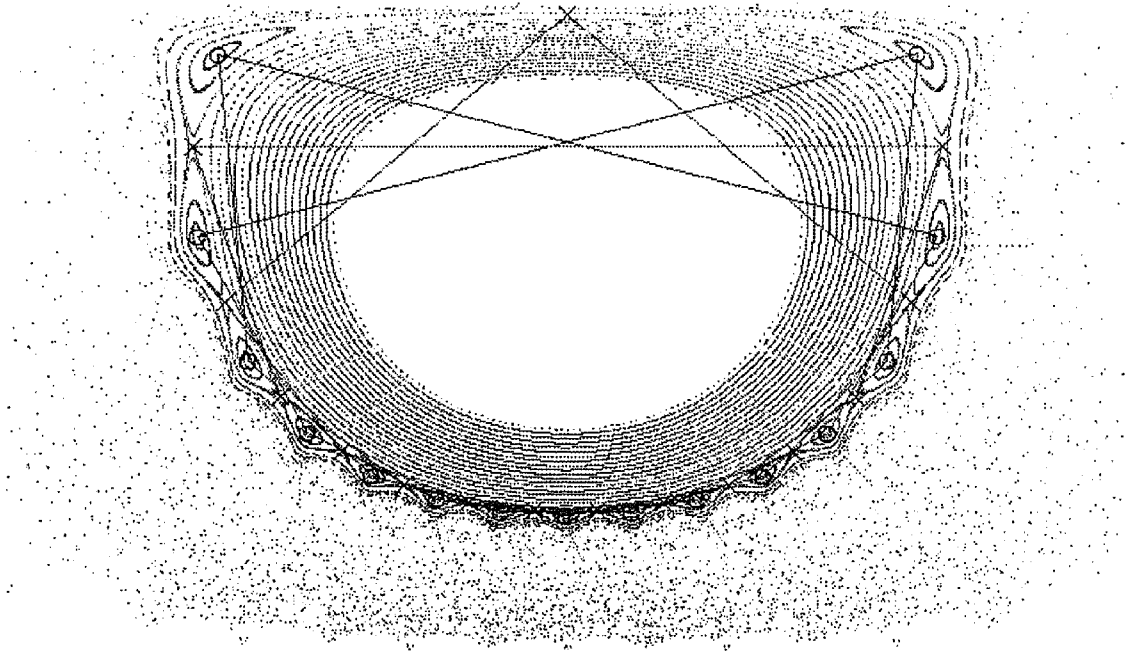
Figure 24: Periodic points with $\alpha = (n-2)/n$

The following is a list for the mass parameters a where $\lim_{D \to 0} \alpha(D, A)$ is rational and

(b) $\alpha = 14/16$, $(a,b) = (-0.457276, 0)$
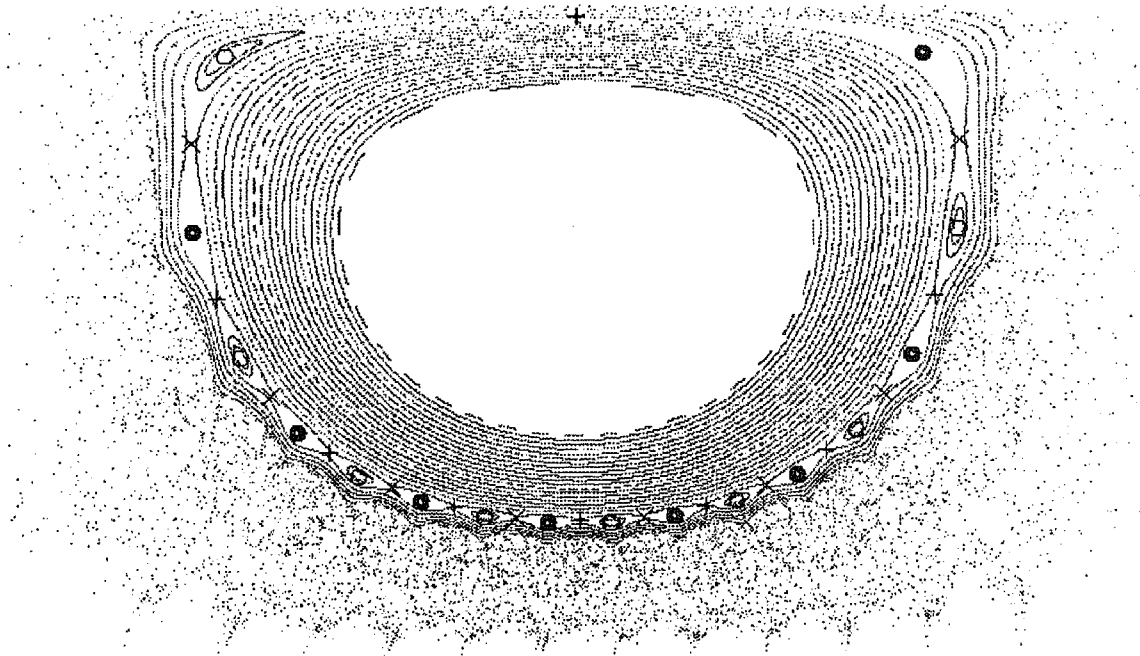
Figure 24: Periodic points with $\alpha = (n-2)/n$ (continue)

(c) $\alpha = 15/17$, $(a,b) = (-0.461844, 0)$
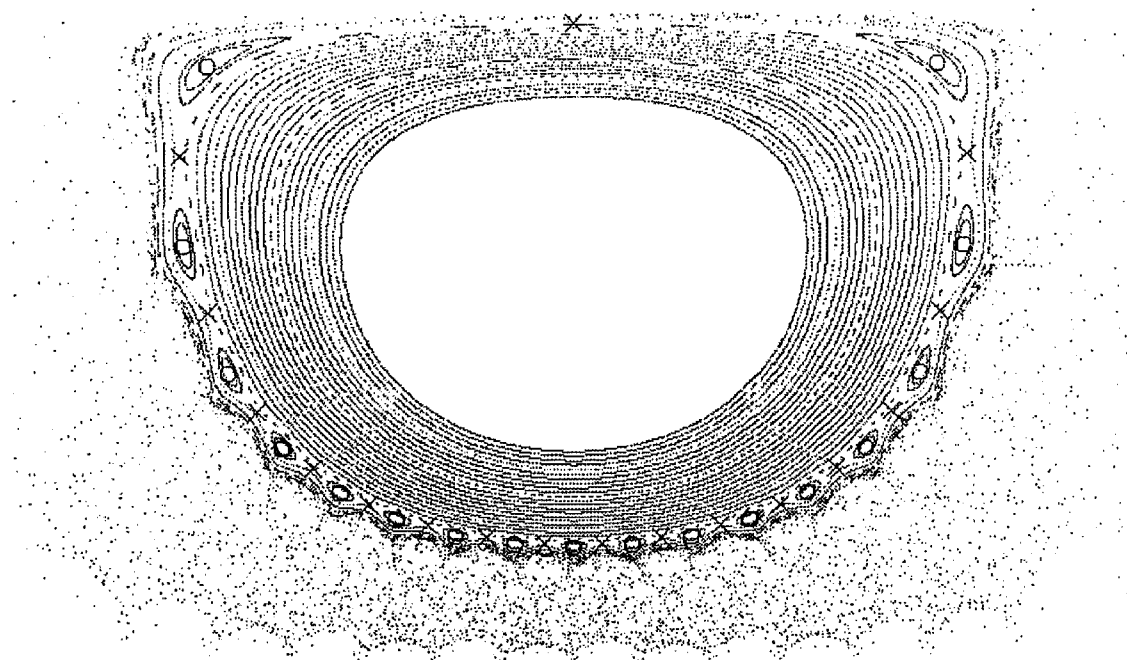
Figure 24: Periodic points with $\alpha = (n-2)/n$ (continue)

(d) $\alpha = 16/18$, $(a,b) = (-0.466010, 0)$
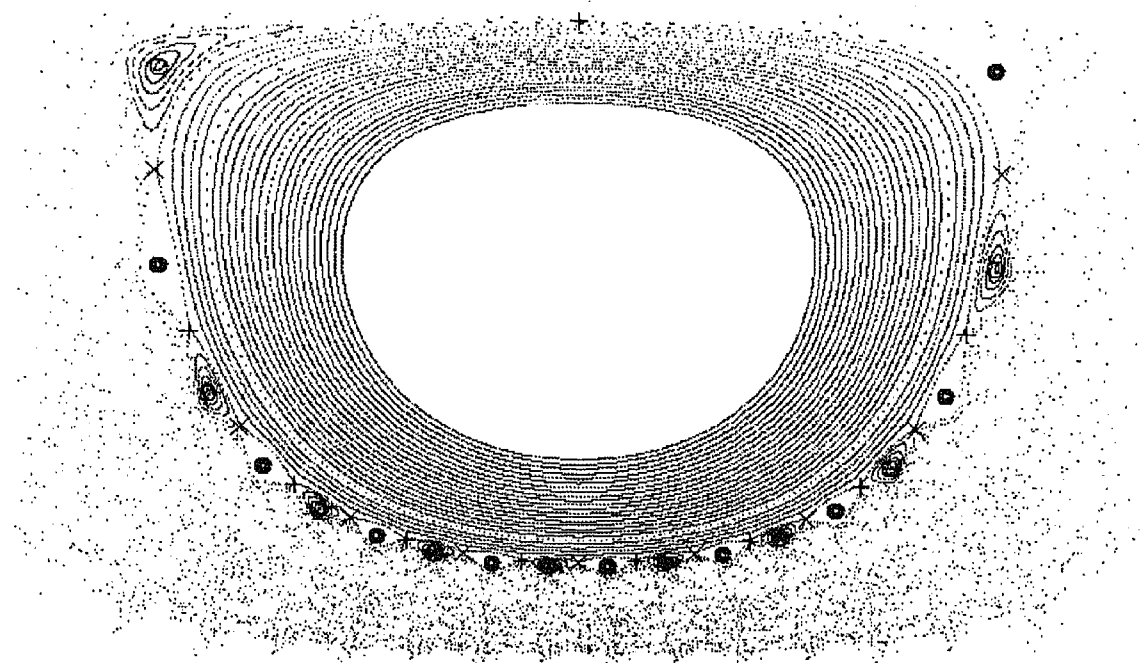
Figure 24: Periodic points with $\alpha = (n-2)/n$ (continue)

(e) $\alpha = 17/19$, $(a, b) = (-0.468687, 0)$
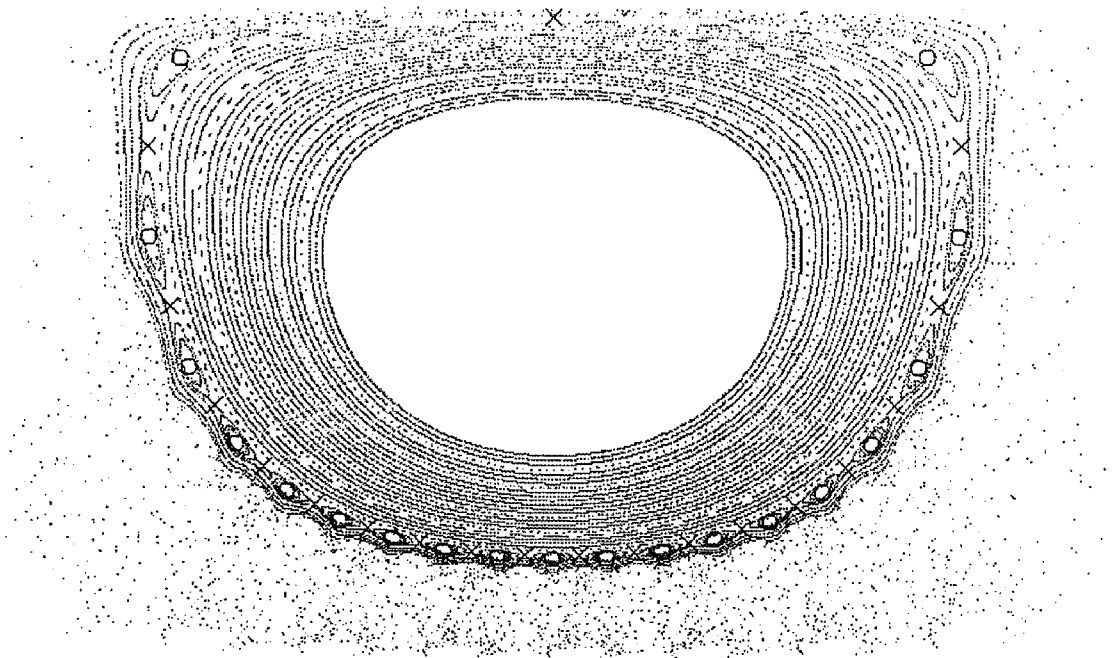
Figure 24: Periodic points with $\alpha = (n - 2)/n$ (continue)

corresponds to small period:

$$a \geq a_{1/3} : a_{1/3} \fallingdotseq 0.4, a_{1/4} \fallingdotseq 0.61, \cdots$$
$$a \leq a_{1/3} : a_{1/3} \fallingdotseq 0.4, a_{2/4} \fallingdotseq -0.019, a_{3/5} \fallingdotseq -0.15, a_{4/6} \fallingdotseq -0.25, a_{3/7} \fallingdotseq -0.31, \cdots.$$

The PPs appearing after the PPs with $\alpha = 1/3$ include the series of PPs with $\alpha = (n-2)/n$ in $a < a_{1/3}$ case, while in $a > a_{1/3}$ case do not. This difference is reflected on the change of the Poincaré section. In $a < a_{1/3}$ case, the Poincaré section is governed by the PPs with a rotation number written in the form $(n-2)/n$. The unstable PPs stay at the vertices of the Schubart region with polygonal shape. The germs grow and follow the stable PPs. We checked these relation between the PPs with $\alpha = (n-2)/n$ and the Poincaré section, for $n = 5$, 6, 7, and 8. We treat the $n = 5$ ($\alpha = 3/5$) case in the next section. In $a > a_{1/3}$ case, the PPs with $\alpha = 1/3$ stay at the vertices of the triangular Schubart region similarly to the $a < a_{1/3}$ case. However, many PPs with $\alpha = 1/4$, 1/5, 1/6, $\cdots$, appear on the Poincaré section; the influence of the PPs for each α is small, but these PPs as a whole make the behaviour of germs complex. Thus, we cannot give a simple explanation to the relation between the PPs and the structure of the Poincaré section in $a > a_{1/3}$ case.

3.3   Influence of the PPs on the Structure of the Poincaré Section

We study the influence of the PPs on the structure of the Poincaré section for $\alpha = 3/5$ case. We show the location of the PPs on the Poincaré section from $a = -0.15$ to $a = -0.2662$ in Fig.25 and 26. We also show the triple collision curves and the regions reg(c) in the background of these figures. Refer to Sect.5.1 in Part I for the correspondence between colour and reg(c). In addition, we plot mapped points for the points near the PPs to see the separatrix of unstable PPs and the libration around stable PPs.

In Fig.25, the process about the motion of PPs and the change of the Poincaré section is shown after the PPs with $\alpha = 3/5$ bifurcate until with $\alpha = 2/3$ do. For $\alpha = 3/5$, there are a pair of stable and unstable orbits. We call their orbital points s_1-s_5 and u_1-u_5 on the Poincaré section. The correspondence between the name and the location is shown in the Fig.25 (a). The separatrices of u_1-u_5 seem as if connected the PPs. The connecting lines draw a pentagon and a pentagram. The motion is the libration around the stable PPs, inside the small triangles surrounded by the edges of the pentagram and the pentagon: the size of these triangles shows the stability of the stable PPs. Even if the stable PPs are still far from the border of the Schubart region at (a)$a = -0.15$, the shape of the stable regions are reflected on the Schubart region elongating to left and right. As the PPs approach the border, the Schubart region becomes of pentagram shape. At (b) $a = -0.16$, there are the germ-shaped blocks, which are bifurcated from the arch-shaped ones. Each germ includes reg($5, 9, \cdots$), reg($9, 13, \cdots$), reg($7, 11, \cdots$), and so on, respectively. Since these germs grow along with the pentagram and surround the Schubart region, the Schubart region

takes pentagram shape. At (c)$a = -0.166$, the points selected to show the separatrices are scattered into the chaotic scattering region in several iteration of mapping. This behaviour of the points implies that the PPs have already been outside of the Schubart region. The germs intrude into between the pentagram and the stable regions of PPs: the germs separate the Schubart region and the stable regions of PPs. After that, the germs grow along the Schubart region with pentagonal shape, and come together around the stable PPs. The stable PPs sink toward the FPs, and head of germs follow the PPs. Therewith, the stable regions, and the gap between the germs, become small. Thereupon, a germ grows in the process of bifurcating from the right FP of an arch-shaped block, growing along this block, and sinking toward the left FP. Inside a germ, the ratio of the region with the lowest region number becomes large. Therefore, a germ finally change round to an arch-shaped region. Actually, let us confirm the above process by comparing the structure at (d)$a = 0.170$ and (e)$a = -0.186$ found in the second sector from the left, to give an example. In this sector, there are the arch-shaped block $reg(2, 6, \cdots)$ and the germ-shaped one $reg(7, 11, \cdots)$ piling up on it. The germ shaped block is germ-shaped, to the letter, and its second stratum is visible as $reg(11)$ at $a = -0.170$. In addition, there is a stable PP in the forward of head of the germ. While at $a = -0.186$, the germ seem to be arch-shaped and only $reg(7)$ is visible inside it. Moreover, the germ seems to compose of an arch-shaped block with $reg(2)$ and other regions. The stable PP is nearer the θ-axis at $a = -0.186$ than at $a = -0.170$. After $a = -0.186$, it is very difficult to find the location of the stable PPs for $\alpha = 3/5$. Hereafter, we show the unstable PPs only in the figure.

We follow the process until $\alpha = 2/3$ PPs bifurcate shown in Fig.25. The unstable PPs go slightly outward: u_3 approaches $R = R_{\max}$-line. Note that the point $(q_1, q_2, p_1, p_2) = (2\Lambda R_{\max}/(1 + \Lambda), 2R_{\max}/(1 + \Lambda), 0, 0)$ is mapped to the $R_{\max}$-line on (θ, R)-plane. The Schubart region is more expanded outward by the approximate edges $\overline{u_3 u_2}$ and $\overline{u_3 u_1}$ at Fig.25 (f)$a = -0.20$ than at Fig.25(e)$a = -0.186$. The reason seem to be the elongating effect at $R = R_{\max}$. At $a = -0.20$, $\alpha = 7/11$ PPs appear. When these PPs reach the border of the Schubart region, they expand the border outward further (Fig.25 (h)$a = -0.23$). However, the size of the eleven small triangles for $\alpha = 7/11$ shows the extent of stable regions is smaller than that for $\alpha = 3/5$ and $\alpha = 2/3$. From Fig.25 (i)$a = -0.24$, we can see that small germ-shaped regions come together around also the PPs with $\alpha = 7/11$. The unstable PPs stay the vertices of the Schubart region at least, after the PPs with $\alpha = 2/3$ bifurcate, until $a = -0.25$ (Fig.26 (a)$a = -0.25$). Figure 26 (b)$a = -0.2662$ is a stage where the PPs with $\alpha = 2/3$ go out of the Schubart region: as is the $\alpha = 3/5$ case, the unstable PPs are located at the vertices of the Schubart region and germ-shaped CSBs come together around the stable PPs.

The above observation enable us to construct the following scenario for the role of the PPs on the structure of the Poincaré section.
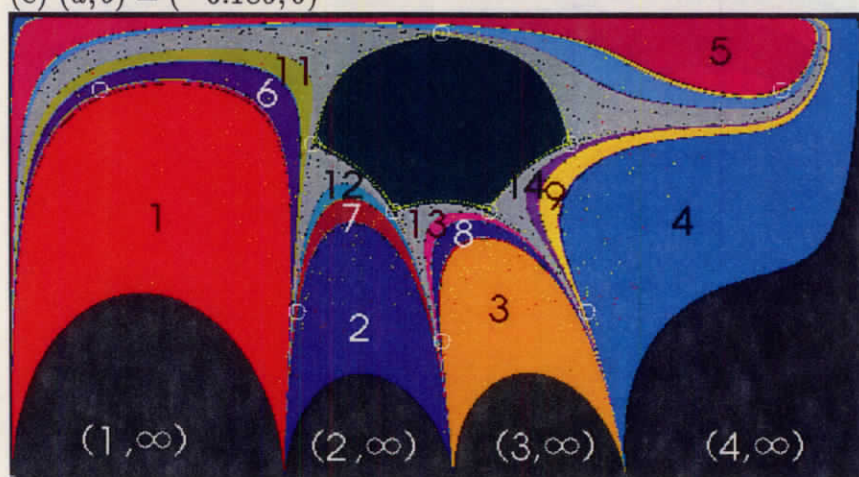
- The PPs with $\alpha = (n - 2)/n$ bifurcate from the FXP. The numbers of stable and

(a) $(a, b) = (-0.150, 0)$
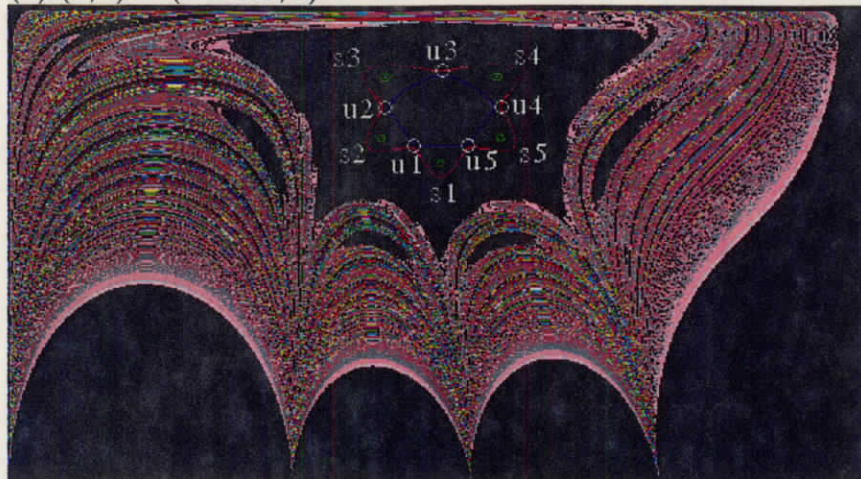
(b) $(a, b) = (-0.160, 0)$
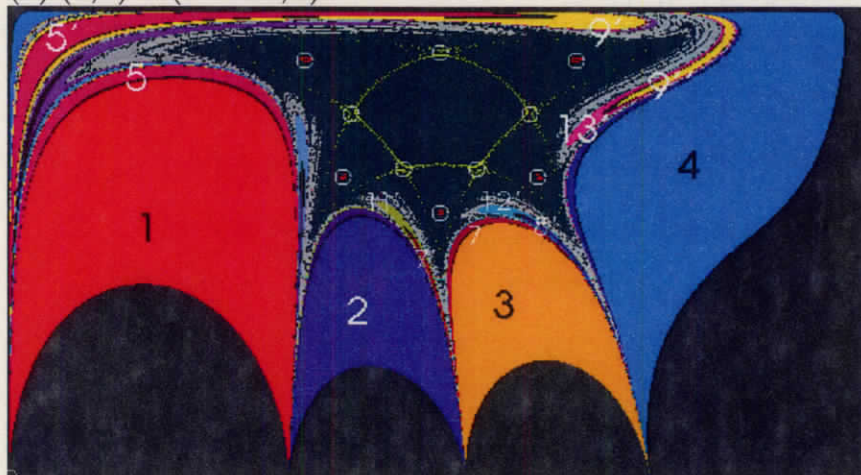
(c) $(a, b) = (-0.166, 0)$
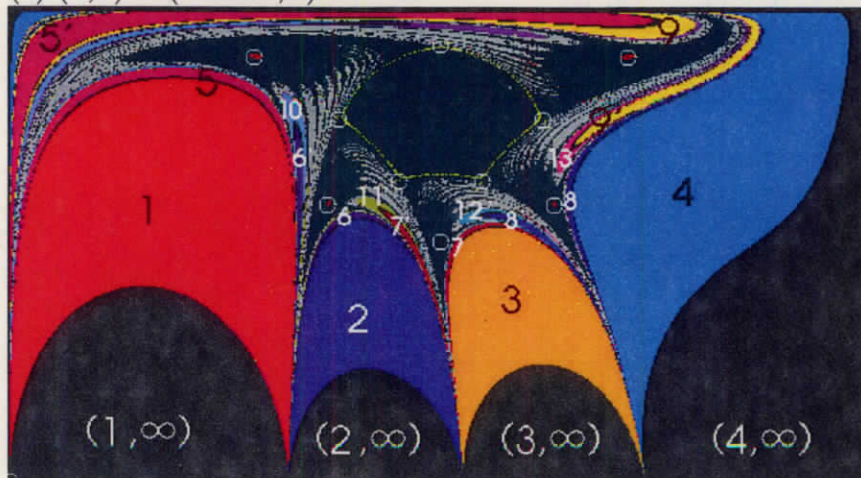
Figure 25: The PPs and the separatrix on the Poincaré section for $\alpha = 3/5$

78

(d) $(a, b) = (-0.170, 0)$
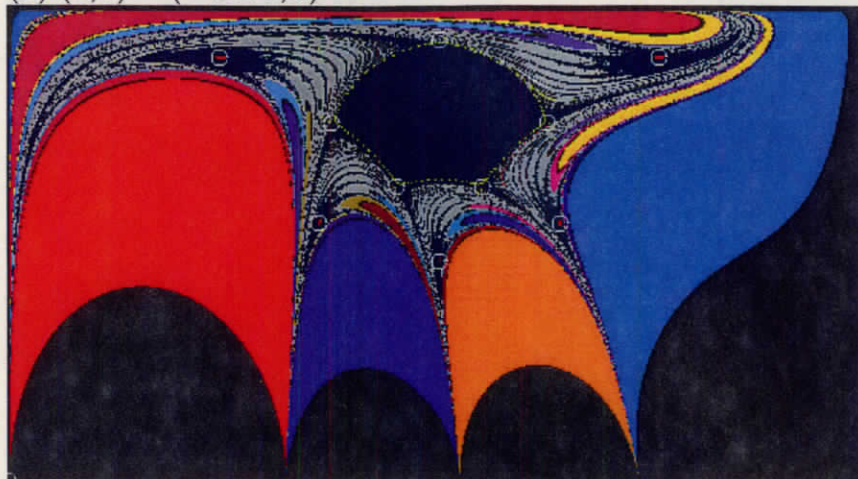
(e) $(a, b) = (-0.186, 0)$

(f) $(a, b) = (-0.200, 0)$
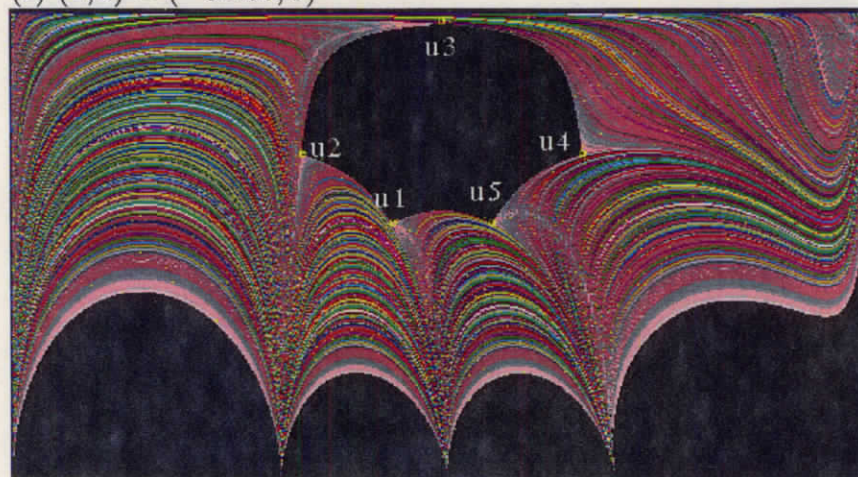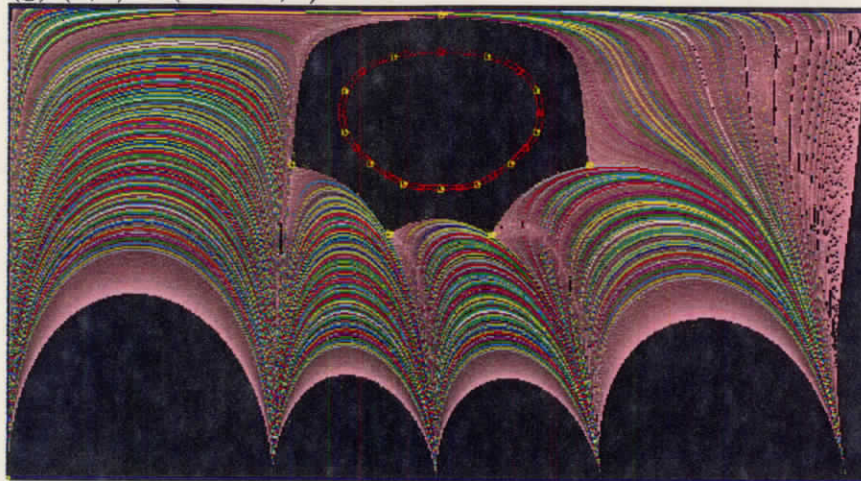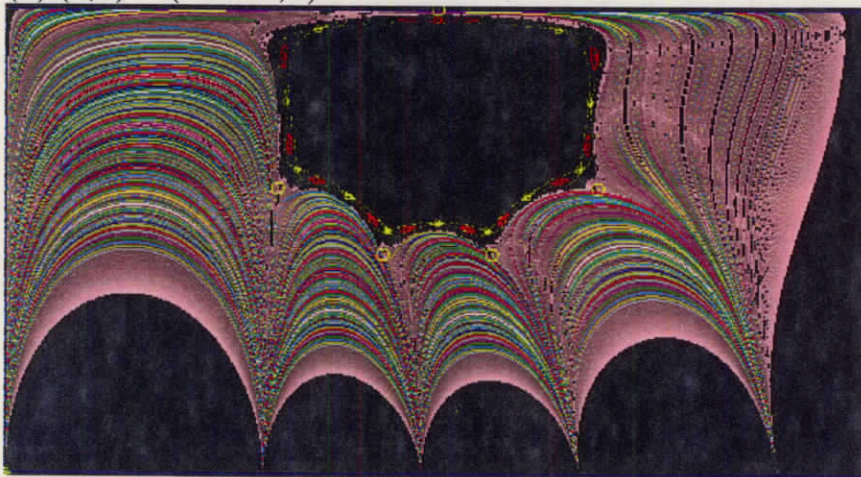

Figure 25: (continue)

(g) $(a, b) = (-0.210, 0)$

(h) $(a, b) = (-0.230, 0)$

(i) $(a, b) = (-0.240, 0)$
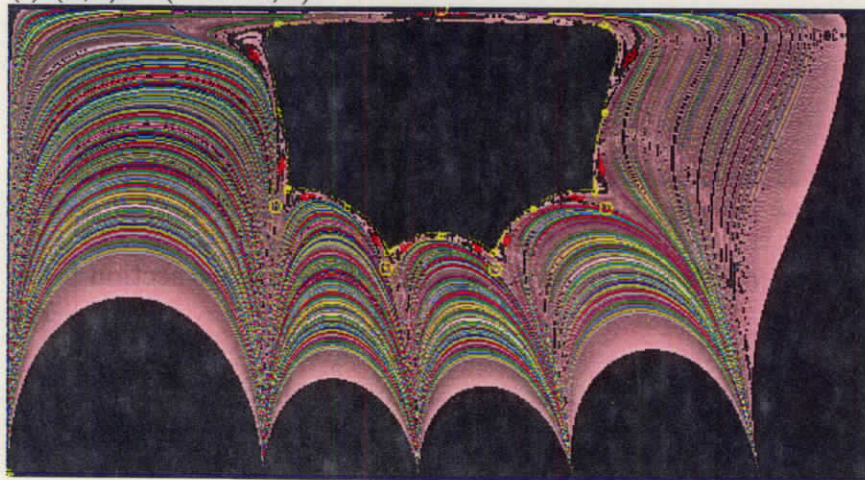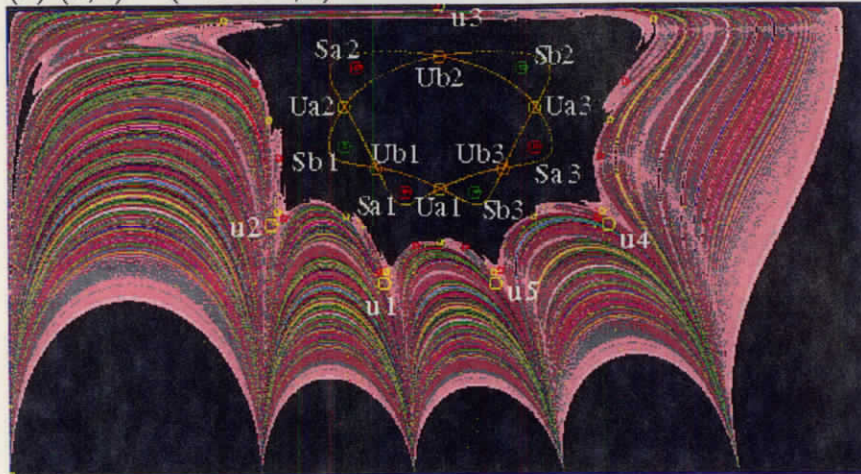

Figure 25: (continue)
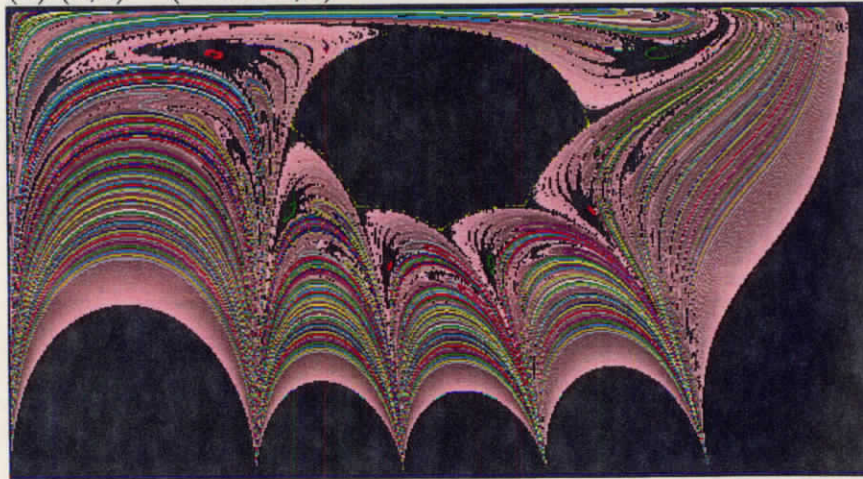
(a) $(a, b) = (-0.2500, 0)$

(b) $(a, b) = (-0.2622, 0)$

Figure 26: The PPs and the separatrix on the Poincaré section for $\alpha = 2/3$

unstable ones are n, respectively. Period is n for odd n and $n/2$ for even n. The distance from the FXP of stable PPs is farther than that of unstable PPs. At the moment of the bifurcation, n_{ACS} is $n-1$. The separatrices of the unstable PPs draw a polygram outside and a polygon inside.

- While the PPs are inside the Schubart region, the germ-shaped CSBs, which bifurcate from arch-shaped ones grow along the polygram. The Schubart region takes also polygram shape.

- After the PPs go out of the Schubart region, the polygram breaks, and the germ-shaped CSBs grow along the polygon. Therefore, the Schubart region becomes polygonal shape. The germ-shaped CSBs come together around the stable PPs.

- The unstable PPs stay at the vertices of the Schubart region though after the PPs with $\alpha = (n-1)/n$ bifurcate. The polygon drawn by the separatrices approximate the border of the Schubart region. While, the stable PPs sink toward the θ-axis with collecting the germ-shaped PPs and making their stable region shrink. As a result, the germ-shaped CBSs make the strata and recompose the arch-shaped CSBs. The germ-shaped CSB that grows along the roof of the Poincaré section becomes the n-th arch-shaped CSB.

4 Discussion

Here, we give a few interpretation for the result found in Sect.3.3. The Schubart region and arch-shaped blocks, which surround it, are of the structure associated to the FXP or the Schubart orbit. The outer region has lower similarity to the FXP than inner region about their orbits. Analogously, there must be the structure associated to the stable PPs around them. The stable regions around the PPs and the germ-shaped blocks coming together around them are of the just structure. The curves which separate the arch-shaped blocks are considered to be the separatrices, because we confirmed that there are the unstable PPs around the vertices and the stable ones on (the neighbouring of) the curves. While, the germ-shaped blocks also are separated by curves connected with the stable region of the PPs. From the analogy to the FXP and arch-shaped blocks, we expect that the 'child' PPs bifurcate from a PP and its separatrices appear as the curves.

5 Summary

We have studied the periodic points bifurcated from the fixed point (the Schubart orbit) and their influence on the structure of the Poincaré section for symmetric mass configuration. The following is the summary of the Part II.

- There is a value $a = a_{1/3}$ where the rotation number α at the fixed point is $1/3$. The periodic points bifurcate, with α grater than $1/3$ as a being decreased from $a_{1/3}$, and with α less than $1/3$ as increased. There are no periodic points bifurcated from the fixed points at $a = a_{1/3}$.

- The periodic orbits with $\alpha = (n - 2)/n$, n being integer, are influential in the structure of the Poincaré section. There is a rule about the number of orbits for these type orbits. A pair of stable and unstable orbits with period n bifurcate for odd n, while two pairs bifurcate for even n. We have confirmed this rule up to $n = 20$.

- The stable periodic points leave the fixed point quickly. They collect germ-shaped blocks with sinking toward the θ-axis. This collection results in recomposition of arch-shaped block from these germ-shaped blocks. While the unstable periodic points stay at the vertices of the Schubart region. Their separatrices approximate the border of the Schubart region.

Conclusion

The present research is the work that captures the continuous change of the Poincaré section caused by the mass variation by means of symbol dynamics. Before our research, the structural change of the Poincaré section is outlined by HM1993, while the structure of the chaotic scattering region is revealed only for the equal mass case by TM2000a and TM2000b using symbol sequences. We revealed this structure for general mass cases with applying the method of TM2000a and TM2000b. Particularly, the classification based on symbol sequences introduced in TM2000b was refined into regular expressions applicable to arbitrary symbol sequences. This classification enable us to follow the structural change of the Poincaré section caused by continuous variation of mass ratio. This change notified us to the intervention of the periodic orbits bifurcated from the Schubart orbit. We actually detected such periodic orbits to found the influence of them on the structural change of the Poincaré section.

We found the several rules through the present work, about which you can see in summaries in Part I and II. Here, we attempt to show the description of the structure and its change on the Poincaré section. There is a periodic orbit so-called the Schubart orbit for any mass ration in rectilinear three-body system. This orbit is unstable on the 'wedge' area including the $a = 0$-line and on the $a = 1/3$-line and stable the other area. If stable, this orbit is surrounded by stable orbits similar to this orbit and their outside surrounded by chaotic scattering orbits which are similar to the Schubart orbit during some collisions and however one of the particles is ejected through triple approach. These orbits are mapped to the Schubart region, the chaotic scattering region, and the fast escaping regions. The region number c can be considered as the similarity of orbits to the Schubart region. The divided Poincaré section into $\text{reg}(c)$ and $\text{reg}((c, \infty))$ shows this similarity decreases as going away from the Schubart orbit. A subregion of first escaping region makes a sector together with a arch-shaped block in the chaotic scattering region. The number of sectors is determined by the flow on the triple collision manifold (TCM). More concretely, the winding number of the stable manifolds on the TCM determines. Therefore, we can consider that the outline structure of the Poincaré section is governed by the limit orbits for zero initial distances.

The mass ration of our system is represented by a (central mass increase) and b (asymmetry of both sides). The structural change is mainly caused by the variation of a. If a is decreased, the periodic points bifurcate from the Schubart orbit. They appear as the stable and unstable periodic points on the Poincaré section. The periodic points with the rotation number with the form $(n - 2)/n$ are influential. A stable periodic point is surrounded by a stable region and its outside is surrounded by parts of the chaotic scattering region, as same as the Schubart region is. These parts of the chaotic scattering region are just germ-shaped blocks. The germ-shaped blocks recompose arch-shaped blocks or compose of the n-th arch-shaped block. While unstable periodic points stay at the vertices of the Schubart region. Their separatrices become the border of the Schubart

region or separate the neighbouring sectors. If a is continued to be decresed, the periodic points with the rotation numbers 3/5, 4/6, 5/7, $\cdots$, one after another bifurcate. These bifurcations result in the increase of the number of sectors to 5, 6, 7, $\cdots$. These numbers of sectors have to be consistent to the number of sectors determined from the flow on the triple collision manifold. It requires that the bifurcation of periodic points with the rotation number $(n-2)/n$ harmonise with the winding number of fictitious orbits. As far as our observation, this harmonisation occurs.

Acknowledgments

Bibliography

[1] R.McGehee, Triple collision in the collinear three body problem, Invetiones Mathematicae 27, 191-227(1974)

[2] J.L.Halbwachs, Binaries among the bright stars: estimation of the bias and study of the main-sequence starts, Astronomy and Astrophysics 128, 399-404(1983)

[3] Bo Reipurth and Hans Zinnecker, Visual binaries among pre-main sequence stars, Astronomy and Astrophysics 278, 81-108(1983)

[4] C. Simo, Mass for which triple ollision regularizable, Celestial Mechanics 21, 25-36(1980)

[5] S.Mikkola and J.Hietarinta, A numerical investigation of the one-dimentional Newtonian three-body problem I, Celecstial Mechanics and Dynamical Astronomy 46, 1-18(1989)

[6] S.Mikkola and J.Hietarinta, A numerical investigation of the one-dimentional Newtonian three-body problem II, Celecstial Mechanics and Dynamical Astronomy 47, 321-331(1990)

[7] S.Mikkola and J.Hietarinta, A numerical investigation of the one-dimentional Newtonian three-body problem III, Celecstial Mechanics and Dynamical Astronomy 51, 379-394(1991)

[8] M.Irigoyen et F.Nahon, Les mouvements rectilignes dans le probléme des trois corps lorsque la constante des forces vives est nulle, Astronomy & Astrophysics 17, 286-295(1972)

[9] J.Hietarinta and S.Mikkola, Chaos in the one-dimensional gravitational three-body problem, CHAOS 3, 183-203(1993)

[10] K.Tanikawa and S.Mikkola, Triple collisions in the one-dimentional three-body problem, Celecstial Mechanics and Dynamical Astronomy 76, 23-34(2000)

[11] K.Tanikawa and S.Mikkola, One-dimensional three-body problem via symbolic dynamics, CHAOS 10, 649-657(2000)

[12] M.Sekiguchi and K.Tanikawa, On the Symmetric Collinear Four-Body Problem, Publication of Astronomical Society of Japan 56, 235-251(2004)

[13] M.M.Sano, The classical Coulomb three-body problem in the collinear eZe configuration, Journal of Physics A: Mathematical and General 37-3, 803-822(2004)

[14] Agekyan, T. A. and Anosova, Zh. P., A Study of the Dynamics of Triple Systems by Means of Statistical Sampling, Soviet Astronomy 11, 1006(1968)

[15] Robert L.Devaney, Triple Collision in the planar isosceles three body problem, Inventions Mathematicae 60, 249-267(1980)

[16] Levi-Civita, T., Ann. Mat. Ser.3, 9, 1

[17] Wintner, A., The Analytical Fundation of Celestial Mechanics, Princeton University Press, Princeton, New Jersey, (1941)

[18] Kustaanheimo, P, Spinor regularization of the Kepler motion, Ann. Univ. Turku. Ser. AI., (1964)

[19] Kustaanheimo, P and Stoefel, E., Perturbation theory of Kepler motion based on spinor regularization, J. Reine Angew. Math., 218, 204-219(196)

[20] Stiefel, E.L. and Scheifele, G, Linear and Regular Celestial Mechanics, Springer-Verlag, Berlin Heidelberg New York, 6-35(1970)

[21] Chirikov, B. V., A universal instability of many-dimensional oscillator systems, Physics Report 52, 263-379

[22] K.Tanikawa and Y.Yamaguchi, Coexistence of symmetric periodic points in the standard map, Journal of Mathematical Physics 30, 608-616(1989)

[23] Lichtenberg, A. J. and Lieberman, M. A., Regular and Chaotic Dynamics Second Edition, Springer-Verlag, 164-244(1992)

[24] Murray, C. D. and Dermott, S.F, Solar System Dynamics, Cambridge University Press, 428-431(1999)